An atom trap trace analysis (ATTA) system for measuring ultra-low contamination by krypton in xenon dark matter detectors

Tae Hyun Yoon

Submitted in partial fulfillment of the
requirements for the degree
of Doctor of Philosophy
in the Graduate School of Arts and Sciences

COLUMBIA UNIVERSITY

2013

ABSTRACT

An atom trap trace analysis (ATTA) system for measuring ultra-low contamination by krypton in xenon dark matter detectors

Tae Hyun Yoon

The XENON dark matter experiment aims to detect hypothetical weakly interacting massive particles (WIMPs) scattering off nuclei within its liquid xenon (LXe) target. The trace ^{85}Kr in the xenon target undergoes β-decay with a 687 keV end point and 10.8 year half-life, which contributes background events and limits the sensitivity of the experiment. In order to achieve the desired sensitivity, the contamination by krypton is reduced to the part per trillion (ppt) level by cryogenic distillation. The conventional methods are not well suited for measuring the krypton contamination at such a low level. In this work, we have developed an atom trap trace analysis (ATTA) device to detect the ultra-low krypton concentration in the xenon target. This project was proposed to the National Science Foundation (NSF) as a Major Research Instrumentation (MRI) development [Aprile and Zelevinsky, 2009] and is funded by NSF and Columbia University.

The ATTA method, originally developed at Argonne National Laboratory, uses standard laser cooling and trapping techniques, and counts single trapped atoms. Since the isotopic abundance of ^{85}Kr in nature is 1.5×10^{-11}, the ^{85}Kr/Xe level is expected to be $\sim 10^{-23}$, which is beyond the capability of our method. Thus we detect the most abundant (57%) isotope ^{84}Kr, and infer the ^{85}Kr contamination from their known abundances. To avoid contamination by krypton, the setup is tested and optimized with ^{40}Ar which has a similar cooling wavelength to ^{84}Kr.

Two main challenges in this experiment are to obtain a trapping efficiency high enough to detect krypton impurities at the ppt level, and to achieve the resolution to discriminate single atoms. The device is specially designed and adjusted to meet these challenges. After

achieving these criteria with argon gas, we precisely characterize the efficiency of the system using Kr-Xe mixtures with known ratios, and find that ∼90 minutes are required to trap one ^{84}Kr atom at the 1-ppt Kr/Xe contamination.

This thesis describes the design, construction, and experimental results of the ATTA project at Columbia University.

Table of Contents

1 The XENON experiment **1**

1.1 Evidence of dark matter 1

1.1.1 Rotation curves of galaxies 1

1.1.2 Galaxy clusters 2

1.1.3 Cosmic microwave background 5

1.2 Dark matter searches 6

1.2.1 Weakly interacting massive particles (WIMPs) 6

1.2.2 Detection strategies 8

1.3 XENON dark matter experiment 9

1.3.1 Liquid xenon as a WIMP detection medium 9

1.3.2 Principle of the XENON dark matter experiment 11

1.3.3 The XENON100 detector 13

1.4 Background in XENON100 15

1.4.1 Background sources 15

1.4.2 Removal of ^{85}Kr from xenon 18

2 Atomic properties **22**

2.1 Argon 22

2.1.1 ^{40}Ar 23

2.2 Krypton 25

2.2.1 ^{85}Kr 27

2.2.2 ^{84}Kr 30

2.3 Xenon 30

3 Basic concepts **32**

3.1 Light forces on atoms 32

3.2 Optical molasses 35

3.2.1 Principle of optical molasses 35

3.2.2 The Doppler limit of optical molasses 37

3.3 Zeeman slowing 39

3.4 Magneto-optical trap 41

4 Experimental apparatus **44**

4.1 Laser system 45

4.2 Vacuum system 49

4.3 RF discharge source 50

4.3.1 Possible excitation methods 50

4.3.2 RF discharge resonator 52

4.4 Transverse cooling of the atomic beam 54

4.5 Zeeman atom slower 57

4.5.1 Design 57

4.5.2 Construction 64

4.5.3 Field measurements 65

4.6 Magneto-optical trap 68

4.7 Laser shutter 73

5 Cooling and trapping **76**

5.1 Source cooling 76

5.2 CCD camera calibration 79

5.3 Consumption rate of argon 81

5.4 Atomic flux 82

5.5 Magneto-optical trap of argon 85

6 Single atom detection **89**

6.1 Avalanche photodiode 89

6.2 Optics 90

6.3 Background noise 94

6.3.1 Light intensity locking PID controller 97

6.3.2 Background fluctuation 98

6.4 Single atom signal 101

7 Krypton abundance measurement **106**

7.1 Measurement of krypton in argon gas 107

7.2 Consumption rate of xenon gas 108

7.3 Source efficiency versus pressure 109

7.4 Xenon gas with high krypton contamination 110

7.4.1 Xenon bottle 1 110

7.4.2 Xenon bottle 2 112

7.5 Calibration for krypton in xenon studies 113

7.5.1 Pure xenon gas from PraxAir 115

7.5.2 12 ppm krypton mixture 115

7.5.3 0.75 ppm krypton mixture 116

7.5.4 System efficiency for krypton in xenon 117

7.6 Xenon extraction from the XENON detector 117

8 Conclusion **119**

Bibliography **120**

List of Figures

1.1 Measured rotation curve of the NGC 6503 galaxy. 2
1.2 Galaxy cluster Abell 370. 3
1.3 Composite images of the matter in galaxy cluster 1E 0657-56 (bullet cluster) and MACS J0025.4-1222. 4
1.4 The cosmic microwave background (CMB) from 15.5 months of Planck data. 5
1.5 The angular power spectrum of temperature fluctuations measured by Planck. 6
1.6 The co-moving number density Y and the resulting thermal relic density of a 100 GeV dark matter particle as a function of temperature T and time t. 7
1.7 Scintillation mechanism in LXe and different processes that can lead to the quenching of scintillation light. 11
1.8 Operation principle of the dual-phase XENON100 detector. 12
1.9 Schematic of the XENON100 dark matter detector. 14
1.10 Results on the spin-independent WIMP-nucleon scattering cross section from XENON100. 15
1.11 Schematic of the XENON100 purification system and image of the gas panel. 16
1.12 Cryogenic distillation column used to separate krypton. 17
1.13 Differential scattering rates of weakly interacting massive particles (WIMPs) and decay rates of ^{85}Kr. 19
1.14 Cryogenic distillation column used to separate krypton. 20

2.1 Grotrian diagram of argon. 24
2.2 Grotrian diagram of krypton. 28
2.3 Global accumulated ^{85}Kr inventory and the annual emissions. 29

3.1 Magnitude of the scattering force exerted on an atom via atom-photon interaction. . . . 35
3.2 Schematic of atom-photon interaction for an atom moving toward the light source. . . . 36
3.3 Optical molasses force as a function of atom velocity along the axis of light propagation. . . . 37
3.4 Diagram of the energy level according to atom velocity and magnetic field in a Zeeman slower. . . . 40
3.5 Schematic of three dimensional magneto-optical trap (MOT) 42

4.1 Schematic of the atom trap trace analysis (ATTA) system. . . . 44
4.2 Photo of the atom trap trace analysis (ATTA) system at Columbia University. 45
4.3 Schematic of a Littman-Metcalf external cavity diode laser (ECDL) 46
4.4 Schematic of the laser system. . . . 47
4.5 Schematic of the vacuum system. . . . 50
4.6 Excitation schemes for ^{84}Kr atom. . . . 51
4.7 Cross section of the RF discharge source. . . . 52
4.8 Image of the helical coil RF resonator. . . . 53
4.9 Glowing plasma discharge of argon and xenon gas by a helical coil resonator. 54
4.10 Schematic of the first transverse cooling setup. . . . 55
4.11 First-stage transverse cooling efficiency as a function of the laser intensity. . 56
4.12 Relevant energy levels when external field B is applied, and relative transition strengths for $^3P_2$ and $^3D_3$ states. . . . 58
4.13 Design field for the Zeeman slower with a 310 MHz red detuned laser. . . . 59
4.14 Velocity trajectories in the Zeeman slower. . . . 61
4.15 Transverse divergence for the highest captured velocity groups of krypton and argon. . . . 63
4.16 A square copper tube was welded for water cooling. . . . 64
4.17 Measurement of the Zeeman slower field in the longitudinal direction. . . . 66
4.18 Velocity trajectory of Kr evaluated based on the measured Zeeman slower field. 67
4.19 Atom trajectories in the one dimensional magneto-optical trap (MOT). . . 68

4.20 Winding the magneto-optical trap (MOT) coil and MOT field measurement. 69
4.21 Magneto-optical trap (MOT) field and its derivative in the z-direction. . . . 70
4.22 Magneto-optical trap (MOT) field and its derivative in the x-direction. . . . 71
4.23 Chamber and coils for the magneto-optical trap (MOT). 72
4.24 Custom-made laser shutter to mechanically switch laser beam. 74
4.25 Photodiode signal for opening and closing of the shutter. 75

5.1 Maxwell-Boltzmann distributions for argon and krypton beams. 77
5.2 Capture fractions of the Zeeman slower as a function of temperature 78
5.3 Schematic of fluorescence detection with the camera. 80
5.4 Pressure in the reservoir decreases linearly with time as the gas is consumed. 81
5.5 Consumption rates of argon gas for different pressures in the source chamber. 82
5.6 Schematic of the fluorescence measurement in the 1st transverse cooling (TC) chamber. 83
5.7 Histogram of atomic densities as a function of position. 85
5.8 Loading and decay plots for the argon MOT. 87

6.1 Prototype schematic of the APD failsafe circuit. 90
6.2 Schematic of the single atom detection system. 91
6.3 Beam trace and transverse aberration from the OSLO simulation. 92
6.4 Photo of the single atom detection system. 93
6.5 MOT image taken at the position of the APD. 94
6.6 Single atom signals captured by the APD with a high background fluctuation. 95
6.7 Laser intensity measurements at several locations. 96
6.8 Schematic of the intensity locking proportional-integral-derivative (PID) circuit. 97
6.9 Relative laser intensity with and without the PID intensity locking box. . . 99
6.10 Standard deviation of background noise. 100
6.11 Single atom signals measured by the APD with several integration times. . 102
6.12 Single argon atom signals measured by the APD. 103
6.13 Histogram of lifetimes of 74 trapped argon atoms. 104

7.1 Helical coil resonators for the argon vapor cell and the krypton vapor cell. . 106
7.2 Consumption rates of xenon gas for different pressures in the source chamber. 109
7.3 Relative source efficiency for krypton in xenon gas in the function of the source pressure. 110
7.4 Schematic of the gas inlet system and image of a krypton chamber and its connections. 114
7.5 A pipette to extract and carry xenon gas from the XENON100 detector. . . 118

List of Tables

1.1 A series of XENON dark matter experiments. 13
1.2 Summary of the predicted electronic recoil background 18

2.1 Physical properties of argon. 23
2.2 Energy levels of neutral argon. 25
2.3 Physical properties of krypton. 26
2.4 Energy levels of neutral krypton. 27
2.5 Physical properties of xenon. 31

4.1 Beam properties for each stage of the experiment. 48
4.2 Zeeman slower specifications. 67
4.3 Magneto-optical trap (MOT) specifications. 73

5.1 Velocity distributions for gases of particles (1D and 3D) and for a thermal beam. 79
5.2 Consumption rates of argon gas for different pressures in the source chamber. 82
5.3 Characteristics of fluorescent atoms at five different laser frequencies. 84
5.4 Contribution of each stage to the loading rate. 86
5.5 Characteristics of the ATTA system with argon. 88

6.1 Transmission measurements of the bandpass filter as a function of the incidence angle. 92
6.2 Contribution of each component to the background noise in APD measurements with argon gas. 95

6.3 Comparison of the laser modes for trapping and detecting. 101

7.1 Consumption rates of krypton gas for different pressures in the source chamber. 108
7.2 Relative source efficiency for krypton in xenon gas as a function of the source pressure at a -20 dBm RF power. 109
7.3 Mass components in the first bottle of xenon gas analyzed by the RGA. . . 111
7.4 Mass components in the second bottle of xenon gas analyzed by the RGA. . 113
7.5 Specified impurity levels of the xenon bottle from PraxAir. 113

Acknowledgments

I would like to express the deepest appreciation to my advisor, Prof. Tanya Zelevinsky, who gave me support, guidance, and inspiration with kindness and patience throughout the life of this work. I am also grateful to Prof. Elena Aprile for planning this project and providing insightful advice. It was a great pleasure to study and work with thoughtful and enthusiastic professors.

Through this project, I enjoyed working with great colleagues, Claire Allred, Andre Loose, and Luke Goetzke. Their passion and efforts motivated me to pursue the goal. In addition, many thanks Prof. Philip Kim for concern and help along the way, to Kyungeun Lim for help in writing thesis. I also thank the thesis committee members, Prof. Chee Wei Wong and Prof. Rachel Rosen, for their interest and feedback on my thesis.

Finally, this journey would not have been possible without the dedicated support and love of my family. Special thanks to my wife Jihae Shin, my daughter Yireh Yoon, and my parents. Above all, I thank God who made it all happen.

Chapter 1

The XENON experiment

Various astronomical observations over the last few decades suggest the presence of invisible components, which accounts for a large portion of the total energy density in our universe. One of them, dark energy, has a gravitationally repulsive property and helps explain the acceleration of the expansion of the universe. Another component, dark matter, is gravitationally attractive and observable only through gravitational and weak forces. According to the recent data from the Planck mission, the universe consists of 68.3% dark energy, 26.8% dark matter, and 4.9% ordinary matter [Ade *et al.*, 2013].

Finding dark matter is one of the most important open problems in both astrophysics and particle physics. Currently, many groups around the world are attempting to detect dark matter with direct and indirect methods. In this chapter, we review the evidence and detection strategies for dark matter, then the focus shifts to the XENON dark matter search and its background noise sources.

1.1 Evidence of dark matter

1.1.1 Rotation curves of galaxies

Galactic rotation curves are the most convincing and direct evidence for dark matter [Bertone *et al.*, 2005]. The velocity of particles as a function of their trajectory radius can be obtained by observing the redshift of the 21 cm hyperfine transition line of hydrogen [Begeman *et al.*, 1991].

In Newtonian dynamics, this circular velocity is expressed as

$$v(r) = \sqrt{\frac{GM(r)}{r}} \tag{1.1}$$

where $M(r) = 4\pi \int \rho(r) r^2 \mathrm{d}r$ is the mass inside radius r, and $\rho(r)$ is the mass density profile. From this equation, one can predict that velocities fall as $v(r) \propto r^{-1/2}$ beyond the visible stellar disk. Measured rotation curves, however, exhibit a flat behavior at large distances, implying the existence of a dark halo with the mass density $\rho(r) \propto 1/r^2$ beyond the stellar disk. A typical example of galactic rotation curves is shown in Fig. 1.1, from the spiral galaxy NGC 6053.

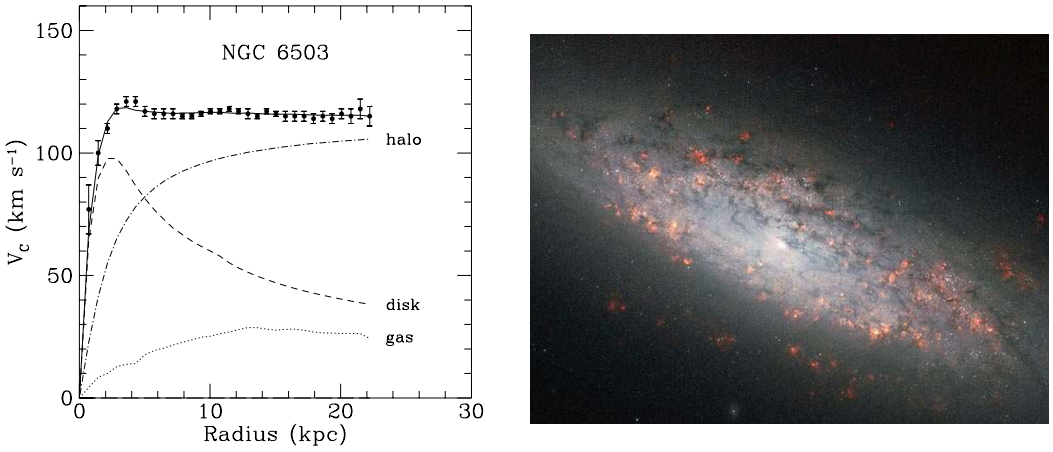

Figure 1.1: Measured rotation curve of the NGC 6503 galaxy as a function of radius r (left). The contributions of gas, disk and dark matter are expressed by the dotted, dashed, and dash-dotted lines, respectively. Figure (left) from [Begeman *et al.*, 1991]. Picture of NGC 6503 spiral galaxy (right). Pink-colored regions mark where stars have recently formed in NGC 6503's swirling spiral arms. Image credit (right): ESA/Hubble and NASA.

1.1.2 Galaxy clusters

A galaxy cluster is a structure consisting of hundreds of galaxies bound by gravity. The evidence for dark matter can be found in several aspects at the scale of galaxy clusters.

In 1933, Zwicky measured the velocity dispersion of galaxies in the Coma cluster, and derived the mass of the cluster using the virial theorem. The calculated mass was 400 times larger than the value expected from their luminosity and the solar mass-to-luminosity ratio. Zwicky inferred the presence of invisible matter, and referred it as Dunkle Materie, 'dark matter' [Zwicky, 1933].

In the 1960s, rocket flights detected X-ray emission from the direction of the Virgo cluster, the closest cluster to our galaxy [Friedman *et al.*, 1967]. High temperature plasma heated by the gravitational potential well in galaxy clusters becomes a source of bremsstrahlung X-ray emission. One can estimate the mass of the cluster from this emission, using the fact that the amount of emitted X-rays is proportional to the plasma density squared. The mass estimate of the galaxy cluster Abell 2029 from the Chandra X-ray observation indicates that unseen matter dominates the mass of the cluster [Lewis *et al.*, 2003].

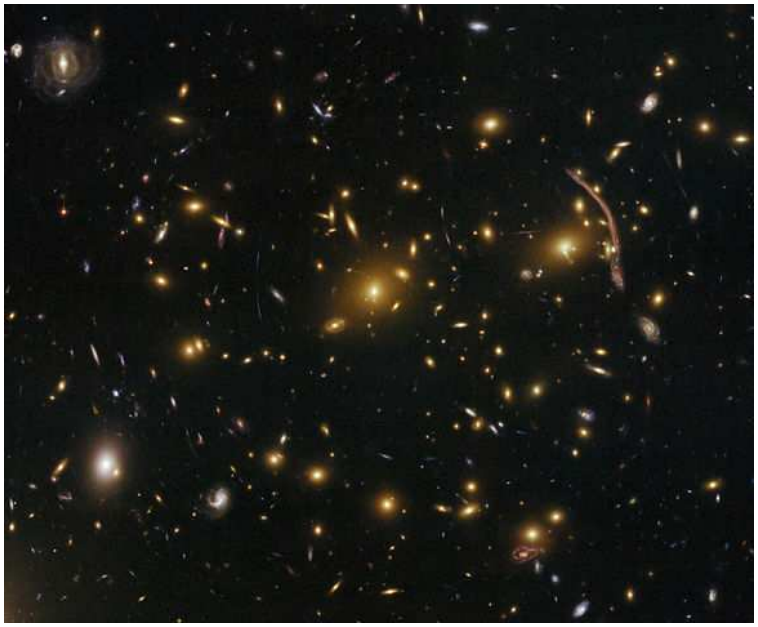

Figure 1.2: Image of galaxy cluster Abell 370 taken by the Hubble Space Telescope Advanced Camera. Image credit: NASA, ESA, the Hubble SM4 ERO Team and ST-ECF.

Gravitational lensing is another tool at the scale of clusters. According to general relativity, any matter with non-zero mass warps spacetime, and light which goes straight along this spacetime is deflected. This process is analogous to light deflection by optical

lenses. In case that the observer, the lens, and the object are aligned in a straight line, the light source appears as a ring around the object. If there is any misalignment, the image will appear as segments of arcs. The strength of gravitational lensing is determined by the mass of the lens, and the distances between the observer, the lens, and the object. Figure. 1.2 shows a picture of the galaxy cluster Abell 370, one of the first galaxy clusters where gravitational lensing was observed. Several arcs in this image indicate the phenomenon of gravitational lensing.

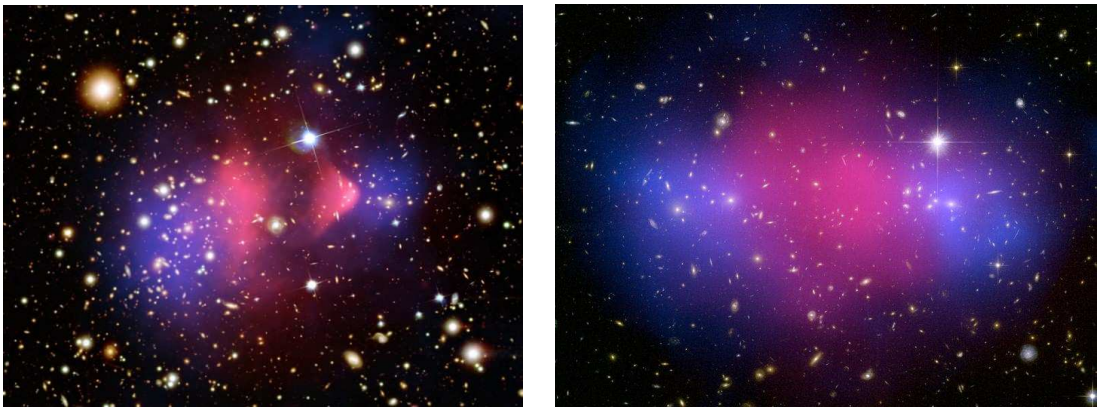

Figure 1.3: The matter in galaxy cluster 1E 0657-56 well-known as the "bullet cluster"(left) and MACS J0025.4-1222 (right), shown as composite images. Image credit (left): X-ray (NASA/CXC/CfA/ M.Markevitch *et al.*; Lensing Map (NASA/STScI; ESO WFI; Magellan/U.Arizona/ D.Clowe *et al.*); Optical (NASA/STScI; Magellan/U.Arizona/D.Clowe *et al.*); Image credit (right): X-ray (NASA/CXC/Stanford/S. Allen); Optical/Lensing (NASA/STScI/UC Santa Barbara/M. Bradac).

"Bullet Cluster (1E 0657-558)" directly demonstrates the presence of dark matter [Clowe *et al.*, 2004; Clowe *et al.*, 2006]. It consists of two colliding galaxy clusters. As two clusters come into collision, the ordinary matter in the clusters interacts and slows down. On the other hand, the dark matter does not participate in any interaction and passes through without interruption. This results in separation of ordinary matter and dark matter after the collision. Figure 1.3 shows the visible mass distribution (pink) obtained by its X-ray signature, and the mass distribution (blue) inferred from gravitational lensing. The later

discovered galaxy cluster MACS J0025.4-1222 also confirms this explanation [Bradač *et al.*, 2008].

1.1.3 Cosmic microwave background

In 1963, Arno Penzias and Robert Wilson unexpectedly discovered the cosmic microwave background (CMB) while studying signals from the Milky Way galaxy [Penzias and Wilson, 1965]. The CMB is almost uniform in all directions (2.72548 K), but has tiny spacial irregularities (0.00057 K) [Fixsen, 2009]. Assuming that the thermal variation by quantum fluctuation in a small region of space has expanded to the size of the current universe as the Big Bang model predicts, the expectations are well consistent with the observed irregularities of the CMB. Figure 1.4 shows the CMB image acquired by the Planck space telescope. The primordial fluctuations in this image are the seeds of all current structures: the stars and galaxies. In Fig. 1.5, the temperature fluctuation from Planck is analyzed

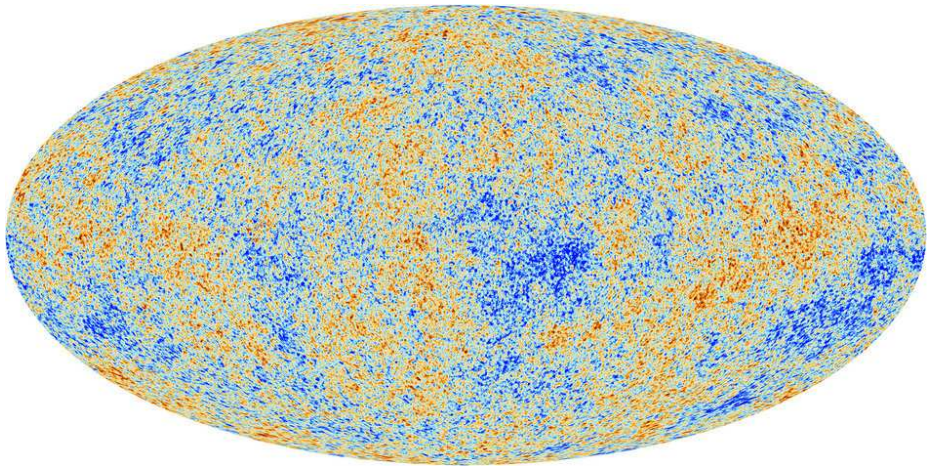

Figure 1.4: The cosmic microwave background (CMB) from 15.5 months of Planck data, imprinted on the sky when the universe was 380,000 years old. Tiny fluctuations give rise to formation of large-scale structure. Credit: ESA and the Planck Collaboration.

at different angular scales. The data extremely well agree with what ΛCDM model, which contains the cosmological constant and cold dark matter, predicts. Several peaks in the power spectrum are called acoustic peaks. The amplitude and position of the peaks depend

on a number of cosmological parameters like the physical baryon density $\Omega_{\rm b}h^2$, the physical cold dark matter density $\Omega_{\rm CDM}h^2$, and the dark energy density Ω_Λ. The derived parameter values from Planck are $\Omega_{\rm b}h^2 = 0.022068 \pm 0.00033$, $\Omega_{\rm CDM}h^2 = 0.1196 \pm 0.0031$, and $\Omega_\Lambda = 0.686 \pm 0.020$ [Ade *et al.*, 2013].

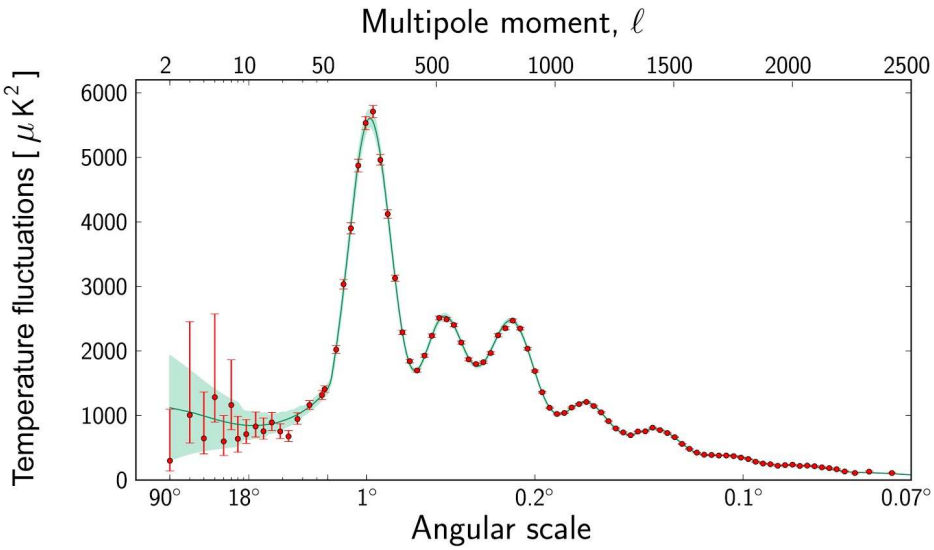

Figure 1.5: The angular power spectrum of temperature fluctuations measured by Planck. The red dots are Planck's observations, and the green curve shows the standard model of the Big Bang cosmology. Credit: ESA and the Planck Collaboration.

1.2 Dark matter searches

1.2.1 Weakly interacting massive particles (WIMPs)

The Standard Model of particle physics has been successful in explaining a wide range of phenomena experimentally investigated. On the other hand, it faces some challenges: It requires the bare mass of the Higgs boson to be fine-tuned to cancel very large quantum corrections, which is an unnatural ad hoc procedure. While the Standard Model describes the electromagnetic, weak, and strong nuclear interactions, gravity is not properly included.

Furthermore, it does not provide any proper candidates for dark matter or dark energy. The supersymmetry model (SUSY) is an elegant extension of the Standard Model, proposing that every particle has a superpartner, with identical properties but whose spin differs by a half-integer from that of the original particle. The problems with the Standard Model mentioned above can be solved by SUSY. Particularly, it postulates the existence of weakly interacting massive particles (WIMPs) as candidates for non-baryonic dark matter.

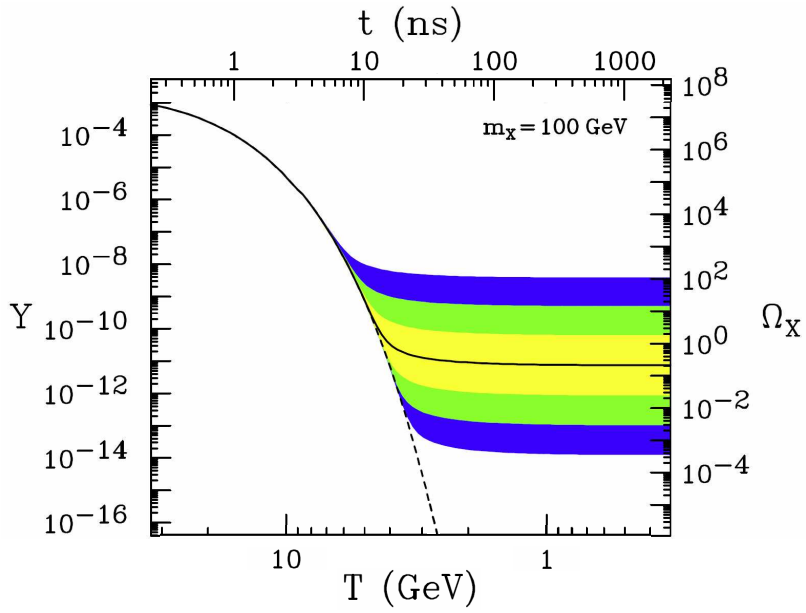

Figure 1.6: The co-moving number density Y and resulting thermal relic density Ω_X of a 100 GeV dark matter particle as a function of temperature T (bottom) and time t (top). The solid contour is for an annihilation cross section that yields the correct relic density, and the shaded regions are for cross sections that differ by 10, 10^2, and 10^3 from this value. The dashed contour is the number density of particle that remains in thermal equilibrium. Figure from [Feng, 2010].

WIMPs are predicted to have mass in the range from 10 GeV to few TeV, and they interact with ordinary matter via the weak nuclear force and gravity. They do not interact through electromagnetic or strong nuclear forces. Thus WIMPs are dark and invisible. The most promising WIMP candidate is the neutralino, the lightest stable supersymmetric particle [Jungman *et al.*, 1996].

The WIMP hypothesis is based on the assertion that dark matter is a thermal relic of the Big Bang. The high energy in the early universe made energy and mass switch from one form to the other freely according to Einstein's mass-energy equivalence, $E = mc^2$. As the universe expands, it cools and loses the energy required to create particle pairs. Thus, the number of dark matter particles drops exponentially as $e^{-m_\chi/T}$ where T is the temperature of the universe and m_χ is the dark matter particle's mass. In addition, as the universe grows, the gas of dark matter particles becomes so dilute that they don't interact with and annihilate each other. Then the dark matter particles freeze out to their thermal relic density [Feng, 2010], which is estimated by

$$\Omega_\chi h^2 \simeq \frac{3 \times 10^{-27}\ \mathrm{cm}^3\ \mathrm{s}^{-1}}{\langle \sigma_A v \rangle}, \tag{1.2}$$

where $\langle \sigma v \rangle$ is the thermal average of the total annihilation cross section of the particle multiplied by its velocity. Figure 1.6 shows the thermal relic density. When a dark matter particle is assumed to have weak interactions, the annihilation cross section is computed to be $\langle \sigma v \rangle \sim \alpha^2 (100\mathrm{GeV})^{-2} \sim 10^{-25} \mathrm{cm}^3\ \mathrm{s}^{-1}$, for $\alpha \sim 10^{-2}$. This is remarkably close to the value thought for dark matter in the universe [Jungman *et al.*, 1996], and it is referred to as the 'WIMP miracle'.

1.2.2 Detection strategies

Searches for WIMPs are divided into three classes: indirect detection, direct detection, and detection in particle colliders. Indirect detection methods search for the products of WIMP annihilation or decay where they are concentrated, such as centers of galactic halos or the center of the Sun. Currently, several experiments aim to find various annihilation products: cosmic rays, gamma rays and neutrinos [Carr *et al.*, 2006; Bertone, 2010]. The Fermi gamma-ray space telescope searches for gamma rays from dark matter annihilation, while the PAMELA experiment and the Alpha magnetic spectrometer on the International Space Station observe positrons. Experiments including AMANDA, IceCube [Abbasi *et al.*, 2011], and ANTARES [Ageron *et al.*, 2011] aim to detect signals in the form of high-energy neutrinos.

Direct detection experiments look for signals from the scattering events of WIMPs off atomic nuclei inside a detector. They usually operate in deep underground laboratories

to protect them from cosmic radiation and to reduce background. The sensitivity of direct detection has improved by more than three orders of magnitude over the past two decades [Gaitskell, 2004; Bertone, 2010]. There are several technologies for direct detection of WIMPs. Cryogenic detectors, operating at temperatures below 100 mK to limit thermal noise, detect the phonon signals produced from elastic collisions between dark matter particles and crystal atoms such as germanium. The experiments CDMS [Ahmed *et al.*, 2010], CRESST [Angloher *et al.*, 2012], and EDELWEISS [Armengaud *et al.*, 2012] make use of cryogenic detection. Liquid noble gas detectors detect scintillation light produced when WIMPs interact with nuclei of the target material, liquid xenon (LXe) or liquid argon (LAr). These experiments include XENON, LUX [McKinsey *et al.*, 2010], ArDM [Marchionni *et al.*, 2011], and DarkSide [Alton *et al.*, 2009].

Another way to find dark matter is to create it in a laboratory. The Large Hadron Collider (LHC) will reach a center of mass energy of 14 TeV after an upgrading procedure to be completed in 2015. Then the existence of new particles at this energy level can be tested. Because a WIMP will pass through the detector due to its negligible interactions with matter, the existence of WIMPs could be inferred from missing energy and momentum, provided all the other collision products are accounted for [Kane and Watson, 2008]. These experiments could detect WIMPs created in high-energy collision, but positive results of direct detection experiments are still required to convince us that enough of them exist in the galaxy to account for all the dark matter signatures.

1.3 XENON dark matter experiment

1.3.1 Liquid xenon as a WIMP detection medium

The XENON dark matter search experiment uses liquid xenon targets to detect nuclear recoils that WIMPs produce in rare interactions with them. One of the most important characteristics of a medium in detection of radiation is its capacity to transform the energy absorbed into measurable signals, while stopping incident radiation. Interactions in general depend on the type of incident particle [Aprile and Doke, 2010]. Among liquid rare gases suitable for radiation detection, LXe has the highest atomic number (54) and density ($\sim$3

g/cm^3) at a modest boiling temperature. These help LXe stop penetrating radiation very efficiently. LXe produces both charge carriers and scintillation photons in response to radiation. This is a unique feature of LXe, shared only with liquid argon (LAr) among liquid rare gases [Aprile and Doke, 2010].

During the interactions with radiation, both direct excitation of atoms and electron-ion recombination lead to the formation of excited dimers, Xe_2*. Scintillation light is produced when these excited dimers decay to the ground state. Thus the scintillation photons in LXe originate in two separate processes involving excited atoms (Xe*) and ions (Xe^+), both produced by ionizing radiation:

$$Xe^* + Xe \rightarrow Xe_2^*, \tag{1.3}$$

$$\begin{aligned} Xe^+ + Xe &\rightarrow Xe_2^+, \\ Xe_2^+ + e^- &\rightarrow Xe^{**} + Xe, \\ Xe^{**} &\rightarrow Xe^* + \text{heat}, \end{aligned} \tag{1.4}$$

$$\begin{aligned} Xe^* + Xe &\rightarrow Xe_2^*, \\ Xe_2^* &\rightarrow 2Xe + hv. \end{aligned} \tag{1.5}$$

Equation 1.3 shows the production of Xe_2^* from an excited atom, and Eq. 1.4 shows the production processes from an ionized atom. The emitted vacuum ultraviolet (VUV) scintillation photons (Eq. 1.5) have wavelengths centered at 178 nm with a width of 14 nm [Jortner *et al.*, 1965].

At high ionization densities, a quenching mechanism called "bi-excitonic collisions" could play a role [Hitachi, 2005]:

$$Xe^* + Xe^* \rightarrow Xe_2^{**} \rightarrow Xe + Xe^+ + e^-. \tag{1.6}$$

An electron-ion pair and a neutral atom are produced in a collision of two excited atoms. The electron generated in Eq. 1.6 recombines with an ion and leads to a production of an exited atom. This process results in two excited atoms producing only one photon. Figure 1.7 describes the scintillation processes and the possible quenching mechanism.

In addition to scintillation, the energy deposited by radiation leads to the production of electron-ion pairs, excited atoms, and free electrons. The number of electron-ion pairs

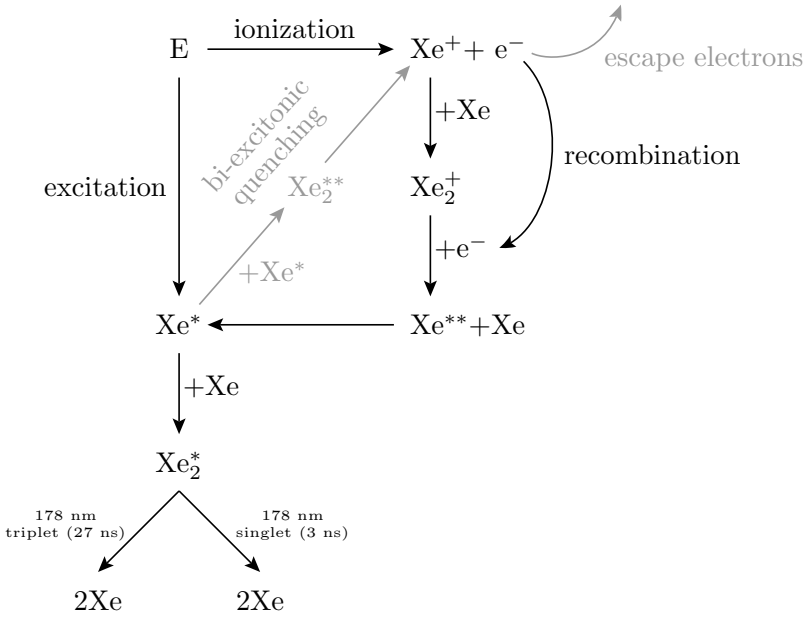

Figure 1.7: Scintillation mechanism in LXe (black) and different processes that can lead to the quenching of scintillation light (gray). Figure from [Plante, 2012].

produced per unit absorbed energy is called the ionization yield. LXe has the largest ionization yield of all liquid noble gases. The produced electron-ion pairs tend to recombine to form neutral atoms again. For the correct measurement of the ionization yield, an external electric field is required to collect electrons and ions separately [Aprile and Doke, 2010].

1.3.2 Principle of the XENON dark matter experiment

The XENON dark matter experiment employs a dual-phase (liquid-gas) time projection chamber (TPC) to simultaneously measure the scintillation light at a few keV_{ee} (keV electron equivalent) [Aprile *et al.*, 2006] and ionization at the single electron level. The schematic of the XENON dark matter detector and the detection principle are shown in Fig. 1.8. The detector has a grounded cathode grid on the bottom, a gate grid a few mm below the liquid-gas interface, and an anode grid a few mm above the interface. A negative potential applied to the cathode produce an electric field in the LXe volume to drift the generated electrons to the gas xenon (GXe) volume. A stronger electric field between the

gate grid and the anode extracts the electrons into the gas phase. Two photomultiplier tube (PMT) arrays, one below the cathode and one above the anode, detect the signals generated in the detector.

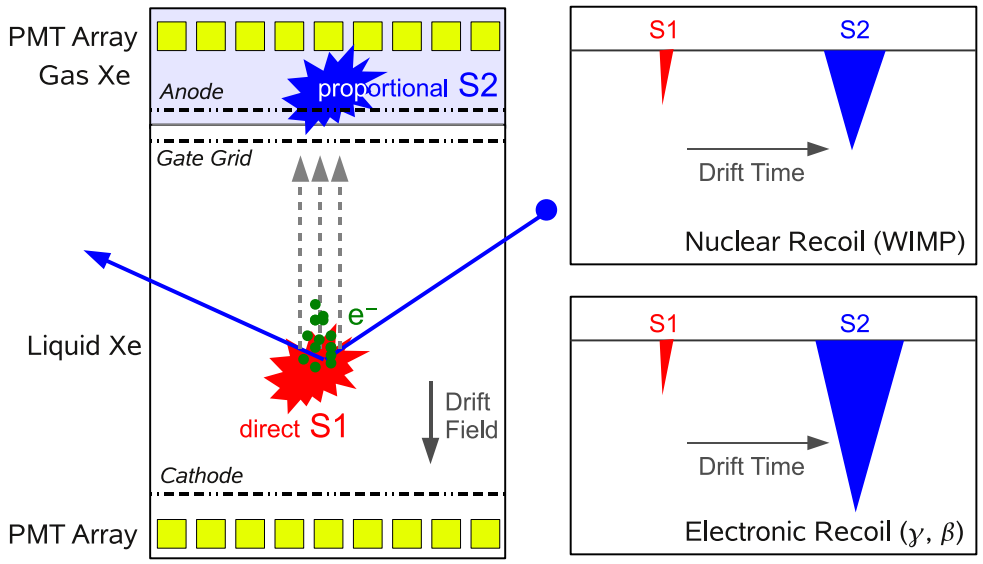

Figure 1.8: Operation principle of the dual-phase XENON100 detector (left). The waveforms of a nuclear recoil event (right, top) and electronic recoil (right, bottom). Figure from [Aprile *et al.*, 2012b].

The scintillation light directly produced by radiation, or the prompt scintillation signal (S1), is detected by the PMTs immediately. On the other hand, the ionized electrons are drifted upward by the electric field and produce scintillation light in the gas xenon volume. This signal is referred to as the proportional scintillation signal (S2) and is also detected by the PMTs. The finite drift velocity of the electrons causes a time difference between the S1 and the S2 signals, which is used in estimating the vertical coordinate of the interaction. Electronic recoils, which are from gamma and beta background events, and nuclear recoils, which are from WIMP and neutron events, have different S2/S1 ratios (Fig. 1.8 (right)). This feature allows a rejection of the majority of the gamma and beta particle background with an efficiency around 99.5 % at 50 % nuclear recoil acceptance [Aprile *et al.*, 2012b].

1.3.3 The XENON100 detector

The XENON dark matter experiments are operated at the INFN Laboratori Nazionali del Gran Sasso (LNGS) underground laboratory. Table 1.1 summarizes the series of three recent XENON experiments. In this subsection, we address the XENON100 detector and its subsystems.

Table 1.1: A series of XENON dark matter experiments [Aprile *et al.*, 2012a; Aprile *et al.*, 2010].

	Period of Operation	LXe mass [kg]	Sensitivity
XENON10	2005 - 2007	25	8.8×10^{-44} cm^2 for 100 GeV/c^2
XENON100	2007 - 2013	165	2×10^{-45} cm^2 for 55 GeV/c^2
XENON1T	2015 -	2.2×10^3	2.0×10^{-47} cm^2 for 50 GeV/c^2

XENON100 was designed to increase the fiducial mass by a factor of ten and to reduce the electromagnetic background by two orders of magnitude, compared to its predecessor XENON10. A drawing of the XENON100 dark matter detector is shown in Fig. 1.9. The cylindrical XENON100 TPC of 30.5 cm height and 15.3 cm radius contains an active target of 65 kg surrounded by 105 kg of LXe active veto. The walls made of 24 panels of polytetrafluoroethylene (PTFE, Teflon) circumscribe the cylindrical volume and separate it from an active LXe veto shield. PTFE is an electrical insulator and a good reflector for the VUV scintillation light [Yamashita *et al.*, 2004].

XENON100 detects the scintillation signal and the proportional signal using 1 inch square Hamamatsu R8520-06-Al PMTs, selected for low radioactivity and high quantum efficiency. The top PMT array where 98 PMTs are held in a concentric PTFE structure is placed above the target in the xenon gas. The bottom PMT array which consists of 80 PMTs arranged as closely as possible is located below the cathode, immersed in the LXe. As a LXe dark matter experiment is operated at cryogenic temperatures, a reliable cooling system with long-term stability is required. For this purpose, XENON100 uses a pulse tube refrigerator (PTR) Iwatani PC150, driven by a 6.5 kW helium compressor. The cooling power for this combination is measured to be 200 W at 170 K [Aprile *et al.*, 2012b].

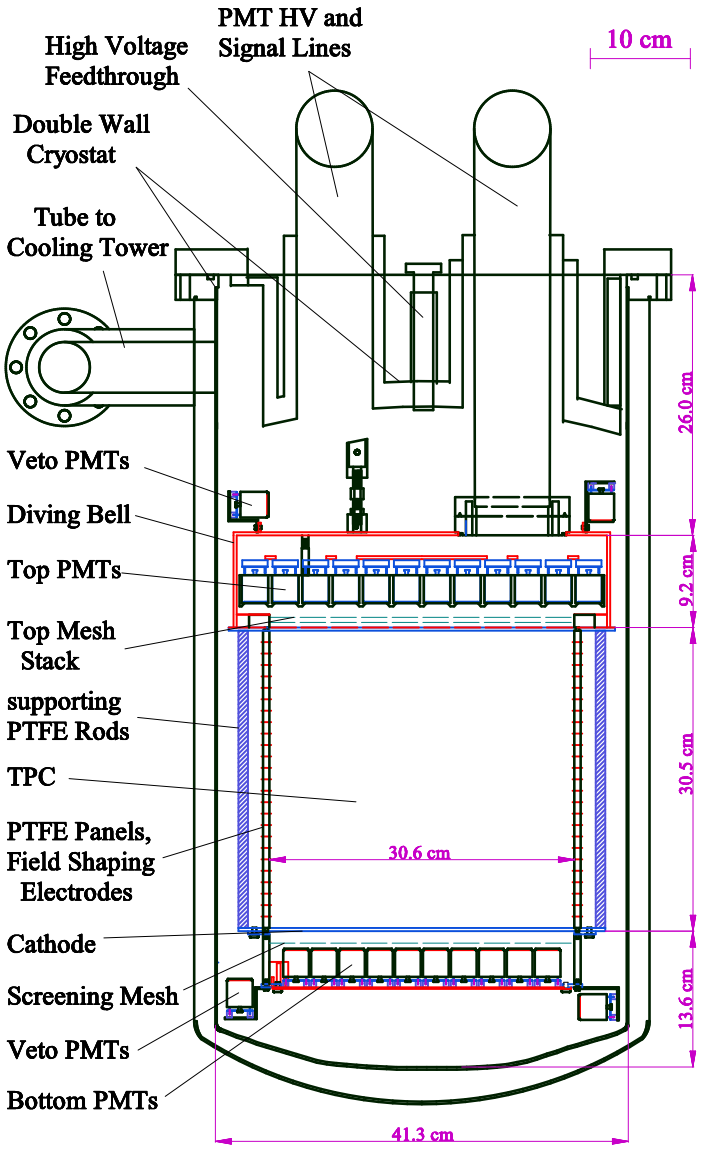

Figure 1.9: Schematic of the XENON100 dark matter detector. Figure.re from [Aprile *et al.*, 2012b]

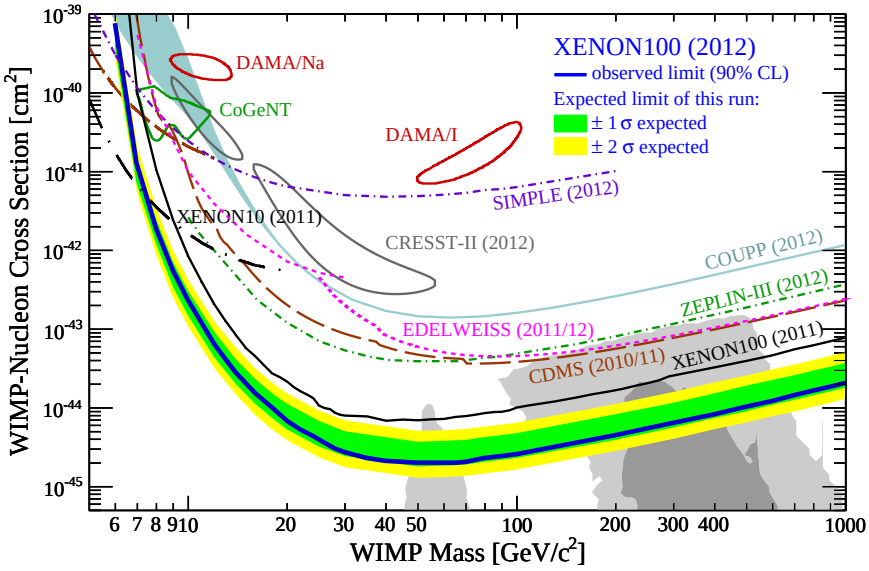

Figure 1.10: Results on the spin-independent WIMP-nucleon scattering cross section from XENON100. Figure from [Aprile *et al.*, 2012a]

The data from XENON100 lead to the upper limit on the spin independent WIMP-nucleon cross section (σ_{SI}) with a minimum at 2×10^{-45} cm^2 for a 55 GeV/c^2 WIMP mass, which corresponds to the present best experimental upper limit set on σ_{SI} [Aprile *et al.*, 2012a]. Figure 1.10 describes the results from XENON100 and a set of other experiments for comparison. The next generation LXe experiment, XENON1T, is currently under construction. XENON1T projects the cross section σ_{SI} upper limit of 2.0×10^{-47} cm^2 at 50 GeV/c^2 with a 2.2 ton LXe target.

1.4 Background in XENON100

1.4.1 Background sources

As XENON100 aims to improve the sensitivity compared to XENON10, the reduction of the background is critical. In the detector, WIMPs scatter off xenon nuclei and produce low energy nuclear recoils. Nuclear recoils of similar energy can also be produced by neutrons passing through the detector, whereas gamma rays and electrons lead to electronic recoils. As previously mentioned, electronic recoils are distinguished from nuclear recoils via the

S1/S2 ratio. XENON100 rejects more than 99% of electronic recoils at 50% nuclear recoil acceptance [Aprile *et al.*, 2010; Aprile *et al.*, 2011]. Despite this rejection efficiency, a small fraction of electronic recoils may statistically leaks into the nuclear recoil region and resemble a WIMP signal.

The presence of impurities such as oxygen or other electro-negative impurities in LXe decreases the size of both S1 and S2 signals. Therefore, xenon in the detector is purified by recirculating the xenon gas through a high temperature zirconium getter (SEAS MonoTorr PS3-MT3-R/N-1/2) (Fig. 1.11). While the GXe circulates, impurities in the xenon gas chemically bond to the getter material and dissipate. LXe extracted from the bottom of the detector vessel evaporates in the gas line and passes through the getter by a double diaphragm pump (KNF N143.12E) at a rate of about 5 standard liter per minute (SLPM) [Aprile *et al.*, 2012b].

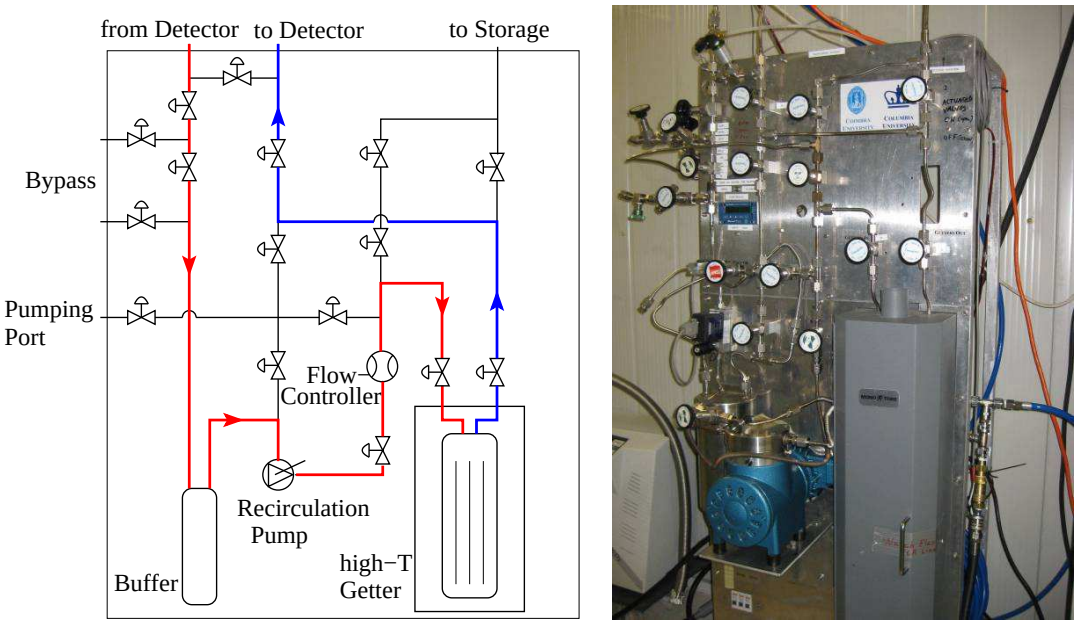

Figure 1.11: Schematic of the XENON100 purification system (left, figure from [Aprile *et al.*, 2012b]) and image of the gas panel (right). The arrows in the schematic indicate gas flow in the detector operation.

During the commissioning phase of XENON100, the detector was heated to 50°C, the temperature limit set by the PMTs, to speed up the purification process before the first filling with LXe. In the meantime, a residual gas analyzer (RGA) monitored the detector vacuum. Then the detector was cleaned with hot GXe at a 2 atm pressure, as xenon is known as a good solvent due to its polarizability [Rentzepis and Douglass, 1981]. The purification was performed for several weeks by reheating the detector while the warm xenon gas passed through the getter. During this process, decrease of the water content from ∼500 part per billion (ppb) to 1 ppb level was monitored with a dedicated detector (Tigeroptics HALO) using the spectral absorption technique [Aprile *et al.*, 2012b].

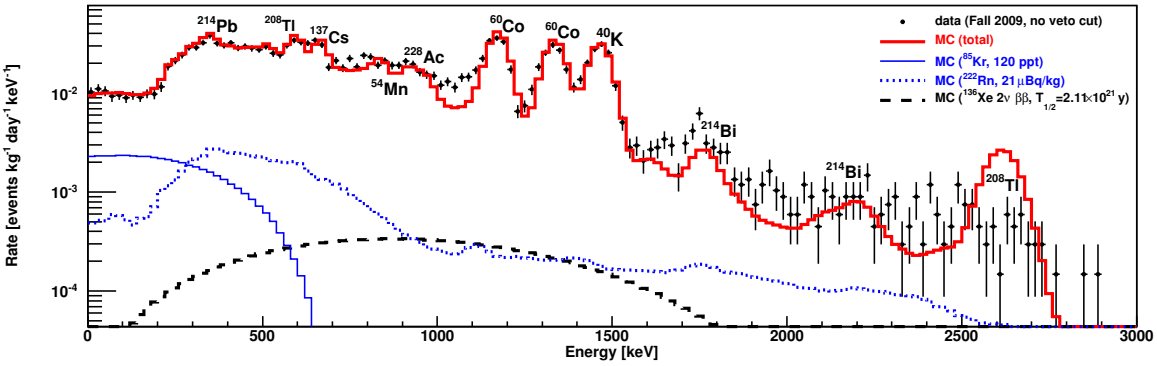

Figure 1.12: Energy spectra of the background from measured data and Monte Carlo simulations in a 30 kg fiducial volume without a veto cut (thick red solid line). Cosmogenic activation of LXe is not included. The energy spectra of ^{85}Kr and ^{222}Rn decays in LXe are shown with the thin blue solid and dotted lines, respectively. The thin black dashed histogram shows the theoretical spectrum of the 2ν double beta decay of ^{136}Xe, assuming a half-life of 1.1×10^{22} years. Figure from [Aprile *et al.*, 2011].

Electronic recoil backgrounds in XENON100 are mainly caused by several sources: radioactive contamination of the materials of the detector and the shield, intrinsic radioactivity in the LXe medium, and the decays of ^{222}Rn and its progeny inside the detector shield. All detector components were selected to minimize the contamination by radioactive materials. The electronic recoil background of XENON100 is estimated by GEANT4 simulations

with details of geometry and materials. Figure 1.12 shows the simulated background in a 30 kg fiducial volume with the measured data [Aprile *et al.*, 2010]. In the low energy region, below 700 keV, the simulated background shows good agreement with the measured background.

While the background stemming from radioactive materials in the detector and shield materials can be reduced by a fiducial volume cut, the intrinsic background from radioactive isotopes in the LXe is a fundamental limitation to the experiment sensitivity. Table 1.2 presents predicted electronic recoils from the detector and shield materials and the intrinsic radioactive impurities in the energy region of interest. In the 30 kg fiducial volume, ^{85}Kr contributes ∼30% to the total background without veto cut and 55% when a veto coincidence is applied below a threshold energy of 100 keV. In other words, ^{85}Kr becomes the dominant source of the electronic recoil background after selecting an optimized fiducial volume and an active veto cut [Aprile *et al.*, 2011].

Table 1.2: Summary of the predicted electronic recoil background: rate of single scatter events in the energy region below 100 keV, before S2/S1 discrimination. The veto cut with an average energy threshold of 100 keV has been applied. Table from [Aprile *et al.*, 2011].

	Predicted rate [$\times 10^{-3}$ events·kg^{-1}·day^{-1}·keV^{-1}]					
Volume	62 kg target		40 kg fiducial		30 kg fiducial	
Veto cut	none	active	none	active	none	active
Detector and shield materials	137.22	75.30	12.89	3.42	7.22	2.02
^{222}Rn in the shield (1 Bq/m^3)	5.95	1.72	0.92	0.16	0.16	0.02
^{85}Kr in LXe (150 ppt of ^{nat}Kr)	2.90	2.90	2.90	2.90	2.90	2.90
^{222}Rn in LXe (21 μBq/kg)	1.04	0.51	0.56	0.38	0.53	0.37
All sources	147.11	80.43	17.27	6.86	10.81	5.31

1.4.2 Removal of ^{85}Kr from xenon

Radioactive decay of ^{85}Kr results in beta particle, with maximum energy of 687 keV, and this is the major source of electronic recoils in XENON100 as discussed in Sec. 1.4.1. ^{85}Kr

is artificially created in nuclear fission, and makes up $\sim 10^{-11}$ of the total krypton isotopes. The properties of krypton and specifically ^{84}Kr will be discussed in more detail in Sec. 2.2. Xenon gas extracted from the atmosphere contains krypton impurities at a part per million (ppm) level after distillation and absorption-based chromatography.

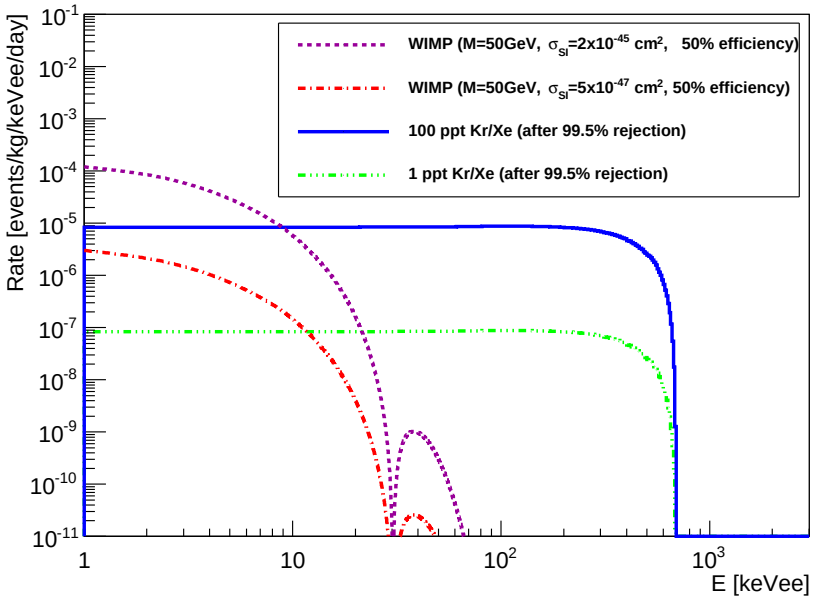

Figure 1.13: Differential scattering rates of weakly interacting massive particles (WIMPs) and decay rates of ^{85}Kr for XENON100 and XENON1T sensitivity goals.

The xenon gas used for XENON100 has been purified by a commercial cryogenic distillation plant (Spectra Gases Co.) to reduce the krypton concentration level to $\sim$ 10 ppb. This concentration level still needs to be reduced by a factor of 100 as krypton impurities at the 100 part per trillion (ppt) level in the xenon gas would contribute a rate of $\sim 2 \times 10^{-3}$ events $\times$ kg $\times$ keV$_{\rm ee}{}^{-1} \times$ day^{-1} from ^{85}Kr [Aprile *et al.*, 2011]. The expected rates of WIMP events for XENON100 and XENON1T are shown in Fig. 1.13, along with the rates of electronic recoils due to ^{85}Kr. The blue solid line indicates the Kr/Xe level required to achieve the projected sensitivity of the XENON100 experiment, 100 ppt, and the green dashed line presents that for XENON1T, 1 ppt.

As XENON100 is the first low background experiment using a large quantity of LXe, a

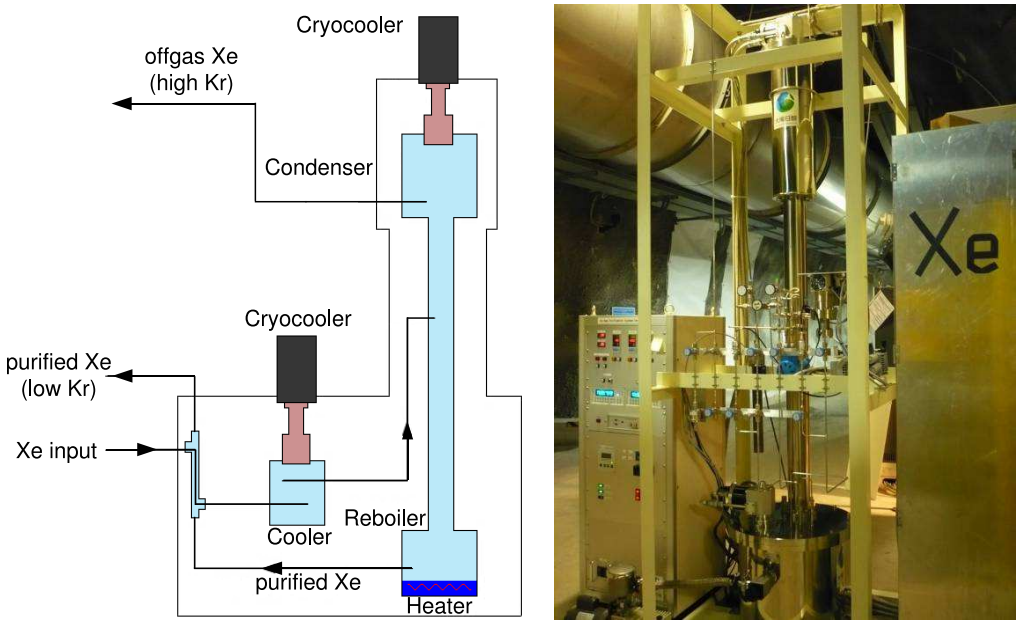

Figure 1.14: Cryogenic distillation column used to separate krypton (left, figure from [Aprile *et al.*, 2012b]) and an image of the setup (right). The XENON column has a height of about 3 m.

krypton contamination at ultra-low levels is critical to the sensitivity of the experiment. In order to further reduce krypton impurities in the xenon, a small-scale cryogenic distillation column was integrated into the XENON100 system underground. The column is designed to reduce the krypton concentration by a factor of 1000 in a single pass, at a purification speed of 1.8 SLPM (or 0.6 kg/h). A schematic and an image of the cryogenic distillation column are shown in Fig. 1.14. The xenon gas is cooled using a cryocooler before entering the column at half height. A thermal gradient is kept constant using a heater at the bottom of the column and a cryocooler at the top. Due to the different boiling temperatures of krypton (120 K at 1 atm) and xenon (165 K), a krypton-enriched mixture stays at the top of the column and a krypton-depleted one at the bottom. The high krypton concentration xenon is separated by freezing it into a gas bottle, and the purified xenon at the bottom is used for the experiment [Lim, 2013].

After installation and the initial commissioning run of the new column, the second

distillation of the full xenon inventory was performed in the summer of 2009. For the commissioning run, the krypton concentration in xenon was measured with a delayed coincidence analysis at 143^{+135}_{-90} ppt (90% CL) [Aprile *et al.*, 2010], which agrees with the value inferred from a comparison of the measured background spectrum with a Monte Carlo simulation [Aprile *et al.*, 2011]. In the second science run [Aprile *et al.*, 2012a], the krypton contamination was lowered to (19 $\pm$ 4 ppt), measured by ultrasensitive rare gas mass spectroscopy. This agrees with the value (18 $\pm$ 8 ppt) derived from the analysis of delayed β-γ coincidences associated with the ^{85}Kr beta decay. The krypton contamination of xenon samples, recently drawn from the XENON100 detector, was measured to be below 1 ppt from a mass spectroscopic technique [Lindemann and Simgen, 2013].

Chapter 2

Atomic properties

This work aims to determine the ppt-level contamination by krypton in the xenon sample from the XENON dark matter experiment. Argon gas is used to avoid contamination by krypton for the testing phase. The three relevant elements, argon, krypton, and xenon, are noble gases with a full outer shell of valence electrons in the ground state, leading to several common properties. Prior to describing the atom trap trace analysis (ATTA) system, the properties of these elements are presented in this chapter.

2.1 Argon

Argon, whose atomic number is 18, was discovered by Lord Rayleigh and Sir William Ramsay in 1894. Argon exists in a gas phase at standard temperature and pressure (STP) with the melting point of 83.80 K and the boiling point of 87.30 K at 1 atm. It is the third most common gas in air, making up 0.93% of the earth's atmosphere [Haynes, 2013]. Argon has 3 stable and 21 unstable isotopes with the electron configuration of $1s^2 2s^2 2p^6 3s^2 3p^6$. Table 2.1 describes physical properties of argon and the abundances of its selected isotopes. Argon is inert and it is not known to form any stable compounds at room temperature [Haynes, 2013]. Table 2.2 displays some excited states of argon and their electronic configurations with energies, and the energies of each state are also drawn in Fig. 2.1.

Argon is produced industrially by the fractional distillation of liquid air, and is widely used where an inert gas is needed since it is the most abundant and cheapest noble gas.

Table 2.1: Physical properties of argon.

Property	Value
Atomic number Z	18
Molar mass	39.948 g mol^{-1}
Isotopic properties	^{36}Ar (0.337 %, stable), ^{38}Ar (0.063 %, stable)
	^{39}Ar (trace, β^- decay, $t_{1/2}$=35 d)
	^{40}Ar (99.6 %, stable)
	^{41}Ar (synthetic, β^- decay, $t_{1/2}$ = 109.34 min)
Gas density (273.15 K, 1 atm)	1.784 g cm^{-3}
Liquid density (87.30 K, 1 atm)	1.40 g cm^{-3}
Melting point (1 atm)	83.80 K
Boiling point (1 atm)	87.30 K
Triple point	83.81 K, 0.68 atm, 3.08 g cm^{-3}
Critical point	150.87 K, 48.34 atm, 1.155 g cm^{-3}

The property of plasma discharge makes argon used in electric light bulbs and in fluorescent tubes based on plasma discharge. It is also used in arc welding and cutting to protect the weld or cut area from atmospheric contamination. In scientific applications, some direct dark matter searches such as ArDM use argon as the target material to interact with weakly interacting massive particles (WIMPs).

2.1.1 ^{40}Ar

As mentioned in the first part of this chapter, we use ^{40}Ar for testing and optimizing the system before detecting ^{84}Kr in the xenon sample. ^{40}Ar, containing 18 protons and 22 neutrons, is the most common isotope (99.6% of all argon in nature), and has an atomic mass of 39.9624. This isotope is produced via decay of ^{40}K, which is a radioactive isotope of potassium with a half-life of 1.25×10^9 years. About 88.8% of the time, naturally occurring ^{40}K transforms to stable ^{40}Ca by emitting a β particle and an antineutrino. In the other cases (11.2%), it decays to stable ^{40}Ar by electron capture with a gamma ray

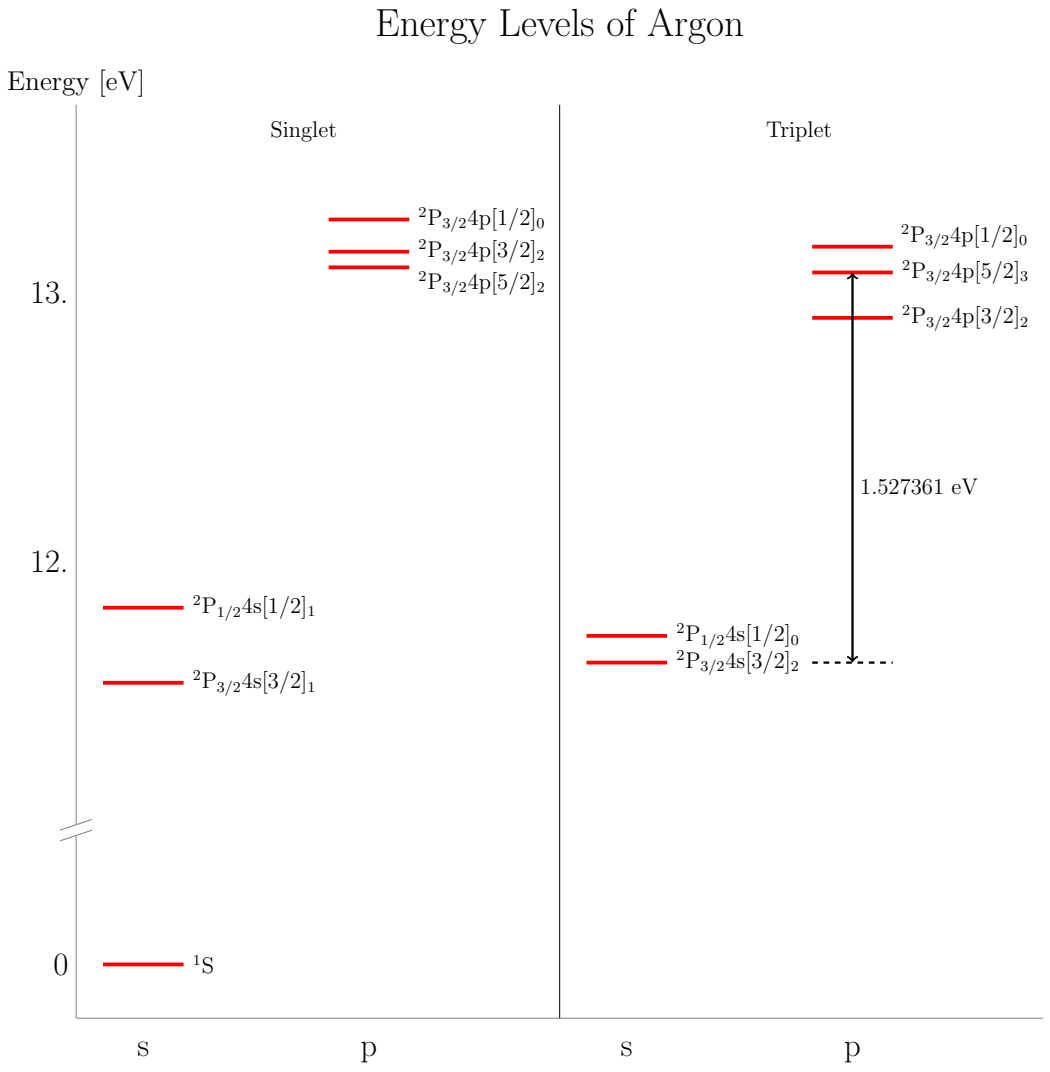

Figure 2.1: Grotrian diagram of argon. The black arrow indicates the transition used for cooling and trapping.

Table 2.2: Energy levels of neutral argon.

Electron Configuration	Spin Configuration	$^{2S+1}L_j nl[K]_J$	Energy [eV]
$3s^2 3p^6$			0
$3s^2 3p^5 4s^1$	triplet	$^2P_{3/2}4s[3/2]_2$ [a]	11.548354
$3s^2 3p^5 4s^1$	singlet	$^2P_{3/2}4s[3/2]_1$	11.623592
$3s^2 3p^5 4s^1$	triplet	$^2P_{1/2}4s[1/2]_0$	11.723160
$3s^2 3p^5 4s^1$	singlet	$^2P_{1/2}4s[1/2]_1$	11.828071
$3s^2 3p^5 4p^1$	triplet	$^2P_{3/2}4p[1/2]_1$	12.907015
$3s^2 3p^5 4p^1$	singlet	$^2P_{3/2}4p[1/2]_0$	13.273038
$3s^2 3p^5 4p^1$	triplet	$^2P_{3/2}4p[5/2]_3$ [a]	13.075715
$3s^2 3p^5 4p^1$	singlet	$^2P_{3/2}4p[5/2]_2$	13.094872
$3s^2 3p^5 4p^1$	singlet	$^2P_{3/2}4p[3/2]_2$	13.153143
$3s^2 3p^5 4p^1$	triplet	$^2P_{3/2}4p[3/2]_1$	13.171777

[a] Transition between these two levels is used for cooling and detection.

and a neutrino or rarely by emitting a position and a neutrino. This decay ratio is used to determine radiometric dates for geological events [McDougall, 1999].

2.2 Krypton

Krypton is an element in the group of noble gases, with an atomic number 36. Ramsay and Travers discovered krypton in 1898 in the residue left after liquid air had nearly boiled away [Haynes, 2013]. Krypton is present in the air at the ∼1 ppm level, and has 6 stable isotopes and 30 unstable isotopes. Table 2.3 shows physical properties of krypton with a list of selected isotopes. Ground state krypton has an electron configuration of $3d^{10}4s^2 4p^6$ containing that of the ground state argon. The configurations of several excited states and their energies are listed in Tab. 2.4, and Fig. 2.2 shows the energy diagram.

Krypton, characterized by its several sharp emission lines including the brilliant green and orange, is used in lighting like other noble gases. Ionized krypton gas discharges appear whitish due to its multiple emission lines. Using this feature, krypton can be used in

Table 2.3: Physical properties of krypton.

Property	Value
Atomic Number Z	36
Molar mass	83.798 g mol^{-1}
Isotopic Abundance	^{78}Kr (0.35 %, β^+ decay, $t_{1/2} > 1.1 \times 10^{20}$ y)
	^{79}Kr (0.35 %, ϵ β^+ γ decay, $t_{1/2} = 35.04$ h)
	^{80}Kr (2.25 %, stable)
	^{81}Kr (trace, ϵ γ decay, $t_{1/2} = 2.29 \times 10^5$ y)
	^{82}Kr (11.6 %, stable)
	^{83}Kr (11.5 %, stable)
	^{84}Kr (57.0 %, stable)
	^{85}Kr (trace, β^- decay, $t_{1/2} = 10.765$ y)
	^{86}Kr (17.3 %, stable)
Gas density (273 K, 1 atm)	3.749 g cm^{-3}
Liquid density (165.05 K, 1 atm)	2.413 g cm^{-3}
Melting point (1 atm)	115.79 K
Boiling point (1 atm)	119.93 K
Triple point	115.775 K, 0.722 atm, 3.08 g cm^{-3}
Critical point	209.42 K, 54.28 atm, 1.155 g cm^{-3}

photographic projection lamps as a brilliant white light source. The relative abundance of krypton versus hydrogen can be used by astronomers to measure how much nucleosynthesis has taken place in any region of interstellar space [Cartledge *et al.*, 2008]. One of the stable isotopes, ^{86}Kr, was used for definition of the fundamental unit of length. In 1960, the General Conference on Weights and Measures (*Confrence Gnrale des Poids et Mesures*, CGPM) defined the meter based on the wavelength of ^{86}Kr radiation. (In 1983, it was replaced with the length of the path traveled by light in vacuum during a time interval of 1/299,792,458 s [Taylor and Thompson, 2008].)

Table 2.4: Energy levels of neutral krypton.

Electron Configuration	Spin Configuration	$^{2S+1}L_j nl[K]_J$	Energy [eV]
$4s^2 4p^6$			0
$4s^2 4p^5 5s^1$	triplet	$^2P_{3/2} 5s[3/2]_2$ [a]	9.915231
$4s^2 4p^5 5s^1$	singlet	$^2P_{3/2} 5s[3/2]_1$	10.032400
$4s^2 4p^5 5s^1$	triplet	$^2P_{1/2} 5s[1/2]_0$	10.562413
$4s^2 4p^5 5s^1$	singlet	$^2P_{1/2} 5s[1/2]_1$	10.643634
$4s^2 4p^5 5p^1$	triplet	$^2P_{3/2} 5p[1/2]_1$	11.303454
$4s^2 4p^5 5p^1$	singlet	$^2P_{3/2} 5p[1/2]_0$	11.666027
$4s^2 4p^5 5p^1$	triplet	$^2P_{3/2} 5p[5/2]_3$ [a]	11.443046
$4s^2 4p^5 5p^1$	singlet	$^2P_{3/2} 5p[5/2]_2$	11.444655
$4s^2 4p^5 5p^1$	singlet	$^2P_{3/2} 5p[3/2]_2$	11.526115
$4s^2 4p^5 5p^1$	triplet	$^2P_{3/2} 5p[3/2]_1$	11.545822

[a] Transition between these two levels is used for cooling and detection.

2.2.1 ^{85}Kr

^{85}Kr, containing 49 neutrons and 36 protons, is produced mainly by fission of uranium and plutonium in nuclear reactors and released during chopping and dissolution of fuel rods in nuclear reprocessing, and the interaction of cosmic rays with stable ^{84}Kr also generates a small quantity of ^{85}Kr. Currently, artificially produced ^{85}Kr overwhelms the cosmogenic

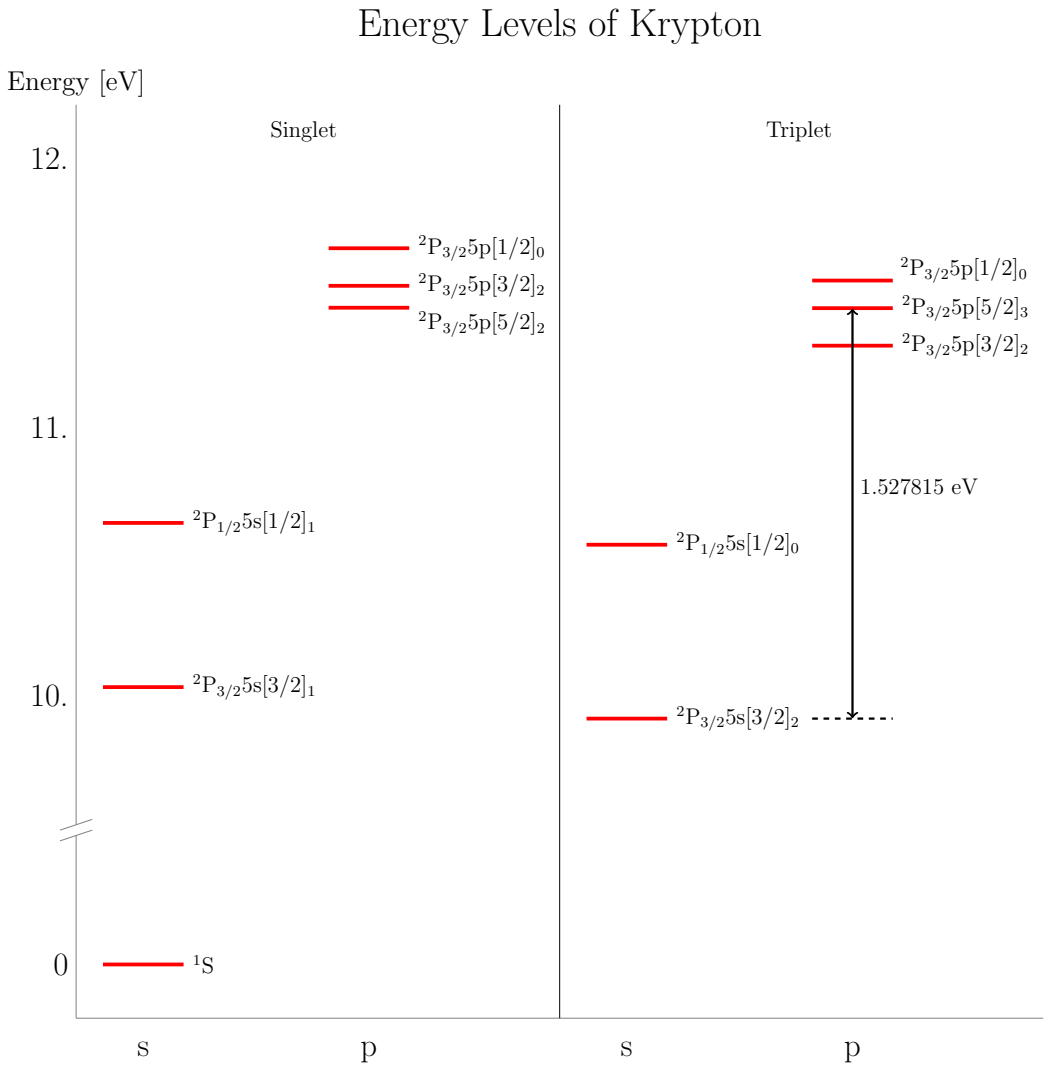

Figure 2.2: Grotrian diagram of krypton. The black arrow indicates the transition used for cooling and trapping.

production of ^{85}Kr. This isotope is the most abundant man-made radioisotope in the troposphere [Schroder *et al.*, 1971]. ^{85}Kr, once released into the atmosphere, diminishes only via radioactive decay where it transforms into ^{85}Rb with a half-life of 10.76 years and a maximum energy of 0.687 MeV (Tab. 2.3). The global atmospheric content has been continuously increasing since the installation of reprocessing plants for nuclear fuel in the early 1950s and reached 5.5×10^{15} Bq at the end of 2009 [Ahlswede *et al.*, 2013]. Figure 2.3 shows the increase of the global ^{85}Kr inventory with time. The current isotopic abundance of ^{85}Kr in the atmosphere is at the level of 10^{-11}.

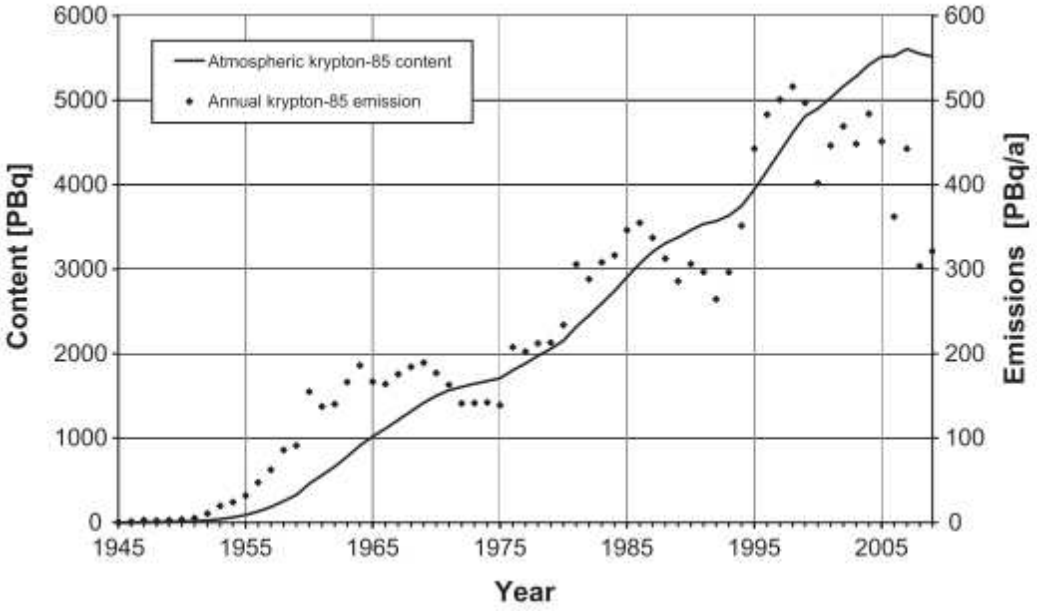

Figure 2.3: Global accumulated ^{85}Kr inventory (radioactive decay accounted for) and the annual emissions. The emissions unit is PBq = 10^{15} Bq = 10^{15} s^{-1}. Figure from [Ahlswede *et al.*, 2013].

The radioactive properties of ^{85}Kr, combined with accumulated data of its global observations since the 1950s, allow us use the isotope as a tracer in environmental samples. Researchers use ^{85}Kr to estimate the age of young groundwater (< 40 years). For a groundwater system with small dispersion, the age of groundwater can be estimated directly from ^{85}Kr activity [Ekwurzel *et al.*, 1994]. Global observation of ^{85}Kr is used to calibrate and examine atmospheric transport models [Levin and Hesshaimer, 1996], and a temporal and

spatial concentration of ^{85}Kr gives an indication of a nuclear leak accident or an undeclared plutonium stockpile [Hippel *et al.*, 1985].

^{85}Kr has several industrial applications. For example, ^{85}Kr is allowed to diffuse into extremely small cracks, where the atoms are trapped and detected by normal photographic techniques. This method is called krypton gas penetrant imaging [Glatz, 1996]. Another usage of ^{85}Kr is as an additive in arc discharge lamps. It is known that the presence of ^{85}Kr in discharge tubes makes the lamps easy to ignite by reducing their starting voltage [Linde Electronics and Specialty Gases, 2010].

2.2.2 ^{84}Kr

^{84}Kr is the most abundant krypton isotope with the natural abundance of 57%. In this experiment, ^{84}Kr is detected to take advantage of its large abundance. ^{84}Kr is stable and thus has no decay products. It contains 48 neutrons and 36 protons, which leads to the atomic mass of 83.9115.

2.3 Xenon

Xenon, a heavy noble gas with an atomic number of 54, was first found by Ramsay and Travers in 1898 in the residue left after evaporating liquid air components. Xenon is a colorless, odorless monatomic gas under STP as the other noble gases. It is present at about one part in twenty million in the atmosphere [Haynes, 2013]. Xenon consists of 9 stable isotopes and 35 unstable isotopes that radioactively decay. Physical properties of xenon and its isotopes are summarized in Tab. 2.5. Though Xe gas is generally inert, a few chemical reactions are known such as the formation of xenon hexafluoroplatinate, the product of platinum hexafluoride and xenon [Bartlett, 1962]. The electron configuration of the ground state xenon is $5s^2 4d^{10} 5p^6$ containing that of the ground state krypton. Xenon is obtained as a byproduct of the separation of air into oxygen and nitrogen. The resulting liquid oxygen mixture contains both krypton and xenon, which are extracted by fractional distillation, and at the last stage, xenon is extracted from the krypton-xenon mixture by distillation. The typical price of xenon is about 1000 $/kg; its rarity makes it much more

expensive than other noble gases [Plante, 2012].

Table 2.5: Physical properties of xenon. Table from [Plante, 2012].

Property	Value
Atomic Number Z	54
Molar mass	131.29 g mol^{-1}
Isotopic Abundance	^{124}Xe (0.095%, β^+ decay, $t_{1/2} > 4.8 \times 10^{16}$ y)
	^{126}Xe (0.89%, stable), ^{129}Xe (26.4%, stable)
	^{130}Xe (4.07%, stable), ^{131}Xe (21.2%, stable)
	^{132}Xe (26.9%, stable)
	^{134}Xe (10.4%, β^- decay, $t_{1/2} > 1.1 \times 10^{16}$ y)
	^{136}Xe (8.86%, β^- decay, $t_{1/2} = 2.11 \times 10^{21}$ y)
Gas density (273.15 K, 1 atm)	5.8971 g cm^{-3}
Liquid density (165.03 K, 1 atm)	3.057 g cm^{-3}
Melting point (1 atm)	161.4 K
Boiling point (1 atm)	165.03 K
Triple point	161.31 K, 0.805 atm, 3.08 g cm^{-3}
Critical point	289.74 K, 57.65 atm, 1.155 g cm^{-3}

Xenon has a number of applications despite its high price. Xenon excited by an electrical discharge creates a characteristic blue glow. It is used in gas-discharge lamps such as xenon flash lamps, arc lamps, and plasma displays. Xenon-containing dimers (Xe_2, XeCl, XeF, etc.) are used in excimer lasers to provide stimulated emission. In science, xenon is used in calorimeters for measurements of gamma rays and as a medium for dark matter searches such as XENON and LUX.

Chapter 3

Basic concepts

In this experiment, we cool and trap atoms of interest to count their number in a given quantity of carrier atoms. Standard cooling and trapping methods used here are based on the interaction between light and nearly two-level atoms. In this chapter, we review the basic principle of light-atom interaction and the details of each cooling and trapping techniques: transverse cooling, Zeeman slowing, and magneto-optical trapping.

3.1 Light forces on atoms

An atom in the presence of light can be described by the time-dependent Schrödinger equation

$$\mathrm{i}\hbar\frac{\partial\Psi}{\partial t} = H\Psi, \tag{3.1}$$

where H is the Hamiltonian operator. The Hamiltonian has the time independent field-free atomic part, H_0, and the time dependent atom-light interaction part, H_I. Thus, $H = H_0 + H_I$.

For a two-level atom and no external field, the Hamiltonian is time independent in the Schrödinger picture, and the Schrödinger equations for each level are

$$\begin{aligned} H_0\psi_1(\vec{r}) &= E_1\psi_1(\vec{r}), \\ H_0\psi_2(\vec{r}) &= E_2\psi_2(\vec{r}), \end{aligned} \tag{3.2}$$

where E_1 and E_2 are the energies of the levels. Then we can express the wavefunction time

evolution as

$$\begin{aligned}\Psi(\vec{r},t) &= c_1\ \psi_1(\vec{r})\ e^{-iE_1t/\hbar} + c_2\ \psi_2(\vec{r})\ e^{-iE_2t/\hbar} \\ &= c_1\ |1\rangle\ e^{-i\omega_1 t} + c_2\ |2\rangle\ e^{-i\omega_2 t},\end{aligned} \tag{3.3}$$

where $\omega_1 = E_1/\hbar$ and $\omega_2 = E_2/\hbar$.

An electric field $\vec{E}$ due to the light produces the perturbation term

$$H_I = -\vec{d}\cdot\vec{E}, \tag{3.4}$$

where $\vec{d}$ is the electric dipole moment $\vec{d} = -e\,\vec{r}$. From this Hamiltonian, the Rabi frequency Ω is defined as

$$\Omega = \frac{\langle 2|\vec{d}\cdot\vec{E}|1\rangle}{\hbar}. \tag{3.5}$$

Now, we introduce the density matrix

$$\rho = |\Psi\rangle\langle\Psi| = \begin{pmatrix} c_1 \\ c_2 \end{pmatrix}\begin{pmatrix} c_1^* & c_2^* \end{pmatrix} = \begin{pmatrix} \rho_{11} & \rho_{12} \\ \rho_{21} & \rho_{22} \end{pmatrix}. \tag{3.6}$$

The diagonal elements ρ_{11} and ρ_{22} are the populations of the states $|1\rangle$ and $|2\rangle$. The off-diagonal elements, called coherences, represent the response of the system at the driving frequency. Then Eq. 3.1 can be written as

$$i\hbar\frac{\mathrm{d}\rho}{\mathrm{d}t} = [H,\rho]\,. \tag{3.7}$$

For convenience, we define new variables

$$\begin{aligned} u &= \widetilde{\rho}_{12} + \widetilde{\rho}_{21}, \\ v &= -i(\widetilde{\rho}_{12} - \widetilde{\rho}_{21}), \\ w &= \rho_{11} - \rho_{22}, \end{aligned} \tag{3.8}$$

where $\widetilde{\rho}_{12} \equiv \rho_{12}\,\exp(-i\delta t)$ and $\widetilde{\rho}_{21} \equiv \rho_{21}\,\exp(i\delta t)$. Here, $\delta = \omega_l - \omega_0$ is the detuning of the light, ω_l is the light frequency, and $\omega_0 = (E_2 - E_1)/\hbar$ is the atomic transition frequency.

The atoms in the excited state decay to the ground state and emit photons, both via stimulated and spontaneous emission. The process of spontaneous emission can be introduced phenomenologically as $\rho_{22}(t) = \rho_{22}\,\exp(-\Gamma t)$, where Γ is the atomic transition

linewidth. Equation 3.1 with the effect of spontaneous emission yields the following equations:

$$\begin{aligned} \dot{u} &= \delta v - \frac{\Gamma}{2}u, \\ \dot{v} &= -\delta u + \Omega\omega - \frac{\Gamma}{2}v, \\ \dot{w} &= -\Omega v - \Gamma(\omega - 1). \end{aligned} \tag{3.9}$$

These are the optical Bloch equations. For the steady state case ($t \gg \Gamma^{-1}$), their solution is

$$\begin{pmatrix} u \\ v \\ w \end{pmatrix} = \frac{1}{\delta^2 + \Omega^2 + \Gamma^2/4} \begin{pmatrix} \Omega\delta \\ \Omega\Gamma/2 \\ \delta^2 + \Gamma^2/4 \end{pmatrix} \tag{3.10}$$

By inserting this solution into the definition of w in Equation 3.8, we can derive the population ρ_{22} of the excited state,

$$\begin{aligned} \rho_{22} = \frac{1-w}{2} &= \frac{\Omega^2/4}{\delta^2 + \Omega^2 + \Gamma^2/4} \\ &= \frac{1}{2}\,\frac{I/I_{\text{sat}}}{1 + I/I_{\text{sat}} + (2\delta/\Gamma)^2}. \end{aligned} \tag{3.11}$$

In the second line of Equation 3.11 we introduced a new variable, the saturation intensity I_{sat}, which is defined as

$$\frac{I}{I_{\text{sat}}} = \frac{2\Omega^2}{\Gamma^2} \equiv s_0, \tag{3.12}$$

where s_0 is the on-resonance saturation parameter.

Now we can obtain an expression for the photon scattering rate in atom-light interactions. The scattering rate is expressed as

$$R_{\text{scatt}} = \Gamma\rho_{22} = \frac{\Gamma}{2}\,\frac{s_0}{1 + s_0 + (2\delta/\Gamma)^2}. \tag{3.13}$$

When a ground state atom absorbs a photon and is excited to an upper energy level, the momentum of the photon is transferred to the atom, and the atom receives a kick in the direction of the photon's propagation. When the excited atom returns to the original state via stimulated emission, the emitted photon has the same direction as the absorbed photon, and as a result, the overall momentum change of the atom during this cycle is zero. When the excited atom decays via spontaneous emission, however, a photon is emitted in

a random direction. Therefore, the momentum change due to spontaneous emissions will cancel out, and only effects from photon absorption are accumulated after a large number of cycles. This results in the scattering force, and its magnitude is a product of the incoming photon momentum and the rate of the interactions.

$$\begin{aligned} F_{\text{scatt}} &= p_{\text{photon}} \times R_{\text{scatt}} \\ &= \hbar k \frac{\Gamma}{2} \frac{s_0}{1 + s_0 + (2\delta/\Gamma)^2}. \end{aligned} \tag{3.14}$$

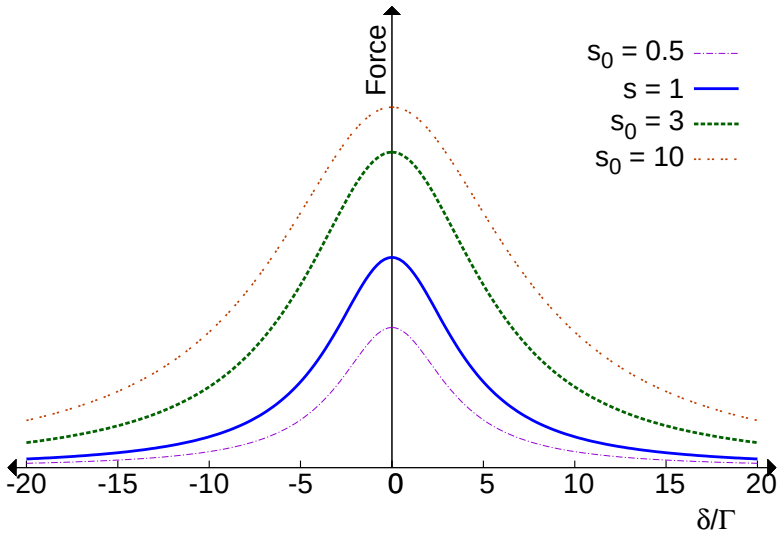

Figure 3.1: Magnitude of the scattering force exerted on an atom via atom-photon interactions as a function of the light detuning.

Figure 3.1 shows the light force on atoms as a function to the light frequency detuning for different light intensities. The scattering force has its maximum value when the light frequency is on resonance as expected, and the line is broadened at high intensities.

3.2 Optical molasses

3.2.1 Principle of optical molasses

In Sec. 3.1, we discussed the interaction between a laser photon and a stationary two-level atom. For a moving atom, the interaction is affected by the Doppler effect. If the atom

is moving toward the light source with velocity v (Fig. 3.2), the frequency of the laser appears blue-shifted to the atom, $\omega_l \rightarrow \omega_l + kv$. In other words, the atomic resonance appears at $\omega_0 \rightarrow \omega_0 - kv$ to the photon. We take the latter notation in the rest part of this thesis. The Doppler effect modifies the scattering force $F_{\text{scatt}}(\omega_l - \omega_0)$ to $F_{\text{scatt}}(\omega_l - \omega_0 + kv)$.

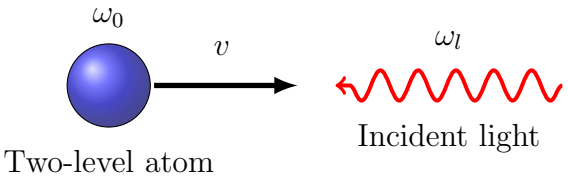

Figure 3.2: Schematic of atom-photon interaction for an atom moving toward the light source.

Optical molasses are set up by two counterpropagating laser beams that have the same frequency and intensity. When an atom moves with velocity v along the light propagation axis, the net force on the atom is expressed as the sum of the scattering forces from each laser,

$$F_{\text{molasses}} = F_{\text{scatt}}(\omega_l - \omega_0 - kv) - F_{\text{scatt}}(\omega_l - \omega_0 + kv). \tag{3.15}$$

For a low velocity condition, satisfying $kv \ll \Gamma$, this equation can be rewritten as

$$\begin{aligned} F_{\text{molasses}} &\simeq \left[F_{\text{scatt}}(\omega_l - \omega_0) - kv\frac{\partial F}{\partial \omega}\right] - \left[F_{\text{scatt}}(\omega_l - \omega_0) + kv\frac{\partial F}{\partial \omega}\right] \\ &= -2\frac{\partial F}{\partial \omega}kv. \end{aligned} \tag{3.16}$$

We define a new coefficient

$$\alpha \equiv 2k\frac{\partial F}{\partial \omega} = 4\hbar k^2 s_0 \frac{-2\delta/\Gamma}{[1 + s_0 + (2\delta/\Gamma)^2]^2}. \tag{3.17}$$

Then Eq. 3.16 is written in the form

$$F_{\text{molasses}} = -\alpha v, \tag{3.18}$$

where α is an effective damping coefficient that is analogous to a mechanical viscous damper in a damped harmonic oscillator setup.

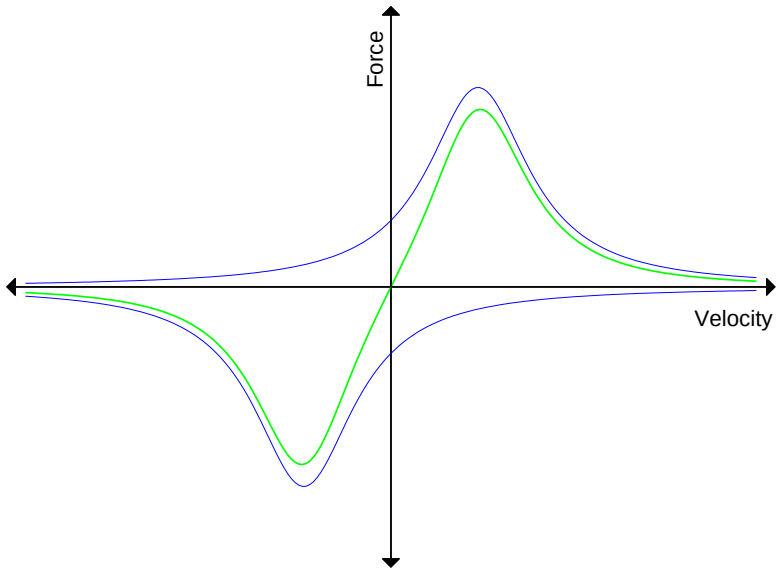

Figure 3.3: Optical molasses force as a function of atom velocity along the axis of light propagation. Blue lines are forces due to each counterpropagating light beam, and the green line is the net force.

Figure 3.3 shows the force exerted on an atom in optical molasses as a function of the atom's velocity. We see that the net force (green line) is almost linear in the small velocity region as Eq. 3.18 indicates. The force grows with velocity in this region. Beyond a certain threshold velocity, however, the net force falls and the optical molasses does not work properly.

3.2.2 The Doppler limit of optical molasses

The concept discussed in Sec. 3.2.1 seems to imply that any atoms with small velocities can be cooled to the absolute zero. In reality, however, this does not happen. Concomitant heating in the optical molasses prevents the atoms from cooling down below a certain temperature. In this section, we estimate the temperature limit of one dimensional optical molasses at low light intensities.

When momentum is transferred from a photon to an atom or vice versa, not only the

atomic momentum but also ts energy changes. The energy change equals the recoil energy

$$E_{\text{recoil}} = \frac{p_{\text{photon}}^2}{2M} = \frac{\hbar^2 k^2}{2M}, \tag{3.19}$$

where M is the atomic mass. The recoil energy occurs for both absorption and spontaneous emission, hence the atom will gain an energy of $2E_{\text{recoil}}$ in each scattering event. Since the scattering rate from two beams is $2R_{\text{scatt}}$, the overall heating rate becomes $4R_{\text{scatt}}E_{\text{recoil}}$.

From Newton's second law of motion, the cooling rate in optical molasses is expressed as

$$\frac{d}{dt}(\frac{1}{2}Mv^2) = Mv\frac{dv}{dt} = -\alpha v^2 = vF_{\text{molasses}}. \tag{3.20}$$

The cooling rate should be same as the heating rate in steady state. From this condition, we obtain the relation

$$\begin{aligned} vF_{\text{molasses}} &= 4R_{\text{scatt}}E_{\text{recoil}}, \\ 4\hbar k^2 s_0 \frac{2|\delta|/\Gamma}{\left[1 + s_0 + (2\delta/\Gamma)^2\right]^2} v^2 &= 4\frac{\hbar^2 k^2}{2M}\frac{\Gamma}{2}\frac{s_0}{1 + s_0 + (2\delta/\Gamma)^2}. \end{aligned} \tag{3.21}$$

Evaluation of Eq. 3.21 yields the kinetic energy of the atom

$$E_{\text{kinetic}} = \frac{\hbar\Gamma}{8}(\frac{2|\delta|}{\Gamma} + \frac{\Gamma}{2|\delta|}). \tag{3.22}$$

The on-resonance saturation parameter s_0 has been neglected here since we deal with only the low intensity case, $s_0 = I/I_{\text{sat}} \ll 1$. Equation 3.22 has its minimum value of $\hbar\Gamma/4$ at $\delta = \Gamma/2$. We use the equipartition theorem $\frac{1}{2}Mv^2 = \frac{1}{2}k_B T_D$ to derive the temperature corresponding to this kinetic energy,

$$T_D = \frac{\hbar\Gamma}{2k_B}, \tag{3.23}$$

where k_B is the Boltzmann constant. The Doppler cooling limit or Doppler temperature T_D indicates the lowest temperature that can be achieved with optical molasses [Foot, 2005].

For electric-dipole atomic transitions, typical T_D values are sub-millikelvin [Metcalf and van der Straten, 1999]. For example, by inserting the linewidth of ^{84}Kr 5.56 MHz, into Eq. 3.23, we evaluate the Doppler temperature $T_D = 133.4$ μK, which corresponds to the atomic velocity $v = 11.5$ cm/s from the equipartition theorem.

3.3 Zeeman slowing

For decelerating a one dimensional atomic beam, one can simply use a counter propagating light beam. The light frequency should be red-shifted to match the Doppler shift due to the atoms' velocity. This method works well for atoms with a narrow velocity range, but has its limit in that the magnitude of the Doppler effect changes as atoms are slowed. Different light frequencies are required for the different atom velocities. This can be accomplished by sweeping the laser frequency rapidly, which is called the chirp cooling [Prodan and Phillips, 1984]. This method has an obvious disadvantage that slowed atoms arrive in pulses separated by the sweeping period. W. Phillips and H. Metcalf came up with an ingenious way to solve this problem using a spatially varying magnetic field [Phillips and Metcalf, 1982].

In the presence of a magnetic field $\vec{B}$, the Hamiltonian for a free atom is

$$H = H_0 + H_B. \tag{3.24}$$

H_B is a perturbation Hamiltonian from the magnetic field,

$$H_B = -\vec{\mu} \cdot \vec{B}, \tag{3.25}$$

where $\vec{\mu}$ is the magnetic moment of the atom. This perturbation shifts the atomic transition energy by $\Delta E = \mu' B$. In other words, the effective transition frequency changes as $\omega_0 \to \omega_0 + \mu' B/\hbar$. μ' is the effective magnetic moment for the transition, defined as $\mu' \equiv (g_2 M_2 - g_1 M_1)\mu_\mathrm{B}$, where μ_B is the Bohr magneton, $g_{1,2}$ is the Landé g-factor, and $M_{1,2}$ is the magnetic quantum number. The splitting of a spectral line due to the energy shifts by a magnetic field is the Zeeman effect. In this context, let us consider the case of a Zeeman slower with a red-detuned light. Then the term $\mu' B/\hbar$ is required to be negative, which is accomplished by a transition with $\Delta M = -1$.

A varying magnetic field B along the atomic beam axis shifts the transition frequency so that the Zeeman effect compensates for the change of Doppler shift. This apparatus is known as a Zeeman slower. The varying magnetic field is traditionally achieved by a tapered solenoid, and recently an apparatus using permanent magnets was developed [Ovchinnikov, 2008; Reinaudi *et al.*, 2012]. Taking into account the effect of this magnetic

field and the Doppler effect from varying velocities, we obtain a modified scattering force $F_{\mathrm{ZS}}(\omega_l - \omega_0 + kv(z) - \mu' B(z)/\hbar)$. This means that the Zeeman shift by the magnetic field should obey the condition

$$\omega_0 = \omega_l + kv(z) - \frac{\mu' B(z)}{\hbar}. \tag{3.26}$$

Figure 3.4 (top) shows this relation for the atomic energy level, as well as the working principle of a Zeeman slower. Figure 3.4 (bottom) is a schematic of the apparatus.

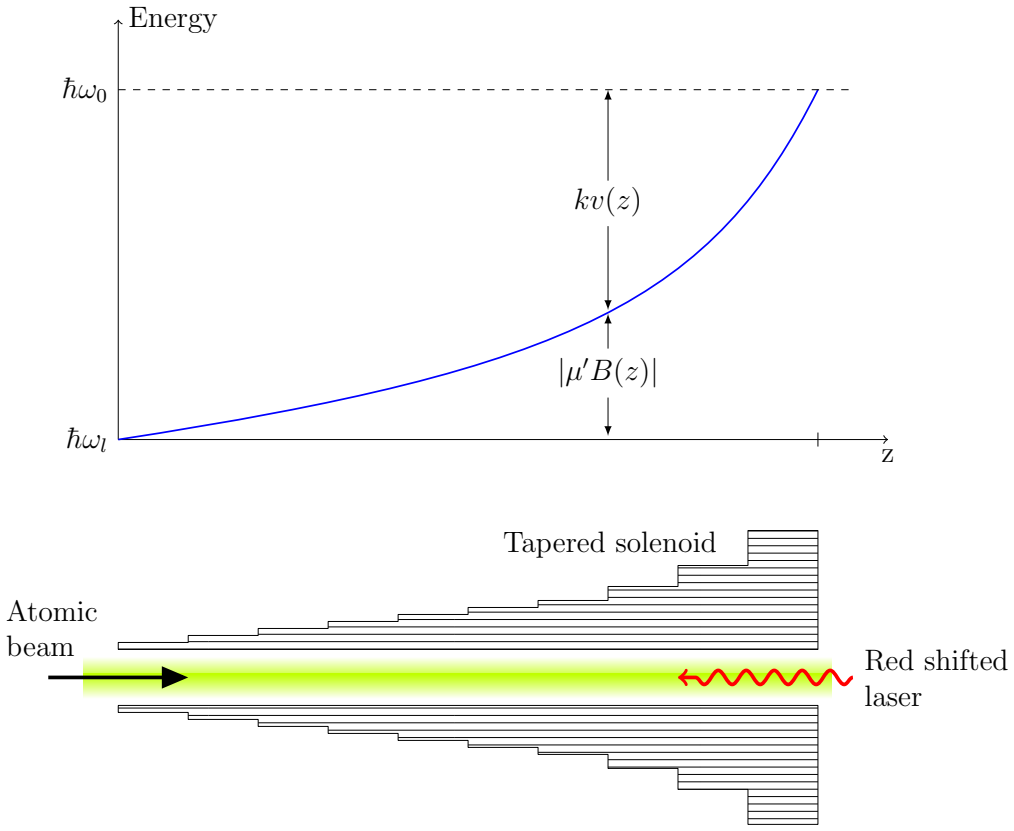

Figure 3.4: Diagram of the energy level in a Zeeman slower (top) and schematic of the apparatus using tapered solenoid to produce the varying magnetic field (bottom). As an atom is decelerated, the Doppler shift decreases and the larger Zeeman effect compensates for this decrease.

From Newtonian mechanics, the velocity at position z satisfies the relation $v_0^2 - v(z)^2 = 2az$, where v_0 is the initial velocity at the entrance of the Zeeman slower. For the constant

deceleration a, the atomic velocity is written as

$$v(z) = v_0 \left(1 - \frac{z}{z_0}\right)^{1/2}, \tag{3.27}$$

where $z_0 = v_0^2/a$ is the length of the Zeeman slower. Any atoms decelerated have the same final velocity v_f at the end of the Zeeman slower, and the Zeeman slower slows down all atoms in the velocity range from v_0 to v_f. By inserting $v(z)$ into Eq. 3.26, we obtain the required magnetic field profile

$$B(z) = B_0 \left(1 - \left(1 - \frac{z}{z_0}\right)^{1/2}\right), \tag{3.28}$$

where $B_0 = \hbar k v_0/\mu'$. Since we aim for the transition with $\Delta M = -1$, with an increasing magnetic field the laser beam should have σ^- polarization.

3.4 Magneto-optical trap

Optical molasses slow down moving atoms, but do not confine them in a small region of space as Eq. 3.16 does not include any position-related terms. A magneto-optical trap (MOT) is the most widely implemented trapping method for neutral atoms [Phillips and Metcalf, 1982]. A one dimensional MOT is achieved by two counter propagating lasers combined with an inhomogeneous magnetic field. The magnetic field should have a zero value at the center and increase away from the center. A pair of anti-Helmholtz coils is usually used to create the magnetic fields for a three dimensional MOT (Fig. 3.5 (left)).

Figure 3.5 (right) shows the MOT mechanism for a $J = 0$ to $J = 1$ transition. The energy levels of atoms with $M_J = 1$ and $M_J = -1$ are split by the Zeeman shift in the presence of magnetic field. The sign of the Zeeman shift depends on the direction of the field; the excited $M_J = 1$ state is shifted up and the $M_J = -1$ state is shifted down for a positive magnetic field ($z > 0$). On the other hand, the $M_J = 1$ state is shifted down and the $M_J = -1$ state is shifted up for a negative magnetic field ($z < 0$). Since the laser is red-shifted, the transition with $\Delta M = -1$ is closer to resonance than the $\Delta M = +1$ transition in the $z > 0$ region. When the incident laser from the right is σ_- polarized, the scattering force that pushes atoms to the left is large in the $z > 0$ region, and small in the

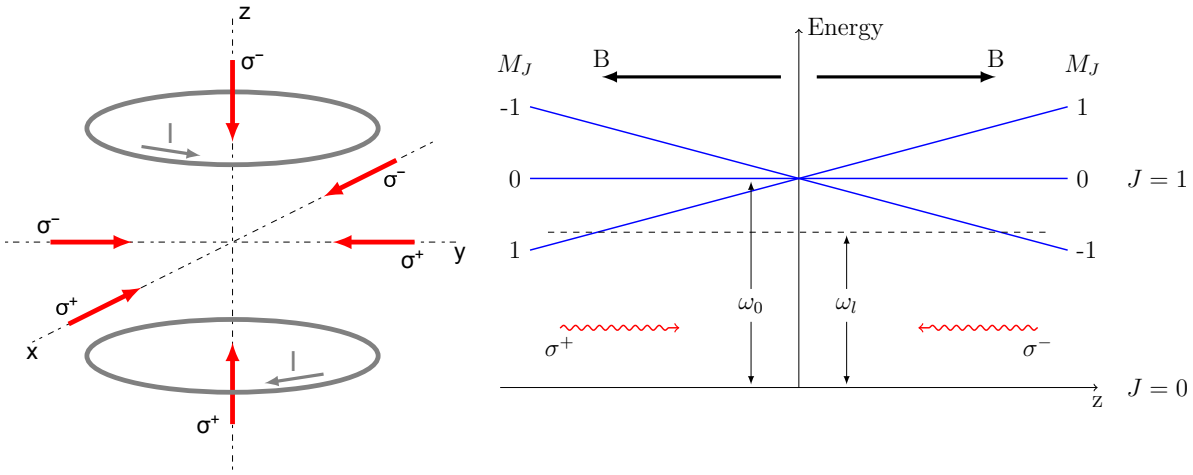

Figure 3.5: Schematic of a three dimensional magneto-optical trap (MOT) (left), and principle of one dimensional MOT (right).

$z < 0$ region. Similarly, the σ_+ polarized laser from the left pushes atoms in the $z < 0$ region more than atoms in the $z > 0$ region. The imbalance of these forces drives atoms to the center of the trap.

The scattering force with the Zeeman effect and the Doppler shift is $F_{\rm ZS}(\omega_l - \omega_0 + kv + \mu' B/\hbar)$, same as for a Zeeman slower. In a one dimensional MOT, the forces from two counter propagating lasers lead to the net force on the atoms;

$$F_{\rm MOT} = F^{\sigma^+}_{\rm scatt}(\omega_l - \omega_0 - kv + \frac{\mu' B}{\hbar}) - F^{\sigma^-}_{\rm scatt}(\omega_l - \omega_0 + kv - \frac{\mu' B}{\hbar}) \tag{3.29}$$

When the magnetic field is a linear function of the position, $B(z) = Az$, this equation becomes

$$\begin{aligned} F_{\rm MOT} &= F^{\sigma^+}_{\rm scatt}(\omega_l - \omega_0 - kv(z) + \frac{\mu'}{\hbar} Az) - F^{\sigma^-}_{\rm scatt}(\omega_l - \omega_0 + kv - \frac{\mu'}{\hbar} Az) \\ &\simeq -2\frac{\partial F}{\partial \omega_l} kv + 2\frac{\partial F}{\partial \omega_0}\frac{\mu'}{\hbar} Az \\ &= -2\frac{\partial F}{\partial \omega_l}(kv + \frac{\mu'}{\hbar} Az) \\ &= -\beta v - \kappa z, \end{aligned} \tag{3.30}$$

where $\beta \equiv 2(\partial F/\partial \omega_l)k$ and $\kappa \equiv \beta \mu' A/k\hbar$. In the third line, we used the relation $\partial F/\partial \omega_l = -\partial F/\partial \omega_0$, since $\delta = \omega_l - \omega_0$. The last line has the form of a harmonic oscillator force, where

β is the viscous damping coefficient, and κ is the spring constant. The first term reduces the atom velocity and the second term confines the atoms in the center of the trap.

Typically, a MOT collects atoms prepared by a Zeeman slower for a high loading rate. The capture velocity of a MOT - the maximum atom velocity that the MOT can trap - can be estimated from the maximum F_{MOT} and the trap laser beam diameter d using the equation $v_0^2 - v_f^2 = 2as$, where s is the displacement:

$$v_c^2 = 2\,\frac{F_{\mathrm{MOT}}}{M}\frac{d}{2}. \tag{3.31}$$

Additionally, we can estimate the temperature of the trapped atoms from the MOT size, using the equipartition theory of a harmonic oscillator:

$$m v_{\mathrm{rms}}^2 = \kappa z_{\mathrm{rms}}^2 = k_B T. \tag{3.32}$$

Chapter 4

Experimental apparatus

The experiment is operated in Pupin Hall, the Physics Department building at Columbia University. For the experiment, we insulated windows in the room with aluminum coated bubble wraps, and covered them with sheets of black paper to block sunlight. An air conditioning system maintains the room temperature at $19 \pm 1°$C for a stable operation of the diode laser.

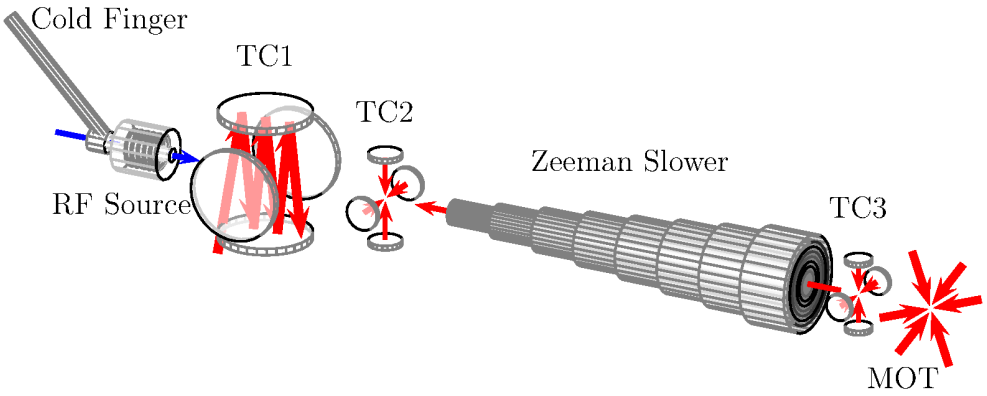

Figure 4.1: Schematic of the atom trap trace analysis (ATTA) system. A radio frequency (RF) discharge source excites atoms to the metastable state while a cold finger cools them. Three transverse cooling stages (TC1, TC2, and TC3) collimate the atomic beam, and a Zeeman slower reduces the longitudinal velocity of the atoms. The decelerated atoms are captured in a magneto-optical trap (MOT) and detected via their fluorescence. The directions of laser beams (red arrows) and the atomic beam (blue arrow) are shown.

Figure 4.1 shows the schematic of our experimental device, known as an atom trap trace analysis (ATTA) system. The main part of the setup is built on an optical table (ThorLabs PTR12108, 6 ft $\times$ 4.1 ft). The picture of the entire system is shown in Fig. 4.2. The design and construction of each component is explained in this chapter.

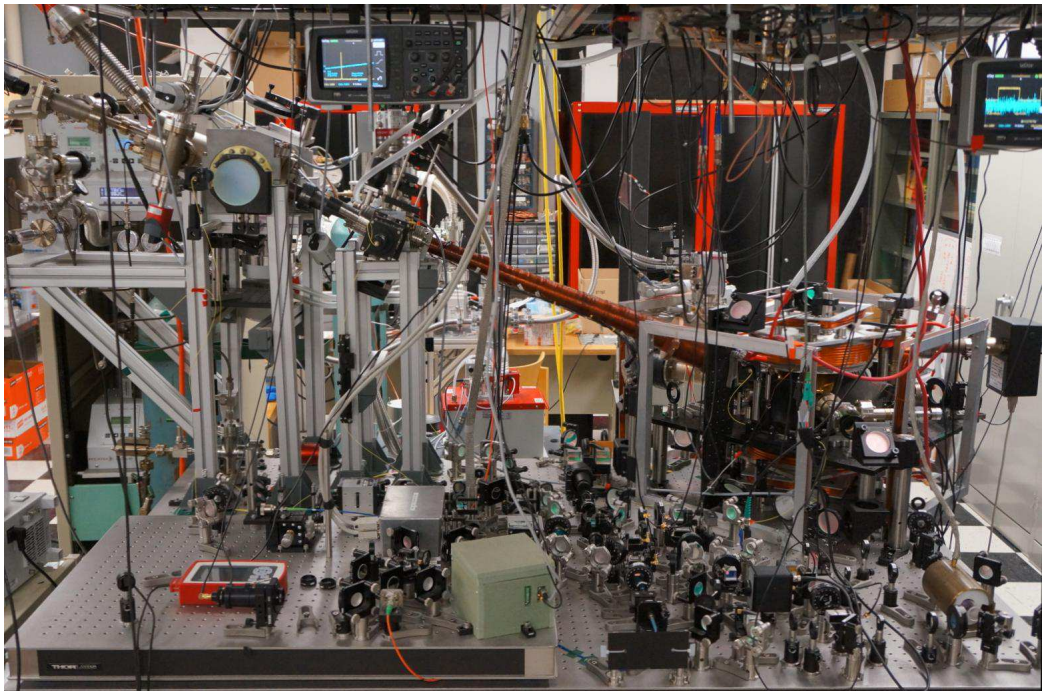

Figure 4.2: Photo of the atom trap trace analysis (ATTA) system at Columbia University. The axis of the system has a slope of 20.5° from the horizontal surface to fit the table space.

4.1 Laser system

One diode laser provides all the required light for trapping and detecting krypton and argon atoms. We employ a custom-built external cavity diode laser (ECDL) in the Littman-Metcalf configuration (Fig. 4.3 (left)), which contains a diffraction grating and an adjustable mirror [Liu and Littman, 1981]. This configuration has an advantage that the direction of the output beam is fixed, compared to the Littrow configuration which uses only a grating. An anti-reflection coated diode (Sacher SAL-0840-060) contained in the external cavity

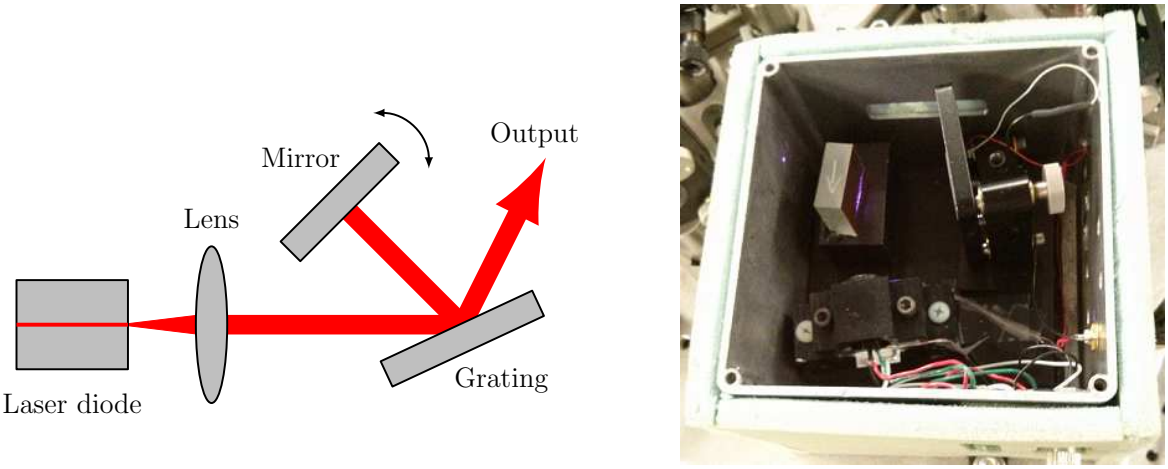

Figure 4.3: Schematic of a Littman-Metcalf external cavity diode laser (ECDL) (left). A diffraction grating sends the first-order beam to a mirror, which mirror reflects the beam into the laser diode. The output frequency can be tuned by adjusting the mirror angle. Photo of the ECDL (right). Diffracted laser light is shown on the grating in purple.

produces a laser of 50 mW with a linewidth < 1 MHz.

A kinematic mirror mount is used to control the angle of the mirror, consequently tuning the wavelength of the laser. We can switch the wavelength between the ^{40}Ar transition at 811.7542 nm and the ^{84}Kr transition at 811.5132 nm by controlling the knobs of the mirror mount and slightly adjusting the driving current of the laser diode. Additionally, a piezoelectric transducer (PZT) was inserted into one axis of the mount for manual fine tuning and laser locking. Since the diode behavior is sensitive to temperature, we use two temperature controllers inside the box to keep the temperature constant; one is near the diode, and the other is at the bottom of the anodized aluminum plate base. The entire box is enclosed by a styrofoam shield to buffer against external temperature changes (Fig. 4.3 (right)).

The 50 mW output of the ECDL is split: 80% of the light is used to seed a tapered amplifier and the rest is divided between a Fabry-Perot spectrum analyzer (ThorLabs SA210-7A) and a wavelength meter (Bristol 621) which are used to monitor the wavelength of the laser. With the 40 mW seed light, the tapered amplifier (Eagleyard EYP-TPL-0808-01000)

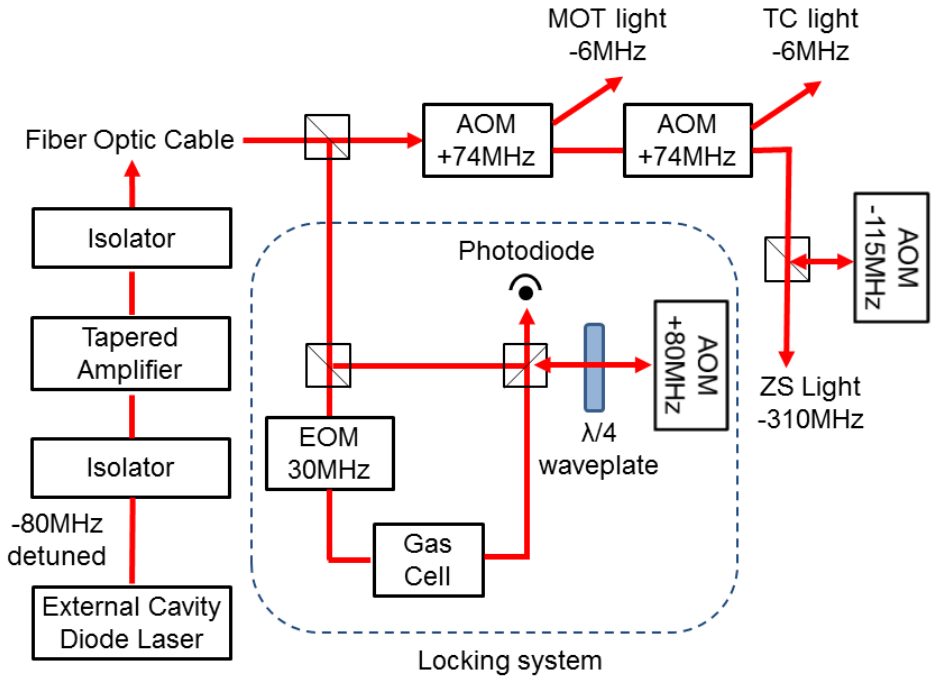

Figure 4.4: Schematic of the laser system.

produces 1.1 W of light that follows the characteristics of the seed light. Two isolators (Conoptics 700) after the ECDL and the tapered amplifier prevent any reflected laser from going backward into the diode. After the beam is properly shaped with lenses, the light is sent through a single-mode polarization maintaining (PM) fiber. This is done to selectively transfer the lowest-order laser mode and decouple any alignment drifts before the fiber from the rest of the experiment. These optical components are set up on a damped optical breadboard to isolate them from any vibrations of the table. The fiber ultimately provides an output of around 550 mW to the cooling and trapping parts of the experiment.

After the fiber, 20 mW of the laser is split off and sent to a laser locking setup. The light beams for transverse cooling, longitudinal slowing, trapping, and detecting atoms have different powers and detunings from the atomic resonance, as detailed in Tab. 4.1. In order to set the required detunings, the light from the PM fiber is passed through three acousto-optic modulators (AOM). Each AOM acts as a transmission grating: the zeroth order beam has zero frequency shift and the higher order beams have frequency shifts that depend on

their diffraction order, the drive frequency of the AOM, and the direction of the sound wave across the AOM. The first AOM is set at 74 MHz and the first order diffracted beam of 300 mW is used for the MOT beams. The second AOM is also set at 74 MHz with its first-order diffracted beam providing 60 mW for the three transverse cooling stages. The last AOM is set at 115 MHz and the negative first-order diffracted beam is double-passed through the AOM to provide 20 mW of light for the Zeeman slower. Since transitions of both argon and krypton have no hyperfine structure, no optical repumping is required in this experiment.

We lock the diode laser in a narrow bandwidth by means of Doppler-free saturated absorption spectroscopy [Bjorklund and Levenson, 1981; Hall, 1981]. The laser in the locking system is split into a weak probe beam and a strong pump beam. The probe beam is phase-modulated by a 30 MHz electro-optical modulator (EOM). The probe beam double-passes an AOM which is set at 80 MHz, thus the negative first order diffracted beam is shifted by -160 MHz. The probe beam, which passes an argon or krypton gas cell, is detected by a photodiode, and the signal is processed by a lock-in amplifier (Stanford Research SR810 DSP). A helical coil, driven by a radio frequency (RF) signal at a 60∼70 MHz frequency and a ∼1 W power, produces discharge in the argon or krypton gas cell. The lock-in amplifier provides an error signal for the piezo driver controlling the mirror in the ECDL. The laser is locked at -80 MHz from the resonant frequency of the reference atom. Figure 4.4 describes the design of the laser system.

Table 4.1: Beam properties for each stage of the experiment.

Destination	Detuning [MHz]	Power [mW]
Locking system	-80	20
Magneto-optical Trap	-6	300
Transverse cooling	-6	60
Zeeman slower	-310	20

4.2 Vacuum system

The system is maintained at ultra-high vacuum to prevent the metastable atoms from scattering off background atoms. The vacuum system is composed of the following components: a sample reservoir, a source chamber, three transverse cooling chambers, and a magneto-optical trap chamber. Each stage is differentially pumped down so that the source chamber has a higher pressure and the MOT chamber has a relatively low pressure. A schematic of the vacuum system in shown in Fig. 4.5.

Argon, xenon, and krypton bottles are connected to the reservoir via regulators. The reservoir is pumped down by a turbopump system (Pfeiffer Vacuum TSU 071 E, pumping speed 59 l/s for nitrogen) including a dry diaphragm pump when the system is not in operation. A valve to the pump is closed when the reservoir is filled with gas for operation. We fine-control the gas flow from the reservoir to the system using a stainless steel ultra-fine leak valve (Lesker VZLVM267) installed between the reservoir and the source chamber. The source chamber is connected to the first TC chamber via a custom made copper gasket with a 0.25" hole for the purpose of differential pumping. A turbopump (Pfeiffer Vacuum TMU 262 P, pumping speed 210 l/s for nitrogen) pumps down the first transverse cooling chamber and the source chamber. The first and second transverse cooling chambers are separated by a gate valve, which is open only when the system is running. A turbopump (Pfeiffer Vacuum HiPace 80, pumping speed 67 l/s for nitrogen) is used to pump down the second transverse cooling chamber. A differential pumping tube with a radius 0.32 cm connects the second transverse cooling chamber and the Zeeman slower. Another turbopump (Pfeiffer Vacuum TMU 262 P) is used to maintain vacuum in the MOT chamber. These three turbopumps are backed by a main pump station which has a turbopump and a diaphragm pump. Pneumatic valves are on the outputs of the three turbopumps so that we can break the vacuum to the backing pump station while maintaining vacuum in the system. A failsafe circuit was built to close the valves automatically in the case of a power failure.

To monitor the pressure, we use combined Pirani/cold-cathode gauges (PIG) (Pfeiffer Vacuum PKR 251, PKR 261, and KIR 270) at each stage. Additionally, a pressure transducer (Stellar Technology GT1600-25A0331) with a quoted accuracy of 0.1% is used to detect a high pressure in the reservoir, and a capacitive manometer (Pfeiffer Vacuum CMR

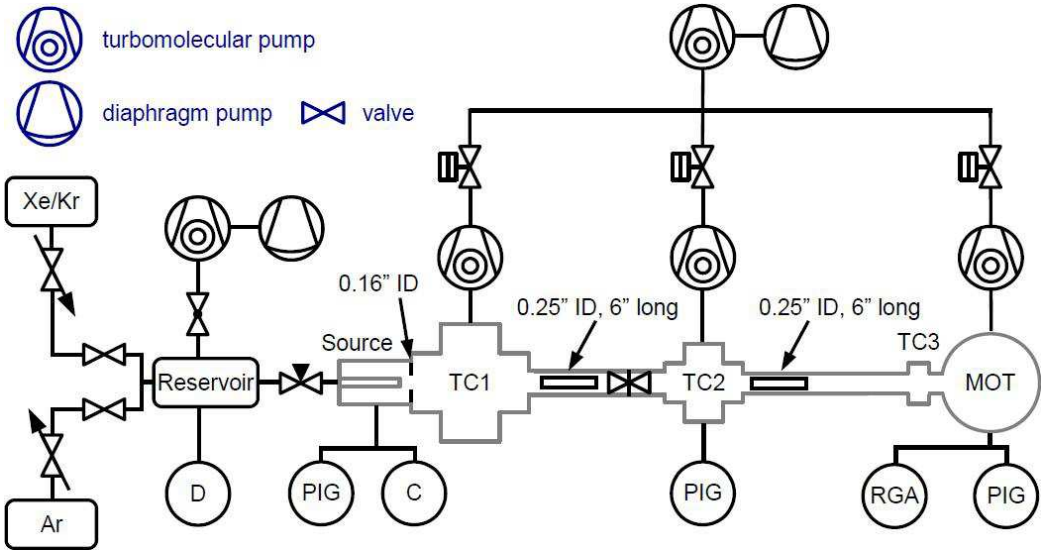

Figure 4.5: Schematic of the vacuum system. The vacuum is monitored by a pressure transducer (D), capacitive manometer (C), combined Pirani/cold cathode gauges (PIG), and a residual gas analyzer (RGA)

365) with a quoted accuracy of 0.5% was attached in the source chamber for the precise pressure measurement, which is necessary to keep the consumption rate constant. A residual gas analyzer (RGA) (Extorr Inc. XT200) also monitors the pressure in the MOT chamber via mass spectrometry. When the system is not in operation, the vacuum is maintained at $\sim 10^{-7}$ torr in the source chamber, low 10^{-8} torr in the second transverse cooling chamber, and low 10^{-9} torr in the MOT chamber. The gas flow is monitored and controlled via the pressure in the source chamber, which is usually in the range of $0.01 \sim 0.1$ mtorr.

4.3 RF discharge source

4.3.1 Possible excitation methods

Because of the absence of lasers with sufficiently short wavelengths resonant with transitions from the ground state of krypton, we use a transition from the metastable state $5s[3/2]_2$ ($^3P_2$) to $5p[5/2]_3$ ($^3D_3$) for trapping and detecting. For this purpose, we first need to excite ground state atoms to the metastable state, with the energy of 9.9 eV above the

ground state. Figure 4.6 shows three possible ways to generate metastable state atoms. In Fig. 4.6 (left), plasma discharge brings the ground state atoms to the metastable state via inelastic collisions with ions and electrons. Collision of the excited krypton atoms with xenon atoms can lead to de-excitation of the metastable krypton and excitation of the Xe: Kr* + Xe → Kr + Xe*, where * indicates a metastable state. This results in a decrease of the excitation efficiency, and consequently a decrease of the MOT loading efficiency. The fraction of atoms excited via discharge is known as $10^{-4} \sim 10^{-3}$ [Chen *et al.*, 1999; McKinsey and Orzel, 2005].

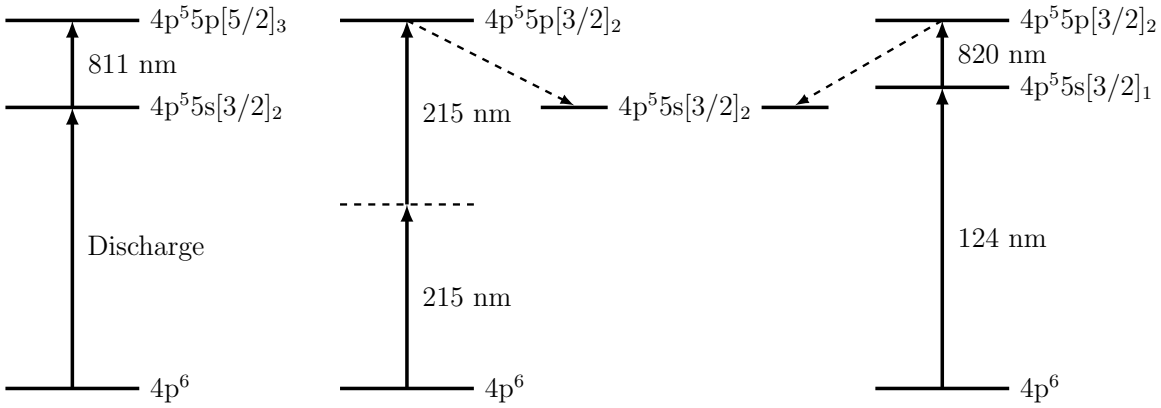

Figure 4.6: Excitation schemes for ^{84}Kr atom. Populating the metastable level via RF discharge (left), via a non-resonant UV+UV excitation (middle), and via a resonant VUV+IR excitation (right).

Figure 4.6 (middle) describes two-photon non-resonant optical excitation where ground state atoms absorb two 215 nm photons and jump to the $^3P_2$ ($5p[3/2]_2$) state. These excited atoms decay to the metastable state with a 77% probability. A high intensity pulsed laser would be required for this purpose since the excitation rate is proportional to the square of the laser intensity. The expected metastable fraction with a commercially available pulsed dye laser is on order of 10^{-2} [McKinsey and Orzel, 2005]. The problem of collisions with xenon still remains in this method, but collisions with high-energy ions and electrons can be eliminated, thus leading to a higher fraction of metastable atoms.

The third possibility uses a two-photon resonant optical excitation as in Fig. 4.6 (right).

A 124 nm laser excites ground state atoms to the $5s[3/2]_1$ state, then a 820 nm laser is used to bring up these atoms to the $5p[3/2]_2$ state. Atoms in this state decay to the metastable state with a 77% probability as discussed in the previous paragraph. While the resonant interaction in this scheme allows a high efficiency (on order of $\sim 10^{-2}$) [Young *et al.*, 2002], this system requires two additional wavelengths and increases complexity.

4.3.2 RF discharge resonator

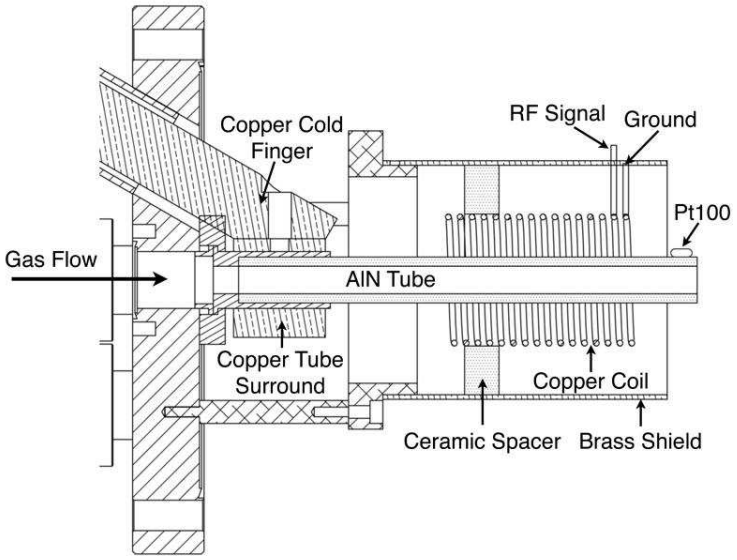

Figure 4.7: Cross section of the RF discharge source. The gas expands through an AlN tube which is cooled by a cold finger. A plasma is generated by an RF signal applied to the copper coil, producing metastable atoms. Temperature is monitored by a Pt100 platinum resistive temperature sensor.

In this experiment, we use the discharge method to produce metastable atoms. A helical resonator creates discharge, where the design parameters are based on Refs. [Macalpine and Schildknecht, 1959; Chen *et al.*, 2001]. The schematic is shown in Fig. 4.7. The resonator consists of a helical coil and a brass shield; 18 American wire gauge (AWG) bare copper wire was used in making the coil. The coil has a length of 7.6 cm and an inner diameter of 3.4 cm, containing 16 windings. One end of the coil is connected to the shield, which is 11.1 cm long with an inner diameter of 6.34 cm, and the other end is connected to the RF

power wire. A Macor ceramic spacer supports the coil, and prevents it from sagging due to gravity.

During operation, the source is cooled by a pulse tube refrigerator (Iwatani PDC08) to reduce the atomic velocity, which results in a higher capture fraction by the Zeeman slower. The atoms flow through an aluminium nitride (AlN) tube inside the resonator coil. The thermally conductive and electrically insulating property of AlN allows efficient cooling without an effect on plasma discharge. A platinum resistive thermometer Pt100 reads the temperature at the end of the tube. There is a viewport on the back side of the source for observing the discharge status. Figure 4.8 shows the picture of the assembled source.

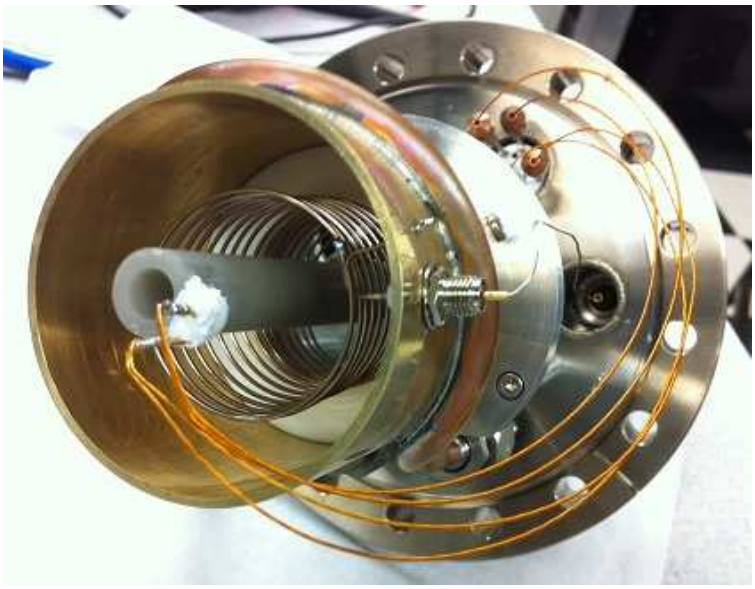

Figure 4.8: Image of the helical coil RF resonator.

A voltage controlled oscillator generates the RF signal to the resonator. A small amount of this power is split off and used for signal monitoring by a spectrum analyzer (Hameg Instruments HMS1000), and the main part of the signal is amplified by an RF amplifier (Mini-Circuits ZHL-50W-52-S). A SubMiniature version A (SMA) cable transfers the output signal of the amplifier into the source. The impedances of the amplifier and the source needs to be matched carefully for the best performance of the source [Sukenik and Busch, 2002].

When switching on the plasma source, we increase the RF power until the source lights, then reduce the power to find the best system efficiency, as the source has a hysteresis property. As long as the efficiency remains stable, the minimal power is preferred to reduce heating, subsequently reducing the atomic velocity. The performance of the source depends on many parameters: frequency and power of the RF signal, source pressure, and temperature inside the chamber. We empirically find the optimal parameters maximizing the excitation efficiency, which is monitored via the MOT intensity. The typical operating parameters are ∼15 W of applied RF power at ∼115 MHz, at a pressure of ∼0.1 mtorr and temperature of ∼160 K. The discharge colors of argon gas and xenon gas are shown in Fig. 4.9.

Figure 4.9: Glowing plasma discharge of argon gas (left) and xenon gas (right) by a helical coil resonator.

4.4 Transverse cooling of the atomic beam

Three transverse cooling stages in the ATTA system collimate the atomic beam using optical molasses with 6 MHz red detuned lasers. These stages significantly enhance the loading rate of the MOT.

The first transverse cooling chamber has four windows of a 9.5 cm diameter in 6" flanges. Since the argon beam has the most probable velocity of ∼300 m/s, and the krypton beam ∼200 m/s at the operating temperature, the atoms pass the interaction region quickly. The longer the interaction between atom and light, the higher the collimation efficiency. Therefore we extend the interaction region by reflecting the laser multiple times between two flat mirrors as Fig. 4.10 (left) shows. This allows the longer interaction times, ans has an advantage of a high laser intensity compared to expanding the beam size with fewer reflections. The laser beam is slightly focused to compensate for the decrease of laser power due to absorption by atoms and losses at window surfaces. The interaction time with the laser is 3×10^{-4} s for the argon beam, and 5×10^{-4} s for the krypton beam. This will allow each argon atom to experience $\sim 2 \times 10^3$ scatters, and krypton atom $\sim 3 \times 10^3$ scatters at the laser intensity of a few I_{sat}.

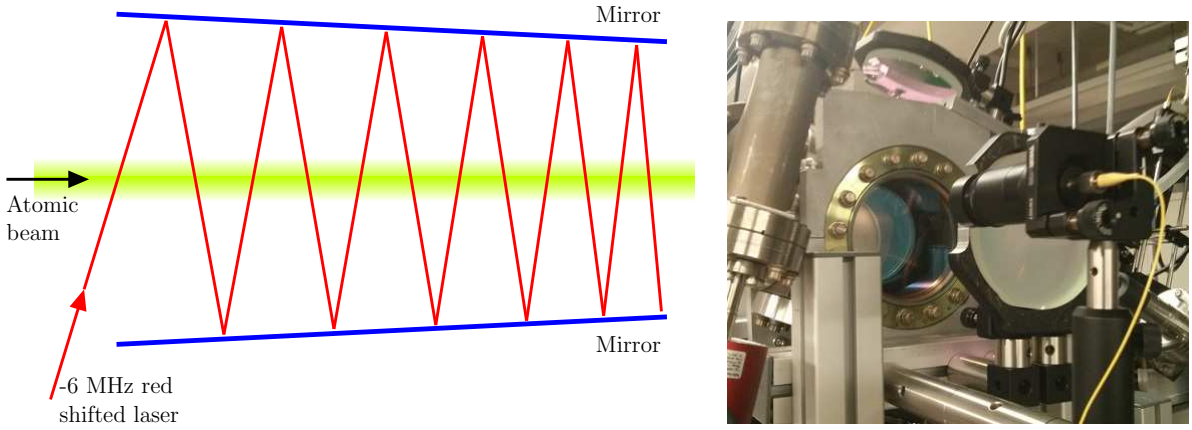

Figure 4.10: Schematic (left) and photo (right) of the first transverse cooling setup. The −6 MHz detuned laser is reflected multiple times between two mirrors and sets up optical molasses.

Figure 4.10 (right) shows the setup of the first transverse cooling stage. Two fiber optic cables deliver the light to the vertical and horizontal axes. Each light beam is expanded to a 1 cm diameter by a telescope, and has an intensity of ∼5 mW/cm^2. This intensity balances the efficiency and the amount of laser power used. The efficiency of the first transverse

cooling is shown in Fig. 4.11 as a function of the laser intensity. We adjust the laser beam paths with the mirrors and fiber optic mounts to optimize the transverse cooling efficiency, which is monitored via the MOT intensity.

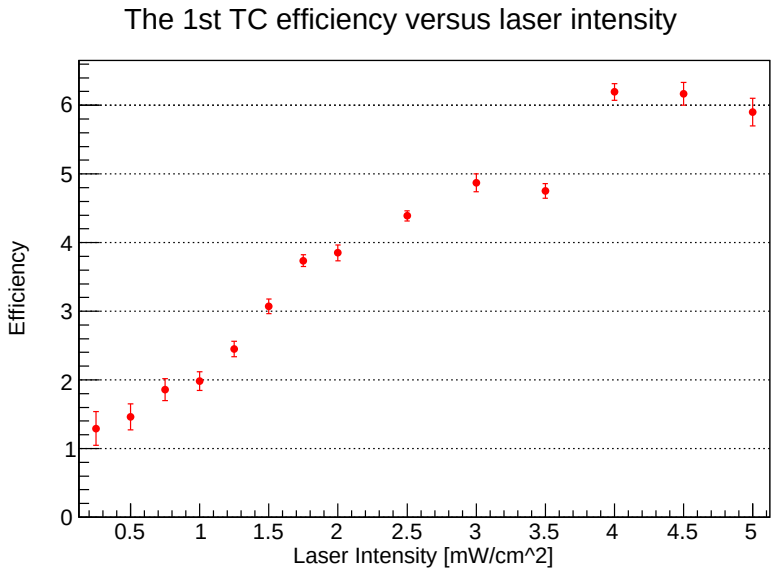

Figure 4.11: First-stage transverse cooling efficiency as a function of the laser intensity, measured with the horizontal beam only.

The atomic beam leaving the first transverse cooling chamber is further collimated by the second transverse cooling stage. The output laser is first expanded to a 0.5 cm diameter by a telescope, then extended along one axis by two convex cylindrical lenses, for a final size of 0.5 cm $\times$ 3 cm and an intensity of 3 mW/cm^2. The chamber has windows in 2.75" flanges allowing the laser beam to pass through. A mirror on the other side of vacuum cross reflects the laser perpendicularly so that the two beams counterpropagate. At first, this stage was designed for a bow-tie configuration with only one laser beam, but later changed to a retro-reflecting configuration with two beams due to difficulty in aligning.

The third transverse cooling stage was installed following the Zeeman slower since scattering inside the slower makes the atomic beam disperse before reaching the MOT chamber. As the longitudinal velocity of the atomic beam is reduced by the Zeeman slower, sufficient

interaction time can be achieved with a small size beam. Thus a 1.33" cube is used for the third transverse cooling chamber. The output light from a fiber optic cable is expanded to a 1 cm diameter at a 3 mW/cm^2 intensity. Since the atoms are slowed to the final velocity of 30 m/s, the atoms experience an interaction time with the light of 3×10^{-4} s, which is similar to the case of the first transverse cooling.

4.5 Zeeman atom slower

4.5.1 Design

In the Zeeman slower, a spatially tuned magnetic field B along the atomic beam keeps a red-detuned slowing laser beam always near resonance. In this subsection, we find the optimal Zeeman slower design.

Deceleration from the light pressure force in a Zeeman slower is expressed as

$$a(v,z) = \frac{F(v,z)}{m} = -\frac{\hbar k \Gamma}{2m} \frac{s_0(z)}{1 + s_0(z) + \left(\dfrac{\delta + kv(z) - \mu' B(z)/\hbar}{\Gamma/2} \right)^2}. \tag{4.1}$$

In the denominator, the relation of Eq. 3.26 was used. As introduced in Sec. 3.3, μ' is the effective magnetic moment of the transition, $\mu' = \mu_B(M_J^e\ g_J^e - M_J^g\ g_J^g)$, where g and e refer to ground and excited states [Metcalf and van der Straten, 1999]. The Landé g-factor is given by

$$g_J = 1 + \frac{J(J+1) + S(S+1) - L(L+1)}{2J(J+1)}, \tag{4.2}$$

such that $g_J(^3\mathrm{P}_2) = 3/2$ and $g_J(^3\mathrm{D}_3) = 4/3$.

Possible transitions between $^3\mathrm{P}_2$ and $^3\mathrm{D}_3$ are described in Fig. 4.12 with energy levels shifted by the Zeeman effect. The strength of a transition is given by the square of the transition dipole moment,

$$\begin{aligned} \mu_{eg} = e(-1)^{L_e+S-M_J^e} \sqrt{(2J_g+1)(2J_e+1)} \\ \times \begin{Bmatrix} L_e & J_e & S_g \\ J_g & L_g & 1 \end{Bmatrix} \begin{pmatrix} J_g & 1 & J_e \\ M_J^g & q & -M_J^e \end{pmatrix} \langle \alpha_e L_e \,||r||\, \alpha_g L_g \rangle , \end{aligned} \tag{4.3}$$

where q is the light polarization, and α represents all properties of the state besides its orbital angular momentum. When it comes to the transition of our interest, $^3\mathrm{P}_2$ - $^3\mathrm{D}_3$, all terms

except for the $3j$ symbol are fixed. Thus, the strength of each transition is proportional to the square of the $3j$ symbol. The relative transition strengths are also shown in Fig. 4.12.

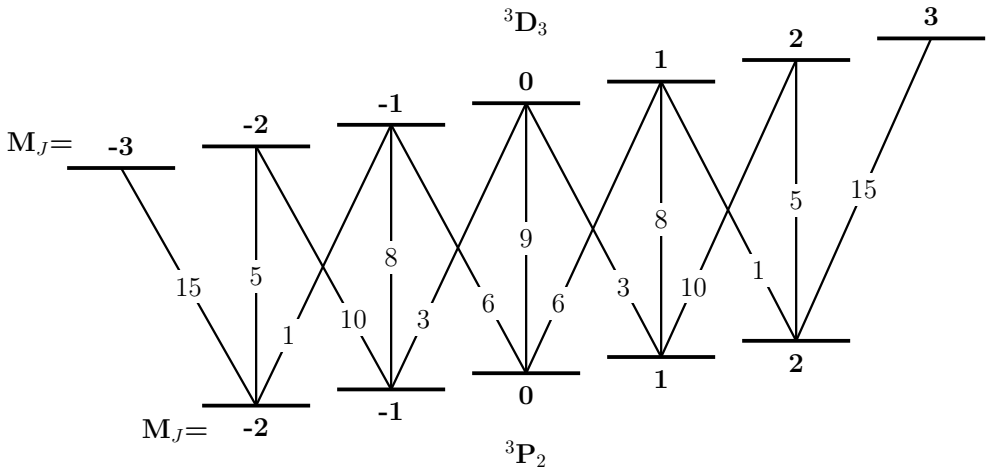

Figure 4.12: Relevant energy levels when external field B is applied, and relative transition strengths for ^{3}P$_2$ and ^{3}D$_3$ states.

We encounter a problem that the sublevel transitions have different magnetic moments μ', e.g., $\mu' = -(4/3)\mu_B$ for $M_J^g = 0 \ \rightarrow M_J^e = -1$, and $\mu' = -(7/6)\mu_B$ for $M_J^g = -1 \ \rightarrow M_J^e = -2$. The maximum difference in μ' values is less than $1\times\mu_B$ in our case, corresponding to the Doppler effect from a frequency detuning $\delta < 20\Gamma$ at the typical fields B, $\sim$100 G. Under this condition, we can still expect a certain amount of light-atom interaction at a light intensity of a few $I_{\rm sat}$ (Fig. 3.1). Note that the B field is much smaller than 100 G at the Zeeman slower entrance. Furthermore, atoms will be optically pumped to the left side in Fig. 4.12 in a short time by σ^- light, and transitions will take place only between the $M_J^g = -2$ and the $M_J^e = -3$. For this reason, we optimize the Zeeman slower for the $M_J^g = -2$ to $M_J^e = -3$ transition.

Now we have $\mu' = \mu_B((-3)(4/3) - (-2)(3/2)) = -\mu_B$. The deceleration has its maximum value

$$a_{\rm max} = -\frac{\hbar k\Gamma}{2m}\frac{s_0(z)}{1+s_0(z)} \tag{4.4}$$

for $v(z) = v_{\rm res}(z) \equiv (\mu' B(z)/\hbar - \delta)/k$. A Zeeman slower is usually not designed for $a_{\rm max}$,

since any imperfections will result in atoms that are too fast to decelerate. Instead, we design for $a(z) = \epsilon a_{\max}(z)$, with $0 < \epsilon < 1$. By inserting $a(z) = \epsilon a_{\max}(z)$ into Eq. 4.1, we derive the velocity trajectory

$$v_\epsilon(z) = v_{\rm res}(z) - \frac{\Gamma}{2k}\sqrt{[1 + s_0(z)]\frac{1-\epsilon}{\epsilon}}. \tag{4.5}$$

Now we need the optimal value of s_0 and ϵ. The damping coefficient of the scattering force $\alpha \equiv -\partial F(v)/\partial v \propto s_0/(1+s_0)^2$ is maximized at $s_0 = 1$. The strength of the deceleration force $F(v) \propto s_0/(1+s_0)$ monotonically increases $0 \to 1$ with increasing s_0, and reaches half-strength at $s_0 = 1$. The product $F(v) \times \partial F(v)/\partial v$ is maximized at $s_0 = 2$. The cooling is proportional to $\partial F(v)/\partial v$, and the best cooling is achieved if $\partial^2 F(v)/\partial v^2 = 0$. This condition is satisfied when $\epsilon = 2s_0/(1+s_0)$. When $s_0 = 2$, $\epsilon = 0.75$. To account for experimental imperfections of the Zeeman slower, we design the Zeeman slower for $\epsilon = 0.65$.

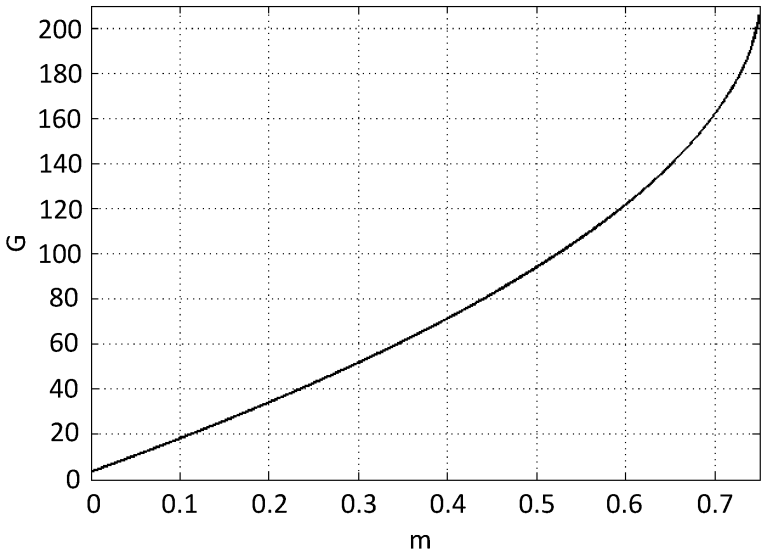

Figure 4.13: Design field for the Zeeman slower with a 310 MHz red detuned laser.

The final velocity is set to $v_f = 15$ m/s, which should be well within the capture range of the krypton and argon MOTs. An atom is then accelerated toward the Zeeman slower entrance such that the backward velocity evolves as

$$\frac{dv_{\rm b}(z')}{dz'} = \frac{a_{\rm b}(z')}{v(z')}, \tag{4.6}$$

where the backward acceleration $a_{\rm b} = \epsilon|a_{\rm max}({\rm Kr})|$ and z' is the backward coordinate along the Zeeman slower. The Kr parameters are used in the expression for $a_{\rm b}(z')$ because the efficiency is most crucial for krypton. Inverting the coordinate $z' \to z$ we obtain a velocity trajectory, $V(z)$. The design magnetic field $B(z)$ is then

$$\begin{aligned} B(z) &= \frac{\hbar[\delta_0 + k v_{\rm res}(z)]}{\mu} \\ &= \frac{\hbar}{\mu}\left(\delta_0 + kV(z) + \frac{\Gamma}{2}\sqrt{[1+s_0(z)]\frac{1-\epsilon}{\epsilon}}\right). \end{aligned} \tag{4.7}$$

As shown in Fig. 4.13, the choice of $\delta_0 = -310$ MHz corresponds to all positive values of B inside the Zeeman slower.

Finally, the $v(z)$ trajectories for either krypton or argon are calculated starting from the initial velocity v_0, and applying the deceleration

$$a(z) = -\frac{0.65}{0.75}\,\frac{\hbar k\Gamma}{2m}\frac{s_0(z)}{1 + s_0(z) + \left(\dfrac{\delta_0 + kv(z) - \mu B(z)/\hbar}{\Gamma/2}\right)^2}, \tag{4.8}$$

where the prefactor of $0.65/0.75 \approx 0.87$ allows for the experimental imperfections of $B(z)$. The Zeeman slower length $l_{ZS} = 75$ cm is constrained by the table size, and the above assumptions lead to the Zeeman slower capture velocities $v_c({\rm Kr}) \approx 245$ m/s, $v_c({\rm Ar}) \approx 250$ m/s. The velocity trajectories for argon and krypton beams are plotted in Fig. 4.14.

Based on the geometry of the vacuum system, the MOT is 15 cm from the optical window for the Zeeman slower light, and a 75 cm Zeeman slower region begins another 25 cm further. Over this 1.15 m span, we focus the light so that it decreases from a $\sim$1.2 cm diameter at the window to a $\sim$0.6 cm diameter at the Zeeman slower differential pumping tube exit. This provides a small amount of transverse cooling, and compensates for the light power decrease through absorption. Roughly, this gives a $\sim$1 cm diameter light beam at the Zeeman slower exit. Given $s_0 = 1.5$ and $I_{\rm sat} = 1.4$ mW/cm^2, the Zeeman slower requires an optical power of only $\sim$2 mW. A telescope with one concave lens and one convex lens is carefully aligned so that the light beam is expanded to an appropriate diameter (> 1.2 cm) and focused gently as designed above.

For a temperature T (in Kelvin), the thermal velocity for each species is $\tilde{v} \equiv \sqrt{k_B T/m}$. The fraction of the atoms with a velocity v below the Zeeman slower capture velocity v_c is

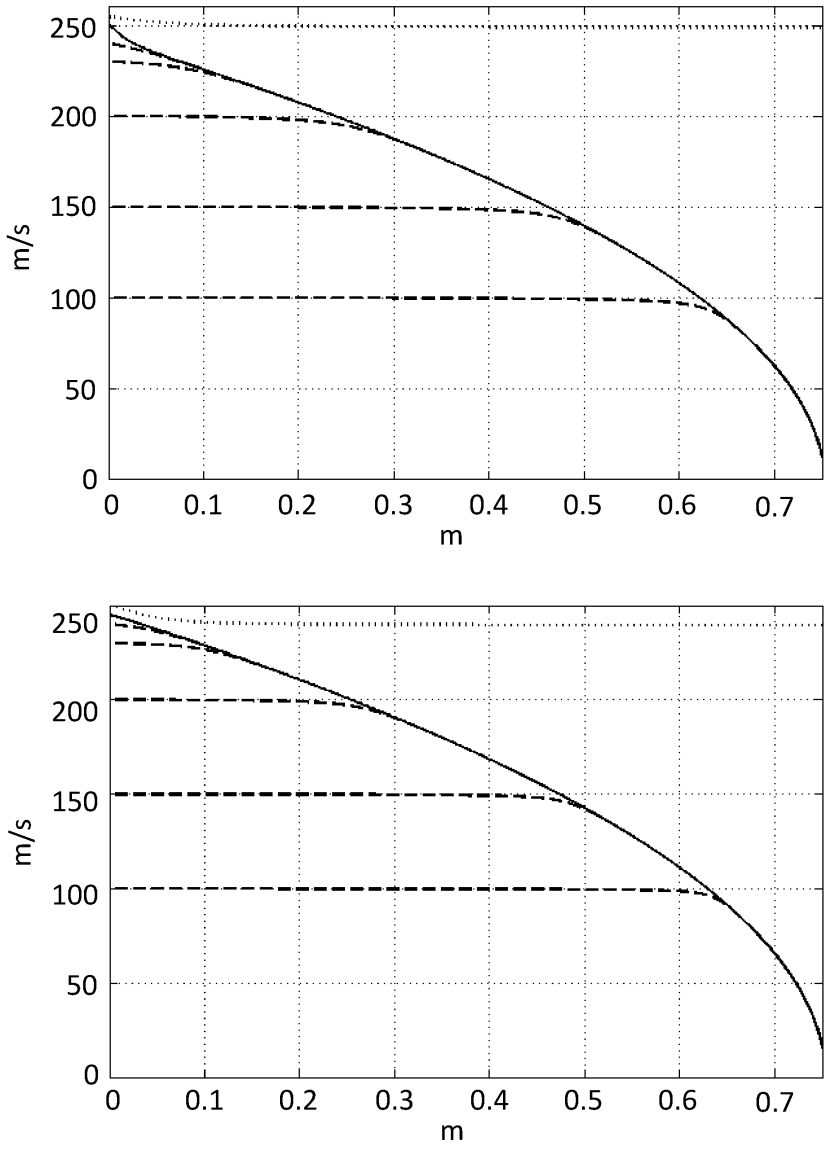

Figure 4.14: Velocity trajectories of argon (top) and krypton (bottom) in the Zeeman slower.

evaluated as

$$f_c = \int_0^{v_c} \frac{v^3}{2\tilde{v}^4} \exp(-v^2/(2\tilde{v}^2))dv, \tag{4.9}$$

based on the Maxwell-Boltzmann distribution for a thermal beam, where $\tilde{v} \equiv \sqrt{k_B T/m}$. For our Zeeman slower parameters, we obtain $f_c(\mathrm{Kr}) = 66\%$ and $f_c(\mathrm{Ar}) = 29\%$ at $T = 140$ K, and $f_c(\mathrm{Kr}) = 29\%$ and $f_c(\mathrm{Ar}) = 9\%$ at $T = 300$ K.

The greater the deceleration of an atom, and hence the number of scattered photons N, the greater the transverse divergence of the slow atomic beam due to the random photon scattering events. For an atom whose longitudinal velocity changes by $\Delta v(z)$ between the Zeeman slower entrance and position z, the atom's root mean square (rms) transverse deviation at $z(t)$ (assuming zero initial beam divergence) is determined as follows:

$$\begin{aligned} x_{\mathrm{rms}}^2 = \langle x^2(t)\rangle &= N\langle \delta v_x^2\rangle\langle (t-\tau)^2\rangle \\ &= \frac{v_r^2}{3} N \int_0^t (t-\tau)^2 d\tau \frac{1}{t} \\ &= \frac{v_r^2}{3} N \frac{t^2}{3} \end{aligned} \tag{4.10}$$

and

$$N = \frac{\Delta v(z)}{v_r}, \tag{4.11}$$

where t is the time the atom has spent in the Zeeman slower, δv_x is the transverse velocity change at each scattering event, τ is the variable denoting the occurrence time of a scattering event, and the recoil velocity $v_r \equiv \hbar k/m$. Therefore,

$$x_{\mathrm{rms}} = \sqrt{\langle x^2(t)\rangle} = \frac{t(z)}{3}\sqrt{v_r \Delta v(z)}. \tag{4.12}$$

The time t is parametrized by the position coordinate

$$t(z) = \int \frac{dz}{v(z)}, \tag{4.13}$$

and the total time in the Zeeman slower for v_c is estimated to be ∼6 ms for both species. Assuming a 6 mm diameter atomic beam at the start of the Zeeman slower (which is also consistent with the size of the last differential pumping tube), the maximum atomic beam diameter at the Zeeman slower exit is 10 mm for krypton and 13 mm for argon, assuming zero initial beam divergence. Figure 4.15 shows the transverse divergence profile inside the

Zeeman slower.

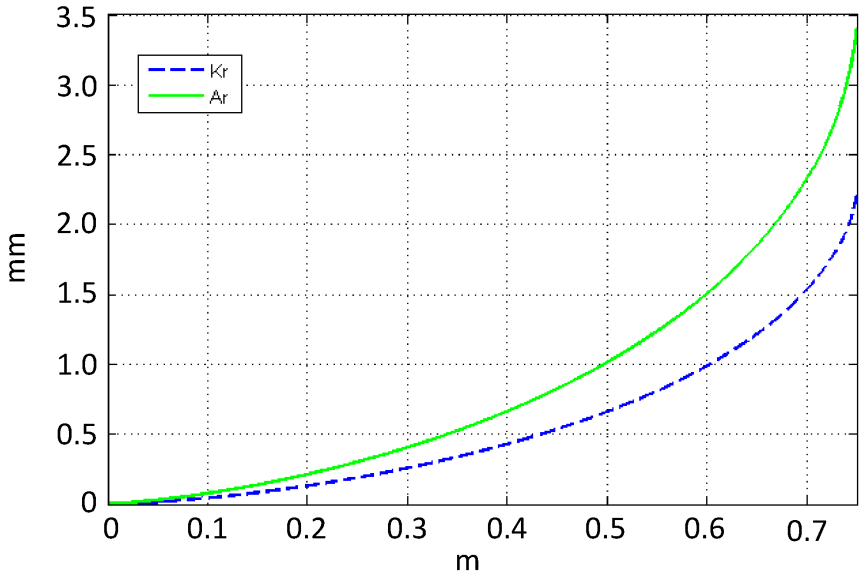

Figure 4.15: Transverse divergence for the highest captured velocity groups of krypton (245 m/s) and argon (250 m/s). The maximum divergence appears to be ∼2.2 mm radius over the 75 cm Zeeman slower length for krypton and ∼3.4 mm for argon. The atomic beam is expected to continue expanding on the way to the MOT, in the absence of transverse cooling.

After the Zeeman slower, the beam will continue to expand as it travels ∼24 cm to the MOT. The beam must clear the 1.5 cm inner diameter of the Zeeman slower tube, and ideally be < 2 cm diameter by the time it reaches the MOT. For v_c, the transverse velocity at the Zeeman slower exit is given by

$$v_{x,\,\mathrm{rms}}^2 = \langle v_x^2 \rangle = N \langle \delta v_x^2 \rangle = \frac{N v_r^2}{3}, \tag{4.14}$$

$$v_{x,\,\mathrm{rms}} = v_r \sqrt{\frac{N}{3}} = \sqrt{\frac{\Delta v_z v_r}{3}}, \tag{4.15}$$

where $v_{x,\,\mathrm{rms}}$ is ∼0.67 m/s for krypton and ∼0.98 m/s for argon. Thus, assuming a 15 m/s slowed atom velocity and a 24 cm free propagation length, we obtain the total atom beam

diameters at the MOT of 3.2 cm for krypton and 4.5 cm for argon. The third transverse cooling after the Zeeman slower is needed to compensate for this expansion.

4.5.2 Construction

We built the Zeeman slower in the traditional tapered solenoid design. The coil was designed to have 18 longitudinal sections, and each section has one more layer of winding than the previous section, e.g. the first section has one layer and the second section has two layers. An exception is that the last section has 14 layers more than the previous one to produce the sharp peak of the B field at the end of the Zeeman slower as shown in Fig. 4.13. Each layer consists of a single, continuous 18 AWG kapton encapsulated copper wire starting at a copper plate, and ending at a particular length, depending on the section number. A square copper tube was welded on the plate to remove the dissipated heat.

Figure 4.16: A copper plate on which a square copper tube was welded for water cooling (left). Zeeman slower winding on a lathe (right).

An aluminum pipe with a 1.5" outer diameter was used as a frame. We used a lathe for winding and secured the first and last ∼1.5" of each layer with Loctite five min epoxy. After a layer was wound and epoxied at both ends, we applied two coats of electrically insulating varnish (Lakeshore VGE-7031). The first coat was allowed to dry before the second was applied. This serves the dual purpose of insulating and minimizing the indentations between the wires. The actual length of the Zeeman slower is 77.6 cm, which generates the desired

B field trajectory of 75 cm. The total length of the wire is ∼1975 m, and its weight is ∼15 kg.

The field profile from the Zeeman slower geometry is expressed as

$$B(z) = \frac{\mu_0 N I}{2} \sum_{j=1}^{18} \left(\frac{z - z_{i_j}}{\sqrt{r_j^2 + (z - z_{i_j})^2}} - \frac{z - z_{f_j}}{\sqrt{r_j^2 + (z - z_{f_j})^2}} \right), \tag{4.16}$$

where z_{i_j} and z_{f_j} are the coordinates of the beginning and end of the jth layer respectively, I is the current, N is the winding number per unit length, and r_j is the radius of the jth layer. This field is shown with a green line in Fig. 4.17.

4.5.3 Field measurements

After the Zeeman slower was built, we measured the axial magnetic field using a custom made gaussmeter which is based on the A1301 chip. An Ametek DLM 600 150-4 regulated power supply provided current to the Zeeman slower. The gaussmeter was positioned in the center of a nylon rod, which was held coaxially with the tube (to within ∼1mm) by a teflon spacer. A motor driven piston (Firgelli Automation FA-400-L-12-24) pushed the rod through the tube at a nearly constant rate while the gaussmeter was measuring the field. The output from the gaussmeter was digitized by a National Instruments Data Acquisition (DAQ) card. Data acquisition was started/stopped when the motor was started/stopped. Thus we obtained the B field as a function of position. As the piston's range is 61 cm, we swept from one end and from the other end separately and merged the two in order to cover the full range.

The first field measurement showed that the peak on the side of the copper plate was not as sharp as the simulated field. We modified the coil by disconnecting the last section and adding narrower layers of wire onto the outer layer. Since the radii of the new layers are quite large (due to the thickness of the inner layers), a higher current is required than what is needed for the rest of the slower. For this reason, we used a separate power supply for the new outer layer to find the optimal current setting. The currents from the two supplies were adjusted carefully to match the simulated B field. The currents of 0.67 A for the inner coil and 2.73 A for the outer coil yield the best agreement with the simulation

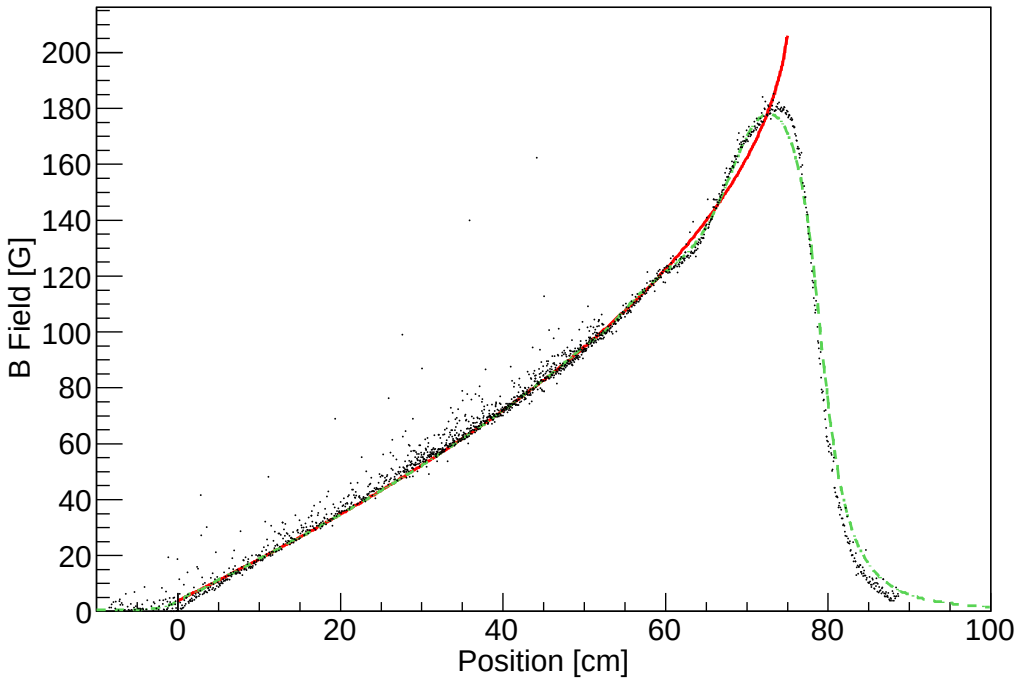

Figure 4.17: Measurement of the Zeeman slower field in the longitudinal direction. The direction of the atomic beam is defined as positive. The solid red line shows the ideal magnetic field; the dashed green line shows the calculated magnetic field from the Zeeman slower design; black dots show the measured magnetic field. The fluctuations of the measured fields are due to the internal fluctuations of the gaussmeter.

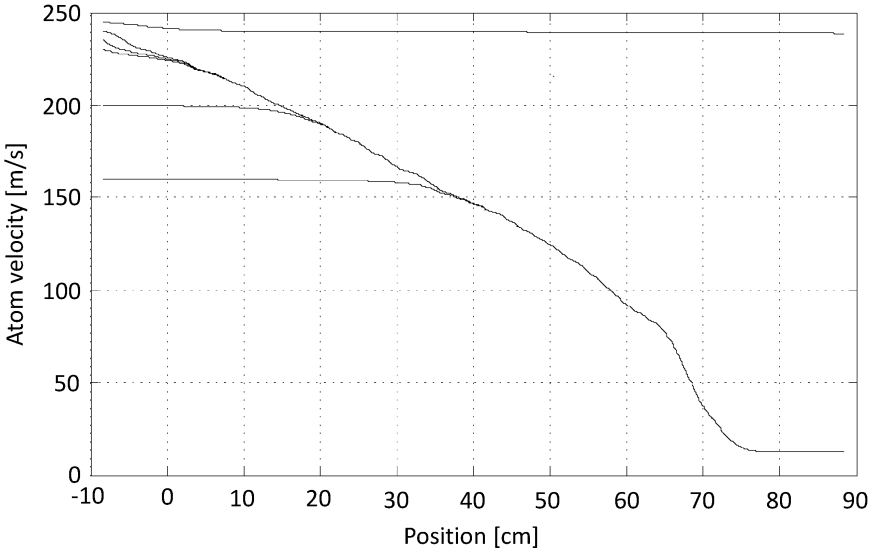

Figure 4.18: Velocity trajectory of Kr evaluated based on the measured Zeeman slower field.

(Fig. 4.17). The velocity trajectory for a krypton atom is simulated based on this measured B field along the Zeeman slower (Fig. 4.18).

Once the optimized current values were found, a potentiometer was connected to distribute a current from a single power supply into the inner and outer layers with the above fixed ratio for permanent use. Specifications for operating the Zeeman slower are summarized in Tab. 4.2.

Table 4.2: Zeeman slower specifications.

	Inner coil	Outer coil	Total
Length of wire [m]	∼1200	∼360	∼1560
Resistance [Ω]	2.97	0.88	3.85
Voltage across coil [V]	1.96	2.40	
Current [A]	0.66	2.73	
Heat dissipated [W]	1.27	8.88	10.2

4.6 Magneto-optical trap

A pair of anti-Helmholtz coils produce magnetic fields for three dimensional MOT as discussed in Sec. 3.4. The design of the coil was based on generating a magnetic field gradient of 10 G/cm in the vertical (z) direction with a 30 A current. These numbers are confirmed from the trajectories simulated for argon and krypton atoms in a one-dimensional MOT (Fig. 4.19), that are derived from Eq. 3.4. For a laser diameter of 4 cm, the capture velocity for argon is 35 m/s, and for krypton is 30 m/s. This indicates that the longitudinally decelerated atoms from the Zeeman slower, with a velocity of 15 m/s, are properly captured by our MOT.

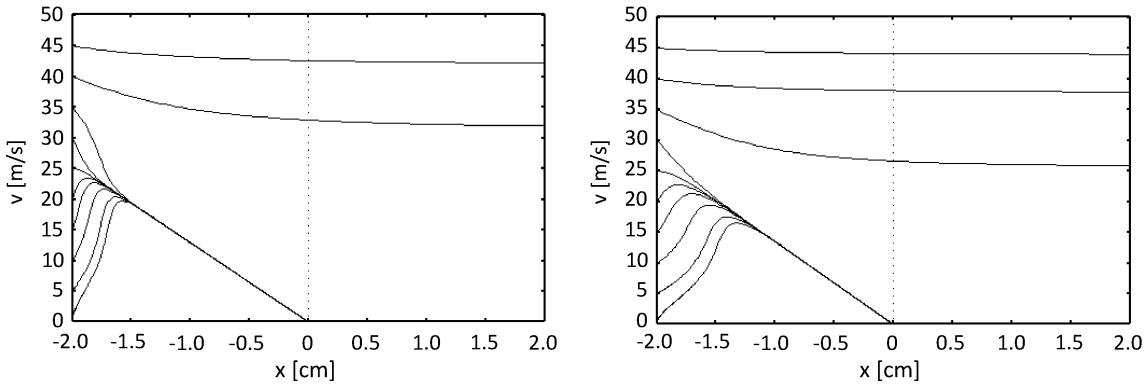

Figure 4.19: Atom trajectories in the one dimensional magneto-optical trap (MOT) for Ar (left) and Kr (right). The simulation uses Parameters $s_0 = 5, \delta/\gamma = -1$, and $\mathrm{d}B/\mathrm{d}z = 11$ G/cm.

Both top and bottom MOT coils have nine layers on aluminum cylinders, and each layer has nine windings. The z-component of the generated magnetic field along the z-axis (the axis of coil winding) is simulated by

$$B_z(z) = \frac{\mu_0 I}{2} \sum_{i=0}^{8} \sum_{j=0}^{8} \frac{(r_0 + id)^2}{((r_0 + id)^2 + (z - (z_0 + jd))^2)^{1.5}} - \frac{(r_0 + id)^2}{((r_0 + id)^2 + (z + (z_0 + jd))^2)^{1.5}}, \tag{4.17}$$

where μ_0 is the vacuum permeability, I is the current, r_0 is the radius of the cylinder, d is the thickness of the coil, z is the distance referenced to the center of the MOT, and i, j

indicate ith winding of the jth layer. The plots of this B field and its derivative are shown in Fig. 4.21.

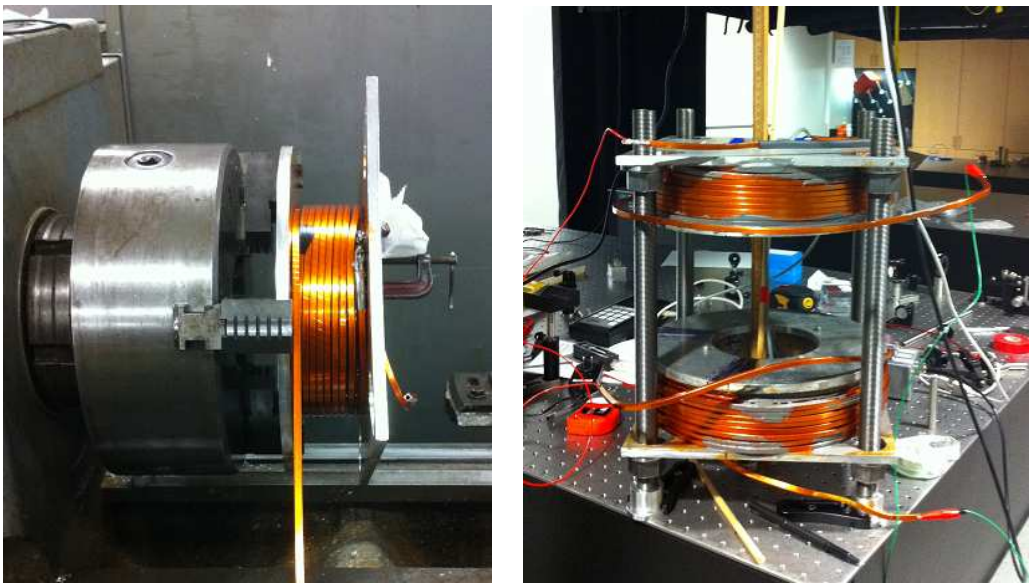

Figure 4.20: Winding the magneto-optical trap (MOT) coil (left) and MOT field measurement (right).

We built the MOT coils using copper wire from S&W Wire. It has a circular hollow inside a square cross section conductor to allow water to flow through the conductor and remove the dissipated heat from the coil. Its kapton taped surface insulates the conductor. We used the same lathe as for the Zeeman slower to wind the MOT coil, and varnished each layer to ensure insulation (Fig. 4.20 (left)). Care must be taken to protect the insulated surface from scratching during winding, since the wire is thick and stiff compared to the wire of the Zeeman slower. After winding, JB Weld was applied on the outer layer to secure the coil.

The MOT coils were brought to an optical table after construction, and set in the designed geometry without the vacuum chamber for the magnetic field measurement. Due to the complexity of the geometry, we manually positioned the gaussmeter instead of using the motor driven piston (Fig. 4.20 (right)). The measured B field in the z-direction and

its derivative at the current of 30 A are shown in Fig. 4.21. As simulated, the coils have its maximum B field of ∼120 G,and the dB/dz value at the MOT center is ∼11 G/cm. Figure 4.22 shows the measured B field and its derivative along the x-axis, which is perpendicular to the z axis and the Zeeman slower axis. The magnitudes along the x-axis are about half of those in the z axis, as predicted from geometry.

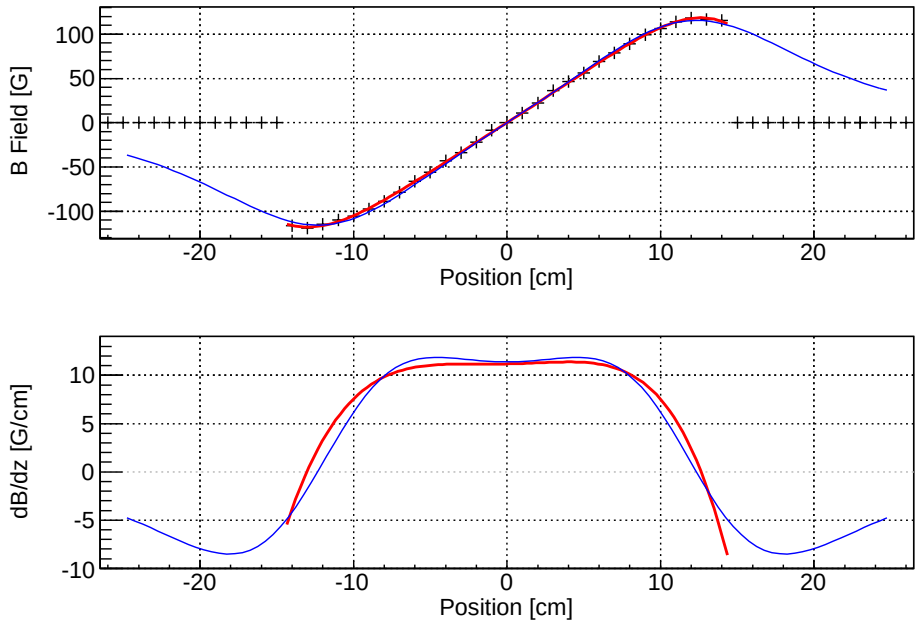

Figure 4.21: Magneto-optical trap (MOT) field (top) and its derivative (bottom) in the z-direction. Blue line is the simulation from the coil geometry, crosses are the measured values, and red line is a fit to a high order polynomial equation.

We used Solidworks to design the chamber suitable for both trapping and detecting, and it was custom-built by Kimball Physics. The chamber has four 4.5" flanges for detection, six 2.75" flanges for trapping lasers, and two 1.33" flanges for the Zeeman slower window and the connection to the vacuum system. We applied a low-outgassing black paint (AZ Technologies MLS-85SB) to the inner surface of the chamber to avoid light reflections. Thus, the surface is required to adhere the paint well. To choose the surface type, we tested the paint with three samples of different surface finishes from Kimball physics. The finishes are rough (Black Beauty sand, of unknown size), medium (blasted with #10 glass powder), and

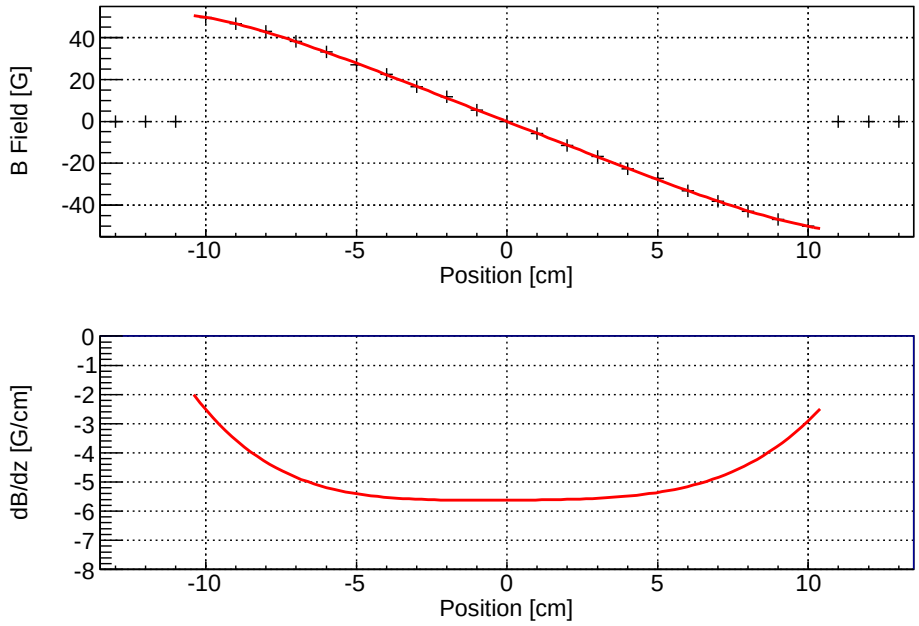

Figure 4.22: Magneto-optical trap (MOT) field (top) and its derivative (bottom) in the x-direction. Crosses are the measured values, and red line is a fit to a high order polynomial equation.

highly polished. The paint adheres better to rougher surfaces, but still adheres reasonably well to the highly polished finish. No flaking is observed, regardless of application thickness. The highly polished finish was selected to avoid the possibility that gas is trapped between the paint and the rough surface layer. We painted the chamber in a clean room at Columbia University, which has a low level of environmental pollutants. However, it turned out that the paint on the surface flakes off slightly after several weeks of operation.

As the windows should not be heated over 150°C, we first baked the chamber closed with blank flanges at a temperature ∼400°C for a week, then the blank flanges were replaced with anti-reflection coated windows while nitrogen gas flushes the system to prevent water and air from adhering to the walls during the process. After the windows installed, the chamber was baked again at a lower temperature. An optical breadboard, which is 30 cm above the table, supports the MOT chamber and the optical components (Fig. 4.23). One side of the breadboard was cut to avoid eddy currents induced by the MOT current switching.

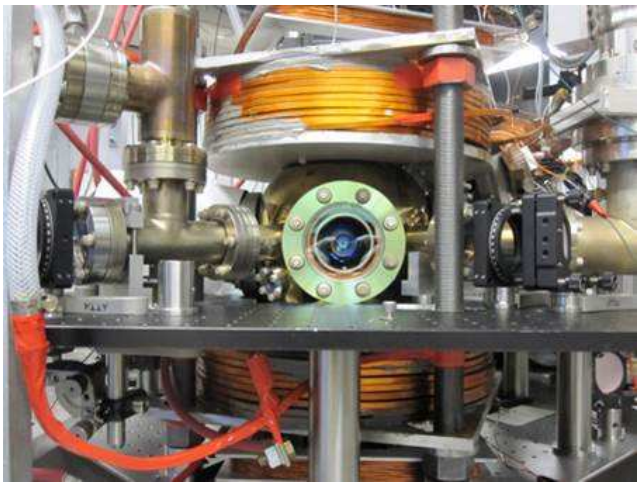

Figure 4.23: Chamber and coils for the Magneto-optical trap (MOT).

A power supply (Ametek DLM 600 150-4) provides the required current to the two MOT coils connected in series. The hollow inside the wire is connected to a temperature recirculating chiller (Thermo Scientific NESLAB Merlin M150) for water cooling. Addi-

tionally, three pairs of Helmholtz coils were added around the chamber to fine control the zero point of the magnetic field, and consequently the position of the MOT, which is critical for alignment of the single atom detection system. Table 4.3 summarizes the MOT specifications.

Table 4.3: Magneto-optical trap (MOT) specifications.

	Top coil	Bottom coil	Total
Length of wire [m]	∼30	∼30	∼60
Resistance [Ω]	0.05	0.05	1.01
Voltage across coil [V]	1.48	1.48	2.98
Current [A]	27.9	27.9	27.9
Power dissipated [W]	41.4	41.4	82.8

The laser beam for the MOT is expanded to a 2 cm radius, and split into three beams by beam splitting cubes. In our setup, the vertical beam has twice the power of horizontal beams. As we discussed above, the polarization of each beam should be set for σ^- transitions, so $\lambda/4$ waveplates are used to adjust beam polarizations before and after the chamber for each pair of beams. Three irises in front of the chamber adjust the sizes of the MOT beams, which is useful in controlling background level for a good resolution of single atom signals.

4.7 Laser shutter

Studies of the MOT loading and decaying are necessary for a detailed MOT characterization. To obtain practical loading and decay plots, it is required to switch on and off the MOT quickly so that the transition time does not affect the results. Switching the MOT can be achieved by several methods: switching the MOT coil current, the trapping laser, the Zeeman slower coil current, the Zeeman slower laser, or the atomic beam. Switching the currents may introduce inductance problems, and switching the Zeeman slower involves a possibility that residual slowed atoms in the system flow into the MOT after the Zeeman slower is turned off. However, a very small fraction of atoms are still trapped even without

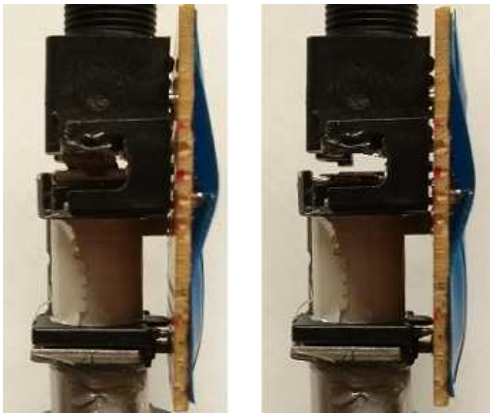

Figure 4.24: Custom-made laser shutter to mechanically switch on and off the Zeeman slower laser. It is normally closed (left) without any driving signal, and is open (right) while a 24 V input voltage is being applied.

the Zeeman slower. Blocking the atomic beam mechanically inside the vacuum would be ideal since it eliminates the light scattered off the atomic beam in the trap chamber [Du, 2003], but this requires a relatively complex setup compared to other methods. We used a mechanical shutter to block the Zeeman slower laser in this measurement.

The shutter consists of a solenoid relay (P&B Electronics T90N1D-12) that comes with a small metal contact opposite an electromagnet. This contact was removed so the full beam diameter could fit through the slot. Removing the contact increases the closing distance between the two magnets, so the relay requires more voltage to function properly. A DAQ card (National Instruments PCI Express 6321) and a terminal block (National Instruments SCB-68) generate the driving signal of 5 V, which is converted to a 24 V signal by a custom-made driver. The process is controlled with a C++ code using National Instrument DAQmx library. Figure 4.25 shows the shutter when it is closed and open.

For testing, the shutter was placed in a laser path and a photodiode recorded the laser power while the shutter switched on and off. The photodiode signal versus time is plotted in Fig. 4.25, which shows that the opening delay is consistently longer than the closing delay. The bounce in the optical signal can be avoided with careful alignment; if the light is too near the closing stop, the bounce will be apparent. The shutter opens and closes sufficiently

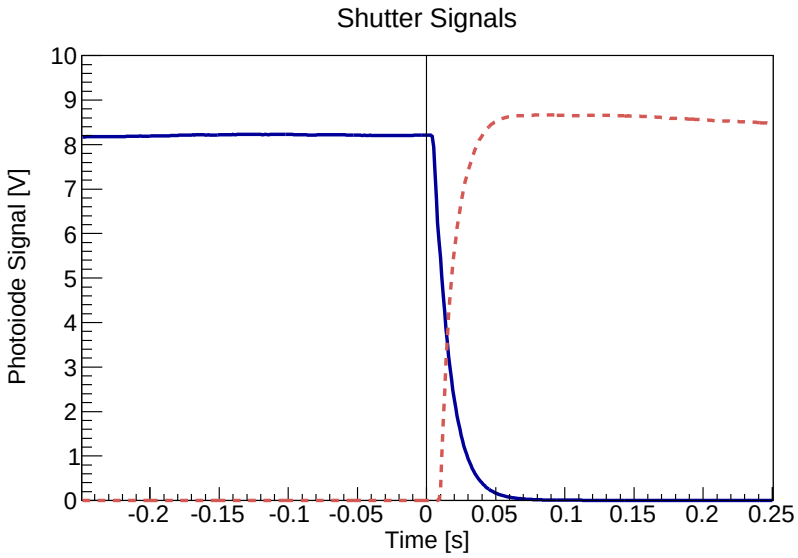

Figure 4.25: Photodiode signal with time for opening (solid blue line) and closing (dashed red line) of the shutter. The trigger signal is transmitted to the shutter at $t = 0$ for both cases.

quickly that we did not see a marked effect from the transition.

Chapter 5

Cooling and trapping

One of the main challenges of this experiment is to achieve the loading rate that is high enough to detect a part per trillion (ppt) level of krypton contamination within a reasonable amount of time. A low loading rate would require a longer measurement time, which results in stricter requirements on long-term system stability. We incorporated several stages to increase the loading efficiency, and all the stages were adjusted and optimized carefully. Argon gas was used for testing and optimization to avoid krypton contamination prior to measuring xenon samples. This chapter deals the optimization processes for a high loading efficiency, and characterizes in samples of trapped argon atoms.

5.1 Source cooling

As discussed in Sec. 4.5, the Zeeman slower can decelerate argon atoms with velocity below 250 m/s, and krypton atoms with velocity below 245 m/s. At equilibrium, particle velocity distributions in gases can be described by the Maxwell-Boltzmann (MB) law, if atoms or molecules have no internal structure and interact via other particles only via elastic collisions. From the Boltzmann energy distribution, one can derive the one-dimensional velocity distribution $f(v)$,

$$f(v) = \frac{1}{\sqrt{2\pi}\tilde{v}} \exp\left(-\frac{v^2}{2\tilde{v}^2}\right), \tag{5.1}$$

where

$$\tilde{v} \equiv \sqrt{\frac{k_B T}{M}}. \tag{5.2}$$

The velocity distributions for gases of particles (1D and 3D) and for a thermal beam are summarized in the Tab. 5.1.

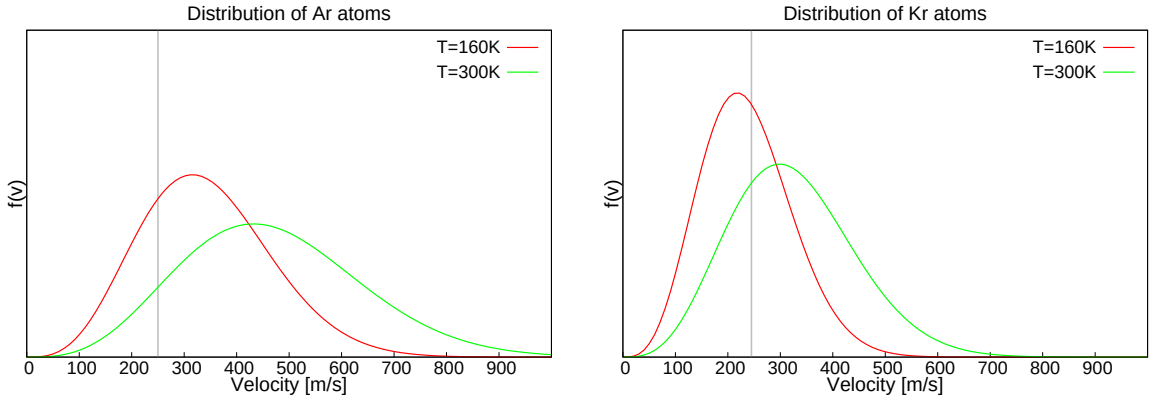

Figure 5.1: Maxwell-Boltzmann distributions at 160 K and 300 K for argon (left) and krypton (right) beams. The vertical gray lines indicate the capture velocity of the Zeeman slower, 250m/s for argon and 245m/s for krypton. The area left of the gray line, bounded by $f(v)$ and $y = 0$, implies the fraction of atoms decelerated by the Zeeman slower.

At the planning stage, we assumed that the atoms in the ATTA system would follow the distribution of a thermal beam (which was experimentally confirmed later). The velocity distributions of argon and krypton atoms in a thermal beam are shown in Fig. 5.1. The fraction of atoms which can be slowed by the Zeeman slower is calculated as

$$f_c(v_c) = \int_0^{v_c} f(v)\mathrm{d}v, \tag{5.3}$$

where v_c is the capture velocity of the Zeeman slower; 250 m/s for argon and 245 m/s for krypton. At room temperature (300 K), our Zeeman slower is projected to decelerate 29% of krypton atoms and 9% of argon atoms. These fractions can be increased by lowering the gas temperature. Figure 5.2 (top, left) shows the fraction of argon atoms decelerated by our Zeeman slower as a function of gas temperature with each velocity distribution in Tab. 5.1.

We use a pulse tube refrigerator (PTR) with an air-cooled helium compressor for cooling the atomic gas before optically slowing it. A copper cold finger connects the copper holder of

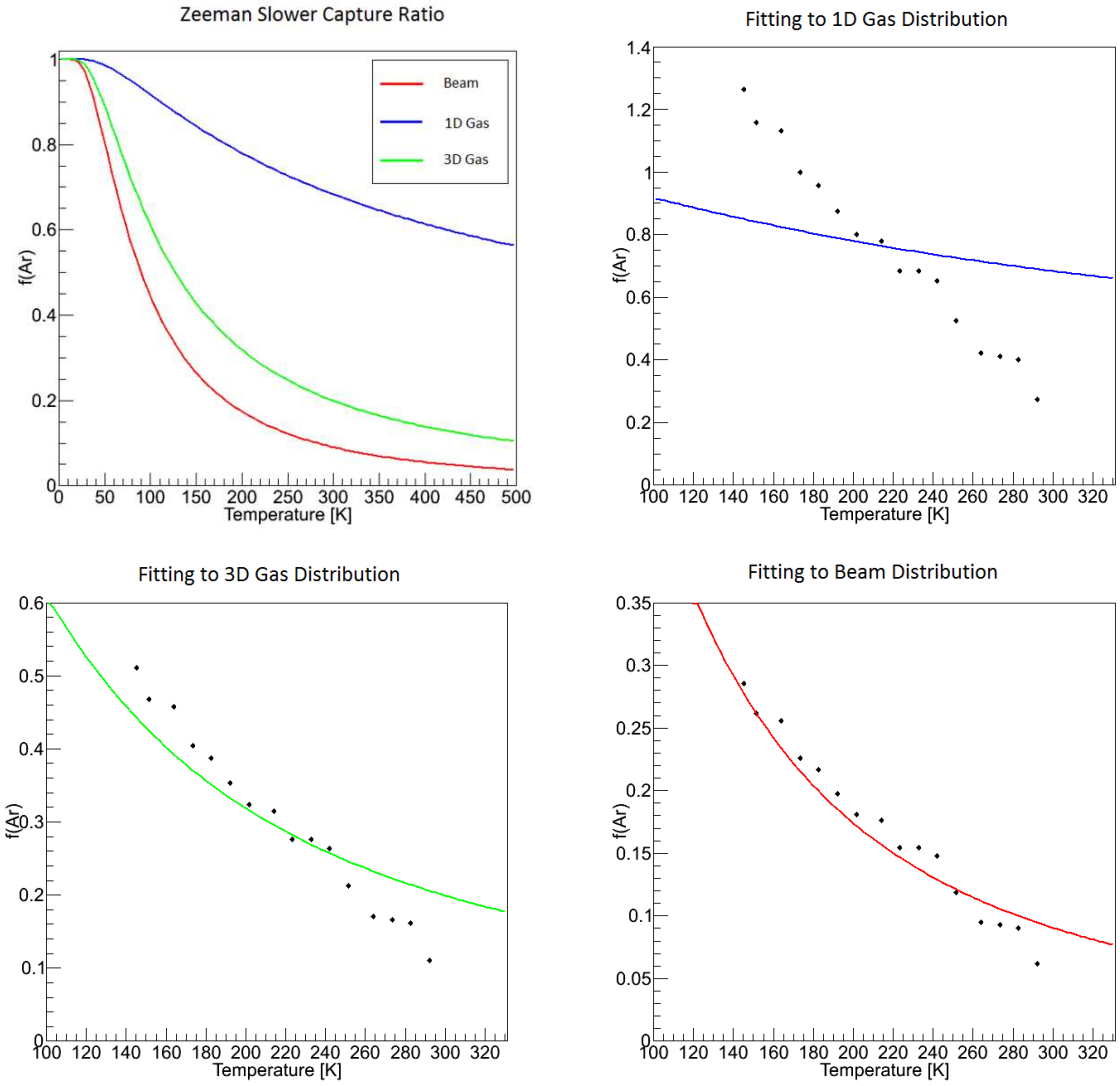

Figure 5.2: Capture fraction of the Zeeman slower for 1D, 3D gases and for a beam of argon atoms (top, left) and the relative intensity of magneto-optical trap (MOT) in the function of temperature. Solid lines are the calculated capture fraction, and black dots are measured MOT intensities, the data points are fitted to the distribution of 1D gas (top, right), 3D gas (bottom, left), and beam (bottom, right). The data are independently scaled to the level of each distribution curve.

Table 5.1: Velocity distributions for gases of particles (1D and 3D) and for a thermal beam. Here, v_{mp} is the most probable velocity, v_{ave} is the average velocity, and v_{rms} is the root mean square velocity. Table from [Metcalf and van der Straten, 1999].

	Distribution $f(v)$	Range	v_{mp}	v_{ave}	v_{rms}
Gas (1D)	$\frac{1}{\sqrt{2\pi}\tilde{v}}\exp\left(-\frac{v_x^2}{2\tilde{v}^2}\right)$	(-∞, ∞)	0	0	$\tilde{v}$
Gas (3D)	$\sqrt{\frac{2}{\pi}}\frac{v^2}{\tilde{v}^3}\exp\left(-\frac{v^2}{2\tilde{v}^2}\right)$	(0,∞)	$\sqrt{2}\tilde{v}$	$\sqrt{\frac{8}{\pi}}\tilde{v}$	$\sqrt{3}\tilde{v}$
Beam	$\frac{v_z^3}{2\tilde{v}^4}\exp\left(-\frac{v_z^2}{2\tilde{v}^2}\right)$	(0,∞)	$\sqrt{3}\tilde{v}$	$\sqrt{\frac{9\pi}{8}}\tilde{v}$	$2\tilde{v}$

the AlN tube to the PTR (Fig. 4.7), and removes the heat from the source. The connections between the copper pieces are filled with thermally conductive grease (Apiezon N Grease) that is compatible with a cryogenic high vacuum. The PTR cools the source to ∼120 K when the source is off. When the source discharge is running, the source temperature in equilibrium is ∼160 K. At 160 K, the decelerated fraction of the Zeeman slower increases to 24% for argon and 57% for krypton.

The Zeeman slower efficiency dependence on temperature is inferred from relative magneto-optical trap (MOT) intensities. For these measurements, the source was first cooled down to 120 K, then the PTR was turned off. We measured the MOT intensity every 5 K as the temperature went up to room temperature. The measured data best fit the MB distribution for a thermal beam (Fig. 5.2), confirming the previously made assumption.

5.2 CCD camera calibration

A CCD camera (ThorLabs DCU224M + Tamron 1134698) detects fluorescent light from metastable atoms, and the image is processed by a computer connected to the camera. The image brightness was calibrated in terms of light intensity. To avoid saturation of the camera image, we prepared a very weak laser with power $P = 7.3$ μW by adding several neutral density (ND) filters to one laser path. The laser power was measured by an optical

power meter (ThorLabs PM100D). Then, the CCD camera was used to image the laser, and the brightness level of each pixel was extracted from the image on a 256-level scale. The 7.3 μW laser power corresponds to the brightness sum of 4.7×10^6 at the camera exposure time $t = 0.079$ ms, which is further calibrated in terms of the photon number.

The laser energy incident on the camera sensor is

$$E = P \times t = 7.3\ \mu\text{W} \times 0.079\ \text{ms} = 5.8 \times 10^{-10}\ \text{J}. \tag{5.4}$$

Since one photon of the 811.7542 nm wavelength has energy of $E_{\text{photon}} = hc/\lambda = 2.45 \times 10^{-19}$ J, the number of photons in the image is $N_{\text{photon}} = E/E_{\text{photon}} = 2.4 \times 10^9$. Finally, the number of photons per one brightness unit is derived as

$$\frac{2.4 \times 10^9\ \text{photons}}{4.7 \times 10^6\ \text{brightness units}} = 511\ \text{photons/brightness unit}. \tag{5.5}$$

This number is used for all measurements using the CCD camera in the experiment.

The size of an object in an image was simply calibrated using an image of a ruler. A ruler was positioned 17.5 cm away from the camera, where the camera has a focused image on its sensor. By counting the pixel number according to the ruler scale in the image, we obtained the value of 432 pixels/cm. This number depends on the camera lens choice, while the brightness calibration is valid for any lens systems.

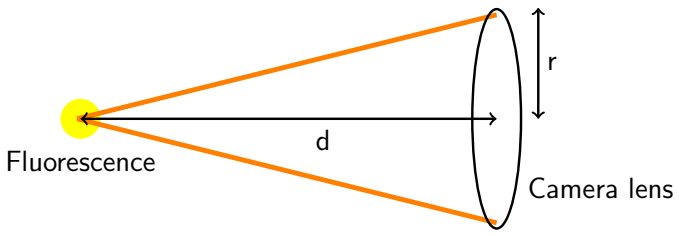

Figure 5.3: Schematic of fluorescence detection with the camera.

Figure 5.3 shows a schematic of an atomic fluorescence measurement. The solid angle to the camera lens is expressed as

$$\Omega \simeq \frac{\pi r^2}{4\pi d^2}, \tag{5.6}$$

where r is the radius of the camera lens and d is the distance from the fluorescence source to the camera lens. Using the value derived in Eq. 5.5 and camera parameters, we estimate the number of atoms as

$$N_{\text{atom}} = \text{Brightness} \times \frac{1}{511} \times \frac{1}{\Omega} \times \frac{1}{R_{\text{scatt}}} \times \frac{1}{t_{\text{exp}}} \times \frac{1}{G}, \tag{5.7}$$

where R_{scatt} is the scattering rate in Eq. 3.13 at the given light intensity and detuning, t_{exp} is the exposure time, and G is the gain setting of the camera.

5.3 Consumption rate of argon

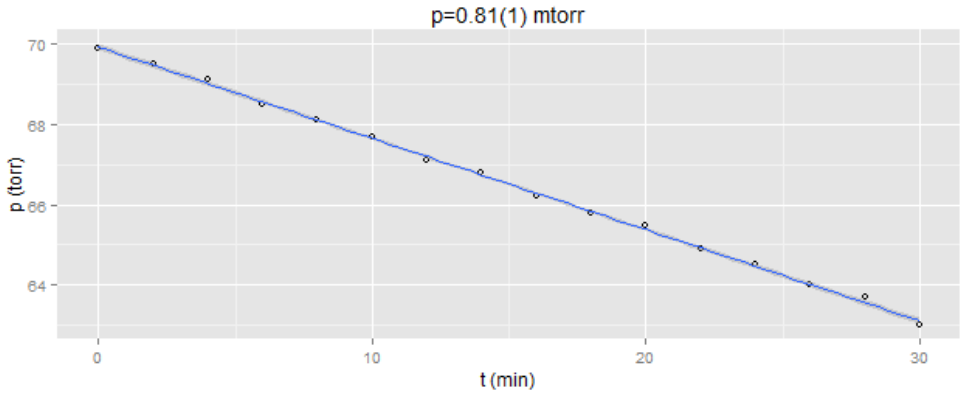

Figure 5.4: Pressure in the reservoir decreases linearly with time as the gas is consumed. The pressure in the source chamber is maintained at 0.81 mtorr.

The gas consumption rate is defined as the number of atoms per second that come into the system from the reservoir. To estimate the consumption rate of the source, we filled the reservoir with argon gas and let it flow out into the source chamber through the fine leak valve. The pressure in the reservoir was measured every two minutes (Fig. 5.4), and the pressure change per unit time, $dP(t)/dt$, was derived. During the measurement, the pressure at the source chamber was carefully maintained at a fixed level in order to determine the consumption rate as a function of source pressure. The time derivative of the ideal gas equation is

$$\left(\frac{dP}{dt}\right) V = \left(\frac{dN}{dt}\right) k_B T, \tag{5.8}$$

where V it the reservoir volume and N is the number of atoms. Then the consumption rate is

$$C = -\frac{\mathrm{d}N}{\mathrm{d}t} = \frac{\mathrm{d}P}{\mathrm{d}t}\frac{V}{kT}. \tag{5.9}$$

Table 5.2: Consumption rates of argon gas for different pressures in the source chamber.

Source chamber pressure [mtorr]	0.61	0.70	0.81	1.00
Consumption rate [10^{16} s^{-1}]	5.8	6.5	7.8	9.2

The consumption rate was measured at several pressures in the source chamber around 0.8 mtorr, where the efficiency of the argon discharge is optimized. By inserting the estimated reservoir volume $V = 6.3 \times 10^{-4}$ m^3 and the gas temperature $T = 290$ K, we obtain consumption rates presented in Tab. 5.2, which are also plotted in Fig. 5.5.

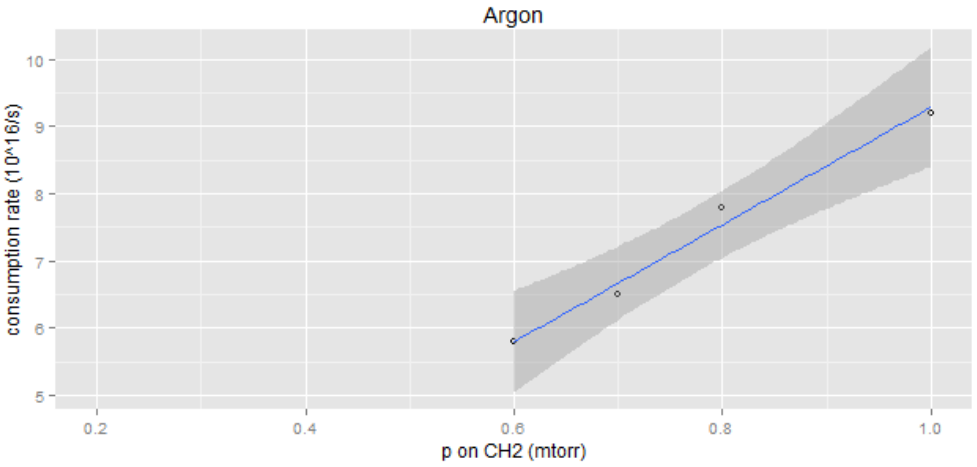

Figure 5.5: Consumption rates of argon gas for different pressures in the source chamber. The consumption rate increases linearly with the source chamber pressure. The gray region shows 1 σ confidence interval.

5.4 Atomic flux

The study of the metastable atomic flux at the first transverse cooling stage together with the consumption rate and the MOT loading rate characterizes the excitation efficiency of

the source and the cooling and trapping efficiency of the system. To measure the flux, a fluorescence laser ($\vec{x}$) was set perpendicular to the atomic beam direction ($\vec{z}$), and the CCD camera observed the fluorescence light from a horizontally transverse direction ($\vec{y}$). The scheme of the measurement is shown in Fig. 5.6.

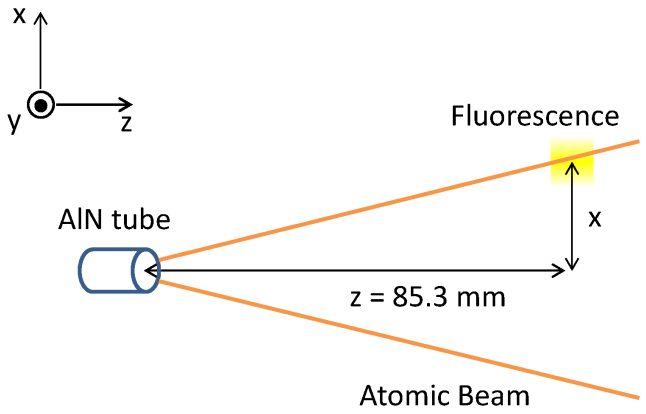

Figure 5.6: Schematic of the fluorescence measurement in the 1st transverse cooling (TC) chamber.

Images were taken for several laser detunings, and the position and intensity of the fluorescence light were analyzed in each image. The pressure in the source chamber was maintained at 0.81 mtorr during the measurement. At various detunings, the laser interacts with atoms that have corresponding velocities determined by the Doppler effect

$$f = f_0 - \Delta f = (1 - \frac{\Delta v}{c}) f_0, \tag{5.10}$$

where f is the laser frequency. The fluorescence is located at $x = 1.37$ mm for the laser locked to a detuning of $\Delta f = -5.61$ MHz. With this detuning and Eq. 5.10, the transverse velocity of the fluorescent atoms is derived as

$$v_x = \Delta v = c\frac{\Delta f}{f_0} = 4.55 \text{ m/s}. \tag{5.11}$$

Since the horizontal distance z is much larger than the diameter of the AlN tube, we assume that the atomic beam disperses from a single point (the end of the tube). Then we have the relation

$$\frac{v_x}{x} = \frac{4.55 \text{ m/s}}{1.37 \text{ mm}} = 3.32 \times 10^3/\text{s} \tag{5.12}$$

from the triangular geometry. Using this relation, the transverse atomic velocities at each detuning atoms are derived in Tab. 5.3. It also allows us to estimate the longitudinal velocity of the atomic beam,

$$v_z = 85.3 \text{ mm} \times \frac{v_x}{x} = 283 \text{ m/s}. \tag{5.13}$$

With the MB distribution of a thermal beam, the most probable velocity of 283 m/s leads to the gas temperature of 129 K.

Table 5.3: Characteristics of fluorescent atoms at five different laser frequencies.

Position x [mm]	Velocity v_x [m/s]	Relative intensity	Atom density [10^6 mm^{-3}]
0.45	1.5	100.0	5.83
5.25	17.5	72.0	4.20
9.30	31.0	42.8	2.50
12.15	40.5	29.7	1.73
14.85	49.5	21.3	1.24

The number of atoms in the fluorescence region is obtained from Eq. 5.7, then we estimate the atom density n, using the laser beam size. The calculated atom densities are presented in Tab. 5.3 and plotted in Fig. 5.7.

To estimate the atomic flux, the density $n(x)$ has to be integrated over the cross sectional area. By fitting a Gaussian distribution to the calculated atom densities, we determine the atom density profile as a function of the distance from center,

$$f(x) = A \exp\left(-\frac{x^2}{2\sigma^2}\right), \tag{5.14}$$

where $A = 5.4 \times 10^6$ cm^{-3}, and $\sigma = 8.09$ mm. Integrating Eq. 5.14 over the x-y plane gives the linear density

$$n_z = \int_0^\infty \int_0^{2\pi} f(x)\, d\theta\, dx = 2\pi A\, \sigma^2 = 2.22 \times 10^7 \text{cm}^{-1}. \tag{5.15}$$

Finally, the product of the longitudinal velocity (Eq. 5.13) and the linear density (Eq. 5.15) determines the metastable atomic flux

$$\text{Flux} = v_z \times n_z = 6.3 \times 10^{11}/\text{s}. \tag{5.16}$$

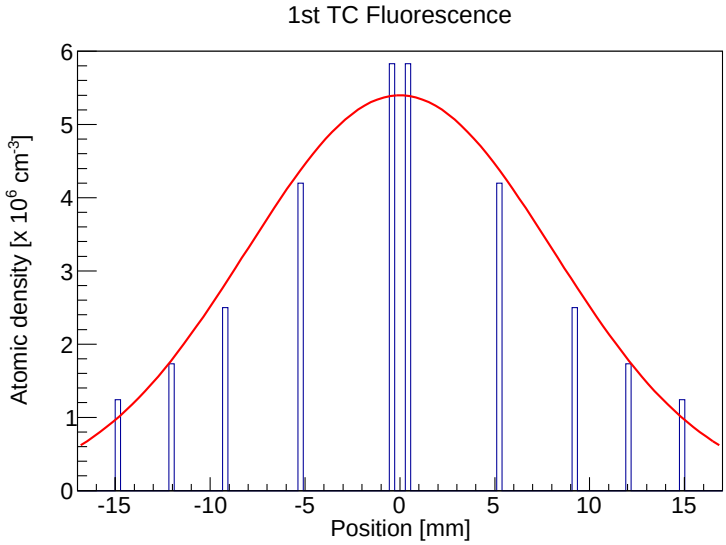

Figure 5.7: Histogram of atomic densities as a function of position. The five data points at positive values of x are measured, and are reflected through the origin for visualization.

Given the gas consumption rate at the 0.81 mtorr source chamber pressure (Tab. 5.2), Eq. 5.16 yields the excitation efficiency of the discharge source of $\sim 10^{-5}$ for argon, which is slightly lower than that in previous studies [Chen *et al.*, 1999; McKinsey and Orzel, 2005].

5.5 Magneto-optical trap of argon

The argon MOT is observed by a CCD camera through a window in a 6" flange of the MOT chamber. The camera is located 17.5 cm away from the center of the MOT chamber on the optical table, resulting in a solid angle of 8.3×10^{-4} to the camera lens. From the brightness sum of the MOT image, the number of trapped atoms is inferred using Eq. 5.7. Since the frame speed of the CCD camera (30 frames/s) is not fast enough, a photodiode (ThorLabs DET36A) is employed to read the MOT intensity through another window. The output voltage from the photodiode is directly calibrated to the atom number derived from the CCD camera.

For the maximum loading rate, all system parameters were carefully adjusted. During optimization, the system efficiency was inferred via the number of trapped atoms which can

be observed in real time while deriving the loading rate requires additional measurements. It turns out that the number of atoms is a good indicator of the loading rate in our case (Eq. 5.18). Table 5.4 summarizes the contribution of each stage to signal enhancement. It is more challenging to adjust the third transverse cooling stage than the first two because the residual fields from the MOT and the Zeeman slower contribute unexpected Zeeman shifts to the transition energy.

The Zeeman slower current was readjusted to find the brightest MOT from the current previously determined by the field measurement, 0.67 A for the inner coil and 2.73 A for the outer coil (Sec. 4.5.3). We obtained the new optimal currents of 0.66 A for the inner coil and 3.17 A for the outer coil. The difference may be due to the residual field of the MOT coil or the actual MOT capture velocity being different from the designed exit velocity of the Zeeman slower (15 m/s). With the Zeeman slower off, we barely see any MOT image from the CCD camera, but a small number of trapped atoms can be observed by single atom detection.

Table 5.4: Contribution of each stage to the loading rate.

Stage	Increase factor	Notes
Source cooling	4	
1st transverse cooling (TC)	20	4.5×4.5
2nd TC	2	
3rd TC	1.2	
Zeeman slower	>1000	

The number of trapped atoms is modeled by

$$\frac{\mathrm{d}N(t)}{\mathrm{d}t} = L - \frac{N(t)}{\tau} - \beta N(t)^2, \tag{5.17}$$

where L is the loading rate, τ is the mean trap lifetime, and β is the quadratic collision term. The second term on the right-hand side represents the loss from collisions with background atoms, and the third term indicates the loss from collisions between trapped atoms. If the MOT volume expands with a fixed density when the number of trapped atoms increases,

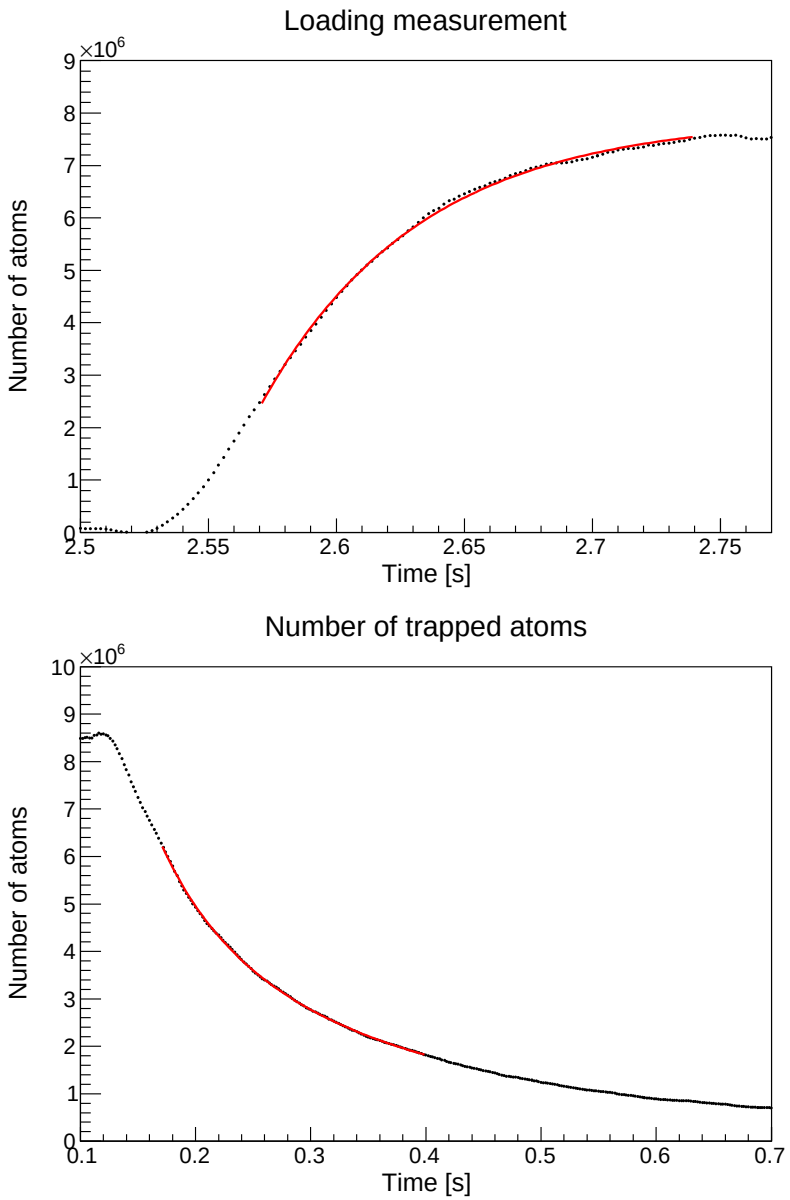

Figure 5.8: Loading (top) and decay (bottom) plots for the argon MOT. Black dots are data, and red lines are fits to the solution of Eq. 5.18.

as is the case here, Eq. 5.17 is modified to

$$\frac{\mathrm{d}N(t)}{\mathrm{d}t} = L - \frac{N(t)}{\tau} - \beta n N(t), \tag{5.18}$$

where n is the fixed atom density [Steane *et al.*, 1992; Marcassa *et al.*, 1993]. Solving Eq. 5.18 yields the solution

$$N(t) = \frac{L}{\dfrac{1}{\tau} + \beta n} + c_1 \exp\left[-\left(\frac{1}{\tau} + \beta n\right) t\right], \tag{5.19}$$

where c_1 is a coefficient. Especially, when $L = 0$, the solution is

$$N(t) = N_0 \left(1 - \exp\left[-\left(\frac{1}{\tau} + \beta n\right) t\right]\right), \tag{5.20}$$

where N_0 is the equilibrium number of trapped atoms.

Table 5.5: Characteristics of the ATTA system with argon.

Parameters	Values
Trapped atom number	8×10^6
Consumption rate	7.8×10^{16} s^{-1}
Metastable atom flux	6.3×10^{11} s^{-1}
Source efficiency	0.8×10^{-5}
Loading rate	1.5×10^8 s^{-1}
Overall efficiency	1.9×10^{-9}

Figure 5.8 shows the loading and decay plots for the argon MOT. Fitting Eq. 5.20 to the decay data determines the values of the constant N_0 and coefficients $\tau = 0.47$ s and $\beta n_c = 9.7$/s. By inserting these into Eq. 5.18 in steady state, i.e., $\mathrm{d}N(t)/\mathrm{d}t = 0$, we obtain the loading rate $L_{\mathrm{Ar}} = 1.79 \times 10^8$/s. Taking into account the factor of 2.1 from the efficiency enhancement of the Zeeman slower for krypton and assuming that other properties of the system remain the same, we expect the krypton loading rate $L_{\mathrm{Kr}} = 3.76 \times 10^8$/s. Thus, the loading rate for 1 ppt krypton contamination would be $L_{\mathrm{Kr-1ppt}} = 3.76 \times 10^{-4}$/s, implying that it should take 78 minutes on average to load one trapped atom. The characteristics of the argon MOT are summarized in Tab. 5.5.

Chapter 6

Single atom detection

It is essential to have the ability to detect single atom signals in order to measure trace contaminations. The trapped atoms in the MOT are detected by the fluorescence light they emit due to the MOT laser beams. In our MOT, one trapped argon atom emits $\sim 10^7$ photons/s at sufficiently high laser intensities. To detect single atoms, we are required to collect as many photons as possible with minimized background. The single atom detection system was designed for this purpose. In this chapter, we discuss design and testing of this system.

6.1 Avalanche photodiode

We use an avalanche photodiode (APD, Perkin-Elmer single photon counting module SPCM-AQRH-12) to detect single atom signals. It has a quantum efficiency of 45% at 830 nm and a dark count of 500 Hz according to the manufacturer's specification. The measured dark count in our lab is $\sim$300 s^{-1}. The active area of the APD has a 180 μm diameter. With a 50 Ω load, the APD generates a 2.5 V TTL pulse of a 15 ns width as each photon is detected [Elmer, 2007].

As it is known that the single photon counting module (SPCM) can be damaged by exposure to a 10^6 counts/s level of light for more than a few milliseconds [Gordon and Selvin, 2003], we developed a failsafe circuit to protect the APD from overexposure using a microcontroller (Arduino ATmega328). The schematic of the circuit is shown in Fig. 6.1.

Since the ATmega328 is not fast enough to count pulses at megahertz rates, the failsafe circuit employs an external counter, 74LS590. The LS590 has an 8-bit binary counter that feeds an 8-bit storage register, enabling the count value to be transferred to the register and the counter cleared while the register is being read out. When the count rate exceeds 300 kHz, the circuit shuts off automatically and a red LED lights up. The failsafe also relays the generated APD signal to a DAQ card (National Instruments PCI Express 6321) connected to a computer. The signal is displayed and recorded in units of photons/s by a National Instrument LabView program.

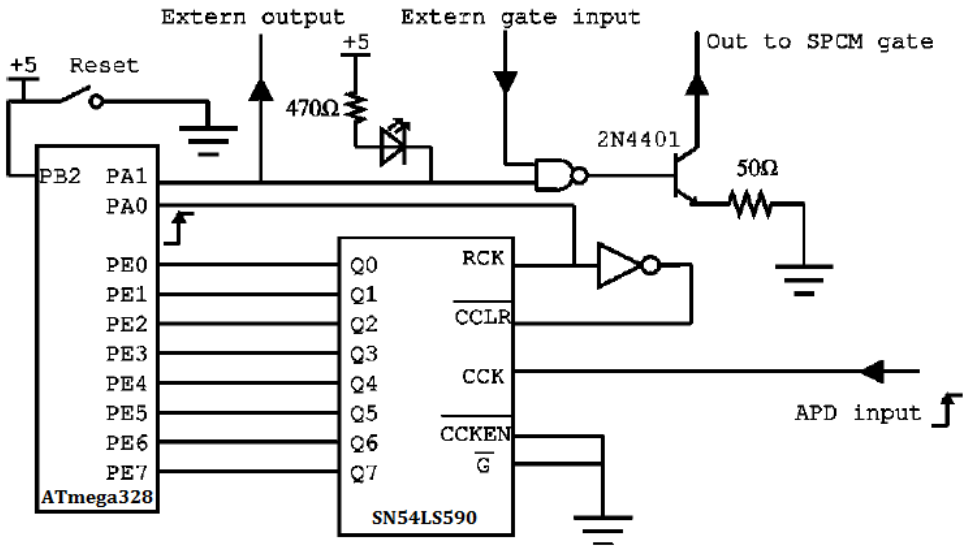

Figure 6.1: Prototype schematic of the APD failsafe circuit. Figure from [Gordon and Selvin, 2003].

6.2 Optics

Figure 6.2 shows the sketch of our single atom detection system. The system was carefully designed to efficiently gather the emitted photons from trapped atoms while filtering out any background photons. The background comes from various sources: ambient light entering through the chamber windows, fluorescence light from the atomic beam, and the MOT

lasers reflected inside the chamber.

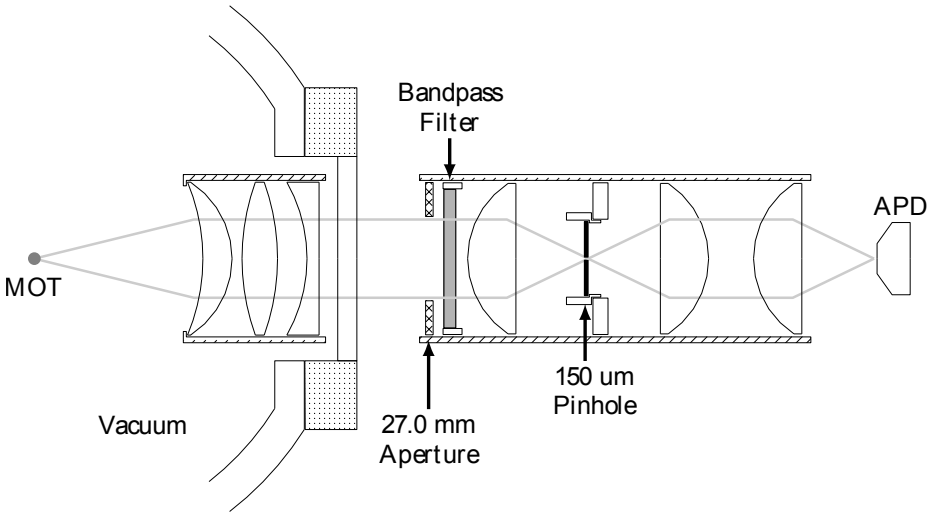

Figure 6.2: Schematic of the single atom detection system. The specially designed collimating lenses are installed inside the vacuum to increase the effective solid angle, and three aspheric lenses are used outside the chamber for focusing and imaging. A bandpass filter removes ambient light, and a 150 μm pinhole filters out stray reflections from the chamber.

A 810 ± 5 nm bandpass filter (Edmund Optics 67-916) filters out ambient light, and a circular pinhole blocks light outside the expected signal path. It is important to find the proper pinhole size to get the best signal to noise ratio (SNR), as both the signal and background transmission increase with a larger pinhole diameter. After tests with several different size pinholes, a 150 μm diameter pinhole was selected since it best balances the high signal level and the low background level. The bandpass filter is located where the signal beam rays are in parallel since it has a higher transmission for normal incidence. The transmission versus the angle of incidence is reported in Tab. 6.1. Since the directions of background light rays are disordered while the light rays are parallel in the region, the bandpass filter can selectively block background light even if it has the same wavelength as the signal.

The optics and the APD are housed in a plastic box to block ambient light, and the space between the window of the box and the chamber is enclosed by a black rubber bellow tube (Fig. 6.4). The APD is mounted on a three-axis translation stage for fine adjustment,

Table 6.1: Transmission measurement of the bandpass filter (Edmund Optics 67-916) as a function of the incidence angle.

Incident angle	No filter	90°	85°	80°	75°	70°
Power [μW]	493.9	286.4	285.0	269.6	79.1	0.1
Transmission [%]	100	58.0	57.7	54.6	16.0	0.0

with the control knobs extended out of the box through holes that are light-tight sealed with black rubber pieces. Thus we can control the APD position when the box is closed.

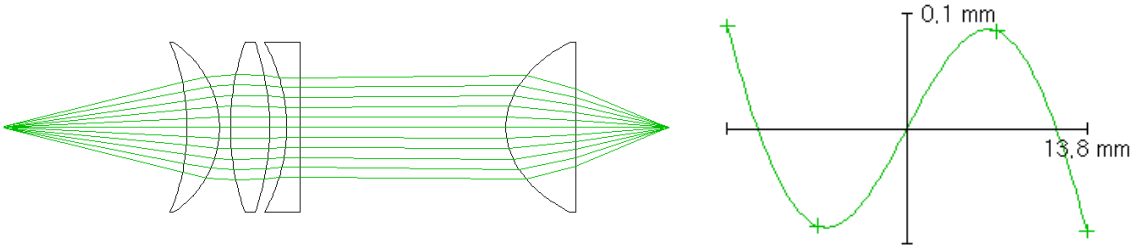

Figure 6.3: Beam trace (left) and transverse aberration (right) from the OSLO simulation. In the aberration plot, the x axis is the distance of a light ray to the optical axis at the surface of the first lens and the y-axis is the distance of the ray to the axis at the position of the pinhole. A beam within a radius of 13.8 mm can be focused into the area of the 180 μm diameter.

To increase the effective solid angle, the first collimating lens is installed ins vacuum, 50 mm from the center of the MOT chamber. In the first design, a single aspheric lens was used as this objective lens, but it produced large spherical aberrations, and only a fraction of photons was focused into the APD sensor. A multiple lens system has better focusing and solves this problem by compensating for the aberrations of one surface with the aberrations of the other ones. The new lens system was designed using the program OSLO (Fig. 6.3). Candidate optics were selected among commercially available lenses, and then the position of each lens was optimized for the minimal aberration, - specifically, to maximize the amount of light focused onto the APD active area. We use three lenses

instead of four, which is adopted in other groups [Alt, 2002; YanQiang *et al.*, 2012], due to the limited space inside the vacuum. The OSLO simulation shows that our system has almost the same performance as a quadruple lens system. We expect that photons inside the radius of 13.5 mm on the surface of the in-vacuum objective can be focused properly by the optics. An aperture with a 13.5 mm diameter is mounted to block any light outside this area since background is large than the signal in that region. This leads to the useful solid angle of 1.8%.

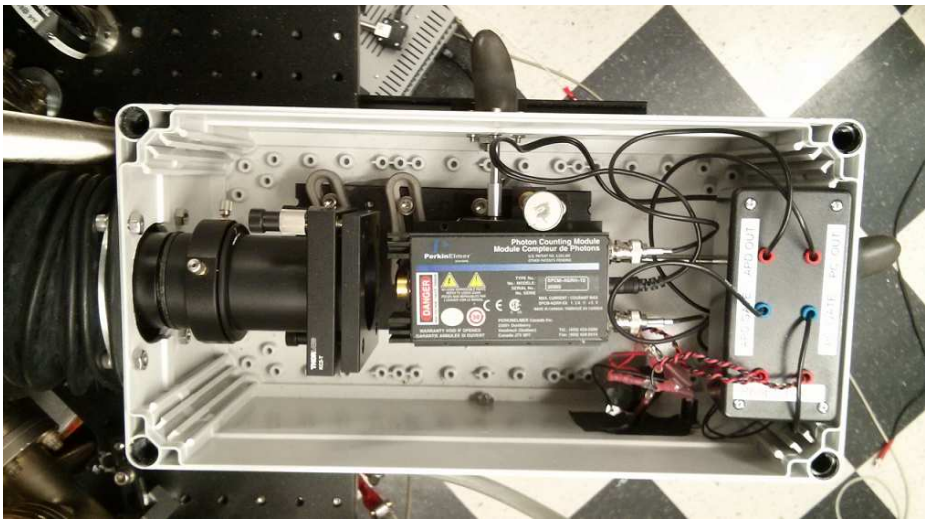

Figure 6.4: Photo of the single atom detection system.

For the alignment of the MOT and the optics, a CMOS camera (ThorLabs DCC1545M) is located at the position of the APD and observes the MOT through the optics. Once we find a good MOT image from the CMOS camera, the camera is replaced with the APD and the box is closed for the APD single atom detection. If all the signals are focused and detected ideally, the CMOS camera image is expected to be ∼10 times brighter than the CCD camera image by considering the solid angles. In reality, we see a factor of ∼4 when the system alignment is good. Figure 6.5 shows images taken by the CMOS camera with the single lens objective and the triple lenses objective. One can clearly see that the latter produces much better focusing.

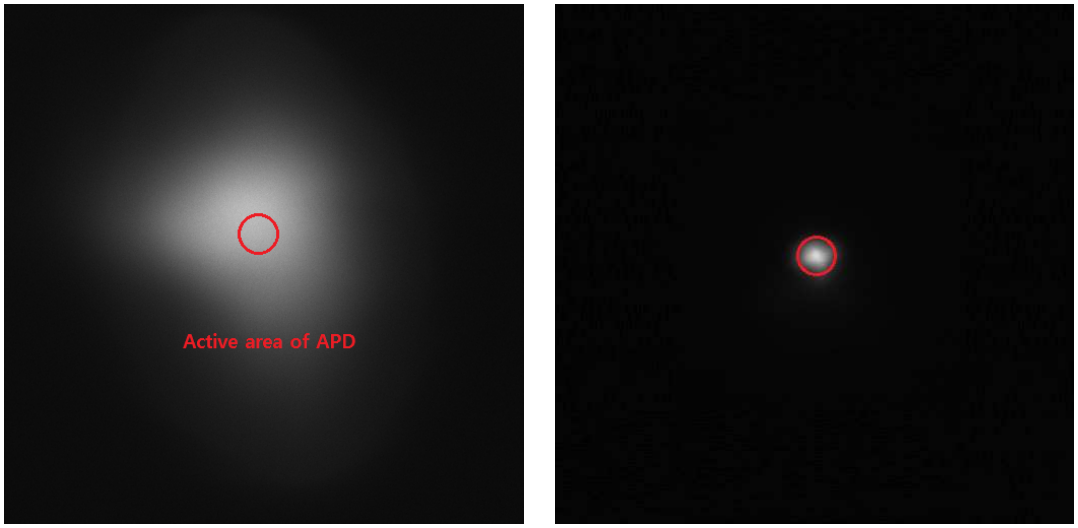

Figure 6.5: MOT image taken at the position of the APD with a single in-vacuum lens (left) and triple in-vacuum lenses (right). The red circles indicate the active area of the APD (diameter of 180 μm). The brightness of the two images is not to scale.

6.3 Background noise

In the APD signal, the background fluctuation is the major obstacle to discriminating single atoms as shown in Fig. 6.6. We measured the background signal from each potential source with argon gas to study the properties of the background (Tab. 6.2). The actual values vary depending on the laser properties and the discharge source behavior at the time of operation, but the largest contribution is always due to laser reflections inside the chamber. Next, fluorescence from the argon beam produces ~20% of the background, and this will automatically vanish for the krypton measurement in a xenon sample due to the very small fraction of krypton in the xenon gas.

There are two ways to remove the background fluctuation: suppressing the background itself and stabilizing the fluctuation. The former approach is achieved by the bandpass filter and the iris mentioned in Sec. 6.2. Regarding the latter approach, stabilizing the intensity of the MOT laser can reduce the background fluctuation because the reflected laser makes the largest contribution to the background.

The laser intensity was measured versus time at several locations to study fluctuations

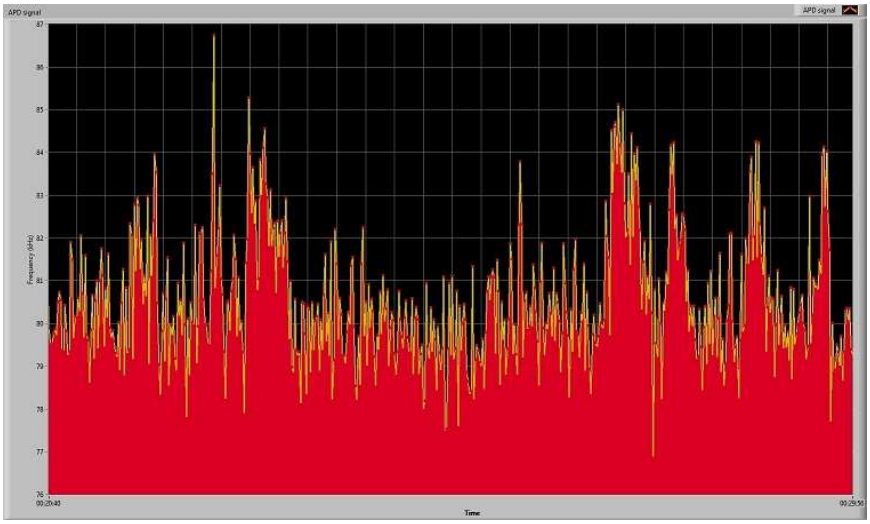

Figure 6.6: Single atom signals captured by the APD with a high background fluctuation. Our signals are ∼5 kHz high, but fluctuation of the background noise makes it difficult to discriminate each atom.

Table 6.2: Contribution of each component to the background noise in APD measurements with argon gas.

Background source	Signal size [kHz]	Relative size [%]
Dark count	0.3	1.4
Ambient light	1.1	5.0
Laser scattering	16.6	75.5
Atomic beam fluorescence	4.0	18.2
Total	22.0	100

and decide how to reduce them (Fig. 6.7). The external cavity diode laser (ECDL) is quite stable, and the tapered amplifier introduces a small amount of fluctuation. The fiber optic after the amplifier generates fluctuations of a ∼2% magnitude, and these fluctuations remain in the MOT laser. The root mean square fluctuations of each data trace are 0.084×10^{-3}, 1.2×10^{-3}, 7.5×10^{-3}, and 7.8×10^{-3}, respectively.

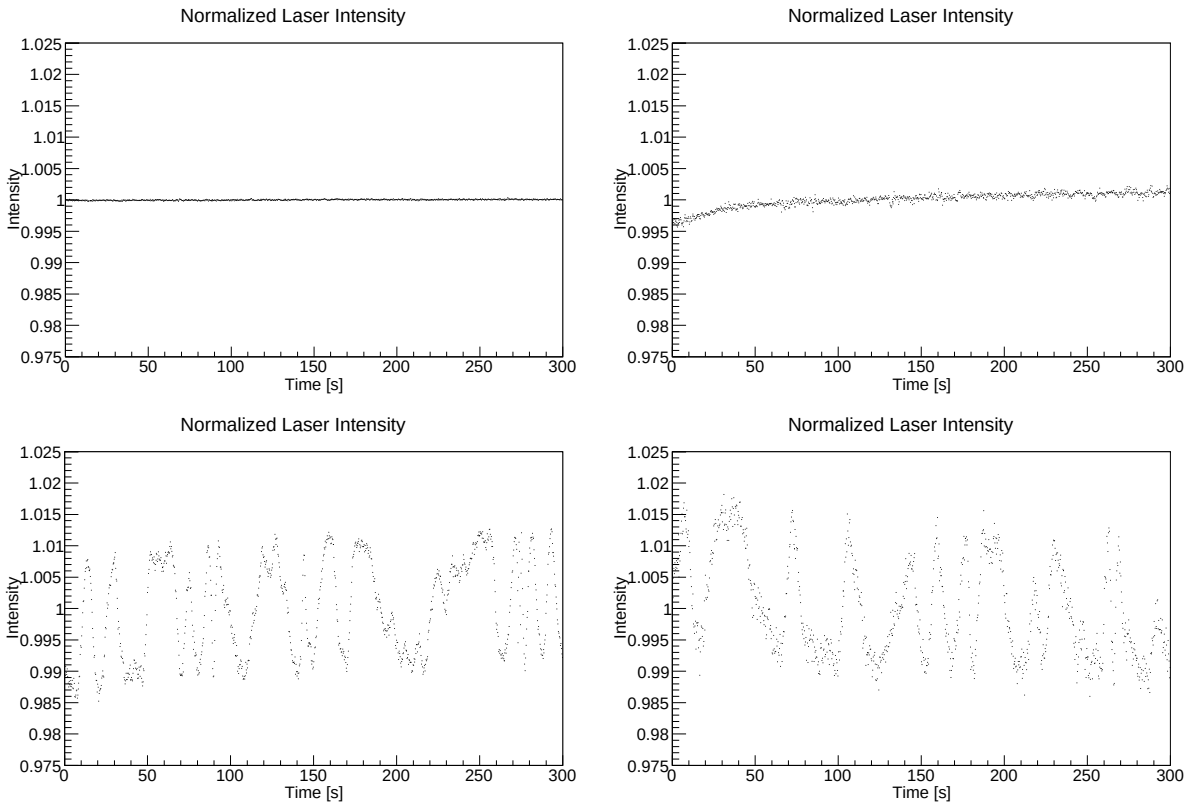

Figure 6.7: Laser intensity measurements at several locations. All data traces are normalized to the average intensity. The data are taken directly after the diode laser (top, left), after the amplifier (top, right), after the fiber optic cable (bottom, left), and after passing through the chamber (bottom, right)

6.3.1 Light intensity locking PID controller

We employ a custom-made proportional-integral-derivative (PID) controller to stabilize the MOT laser intensity [Meyrath, 2005]. A small fraction of the MOT laser light is split off before the expansion and used for intensity locking. The PID controller consists of three subcircuits containing an operational amplifier (Fig. 6.8). In the first subcircuit, a photodiode produces a voltage corresponding to the incoming laser power and a BNC input defines the set point to which the light should be stabilized. The second subcircuit is the actual PID loop which generates the control signal, and the third subcircuit ensures that the output of the circuit has the correct sign.

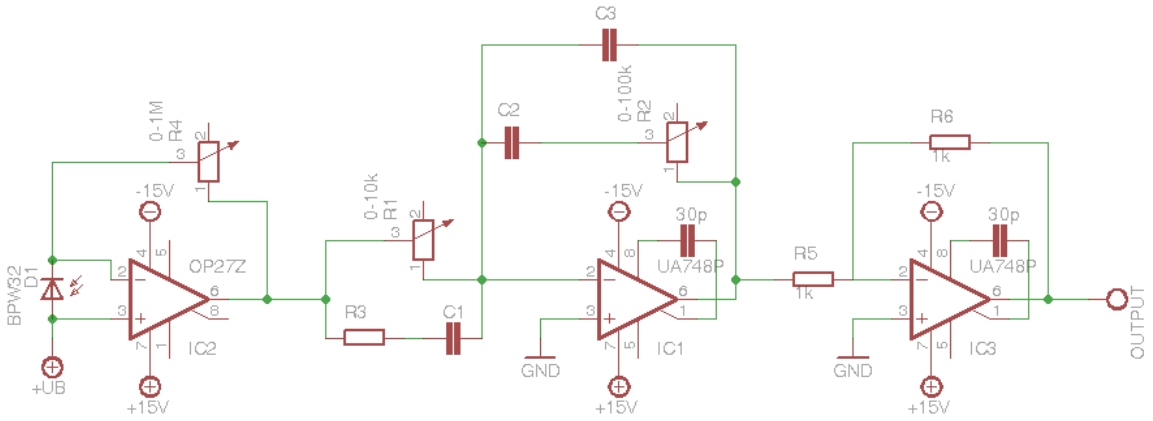

Figure 6.8: Schematic of the intensity locking proportional-integral-derivative (PID) circuit.

The controller output is expressed in the form of

$$\begin{aligned} u(t) &= K_p\, e(t) + K_i \int_0^t e(\tau)\mathrm{d}\tau + K_d \frac{\mathrm{d}}{\mathrm{d}t} e(t) \\ &\equiv K_p \left[e(t) + \frac{1}{T_i} \int_0^t e(\tau)\mathrm{d}\tau + T_d \frac{\mathrm{d}}{\mathrm{d}t} e(t) \right], \end{aligned} \tag{6.1}$$

where K_p is the proportional gain, K_i is the integral gain, K_d is the derivative gain, T_i is the integration time constant, T_d is the derivative time constant, and e is the error (defined as the set point minus the process value). In our circuit design, the above parameters are

determined as

$$K_p = \frac{R_2}{R_1},$$
$$T_i = R_1 C_2,$$
$$T_d = R_2 C_1. \tag{6.2}$$

The output signal is used as control of an attenuator which determines the power of the drive signal to the acousto-optic modulator (AOM) and consequently the output frequency-shifted laser power.

The ideal values of each component in the circuit are predicted by the Ziegler-Nichols method [Ziegler and Nichols, 1942]. We tested the controller with several sets of parameters near the theoretically predicted values and found the proper set of components. For the test of the PID controller, we measured the intensity of the MOT laser beam with and without the controller working. Figure 6.9 shows the measured intensities with a normalized scale. The amplitude fluctuation decreases from ∼2% to less than 0.5% by using the PID controller. There are still fluctuations on a short time scale, but fluctuations on a long time scale (∼10 s) are mostly removed.

6.3.2 Background fluctuation

Despite the PID controller performance, the APD signal still contains significant fluctuations. An APD measurement of laser scattering shows properties of the background signal. We assume the following in this measurement. If the background is from instability of the laser intensity, the background fluctuation should be proportional to the background size. In other words,

$$\sigma(N) = A \times N, \tag{6.3}$$

where N is the number of photons and A is a coefficient. On the other hand, if the background is from shot noise, which is a statistical fluctuation of random photon arrival times, the background fluctuation follows Poisson the distribution,

$$\sigma(N) = \sqrt{N}. \tag{6.4}$$

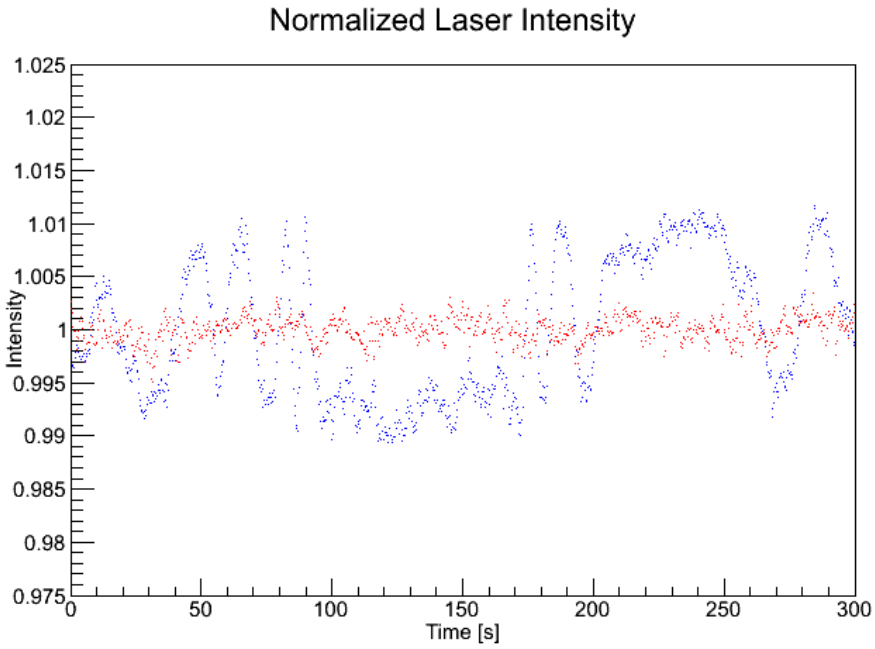

Figure 6.9: Relative laser intensity with and without the PID intensity locking box. The blue dots are the data without the PID controller, and the red dots are taken with the PID controller.

In the measurement, we adjusted the MOT laser power so that the magnitude of each APD signal is 1×10^4/s, 2×10^4/s, or 3×10^4/s at a 300 ms APD integration time. Here, the unit implies the number of detected photons per second. The photon counts were measured for five minutes in each case and the standard deviations were derived. The actual number of photons detected in a single measurement can be expressed as the measured signal times the integration time. For example, with an APD signal of 1×10^4/s at 300 ms, the actual counted number of photons is $N = 1 \times 10^4/\text{s} \times 300\ \text{ms} = 3 \times 10^3$.

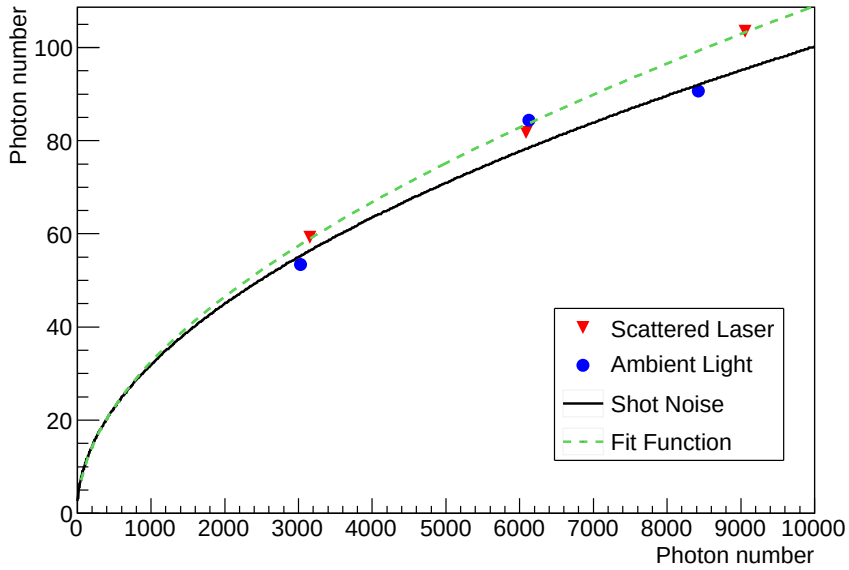

Figure 6.10: Standard deviation of background noise. The black solid line shows shot noise $\sigma(N) = \sqrt{N}$, and red triangles and the blue circles show the standard deviation of the measured background noise from scattered lasers and ambient light, respectively.

Figure 6.10 shows the derived standard deviations in the function of the number of detected photons. The APD signal from ambient light was also measured and processed for comparison. The black solid line in the plot indicates the shot noise level (Eq. 6.4). The standard deviation of the signal from ambient light very well agree with the shot noise curve. The data from laser scattering are also close to the curve, but show a small gap as the photon number increases. The data can be described by an equation $\sigma(N) = \sqrt{N} + 0.00089 \times N$,

which is shown as a green dashed line. This implies that the background fluctuation is mostly from shot noise with a small fraction coming from instability of the laser intensity. In this case, it is not possible to remove the fluctuation by stabilizing the laser intensity since shot noise is inevitable at a given background level. Thus, we are required to reduce the size of the background itself to lower its fluctuation.

For this purpose, we employ another laser operation mode for detection, which is different from the mode used for trapping [Du, 2003]. The detection mode is characterized by a small laser beam size and a low intensity compared to the trapping mode laser. During the transition from the trapping to the detection mode, the size of the background from the reflected laser decreases proportionally to the MOT laser intensity, while the fluorescence rate decreases by a relatively small amount (∼25%). As a result, the background noise is reduced significantly with a comparable signal size. The two laser modes must be switched rapidly to detect single atoms with a high loading rate during a measurement. The characteristics of the two laser modes are summarized in Tab. 6.3. The switching has not yet been attempted because the measurements described below indicate that the detection mode produces a higher loading efficiency for krypton atoms in xenon gas (Sec. 7.5.1).

Table 6.3: Comparison of the laser modes for trapping and detecting.

	Trapping laser	Detecting laser
Beam diameter [cm]	3	1
Beam intensity [mW/cm^2]	2×(8+8+16) [a]	2×(2+2+8) [a]
Total beam power [mW]	452	13
Scattering rate [s^{-1}] [b]	1.57×10^7	1.18×10^7

[a] The values in parentheses are beam intensities of lasers in the x, y, and z directions.

[b] At a detuning of -5.95 MHz, both argon and krypton have the same scattering rates.

6.4 Single atom signal

The integration time of the APD is also an important factor in determining the signal shape. At a short integration times, the number of detected photons N in the measurement process

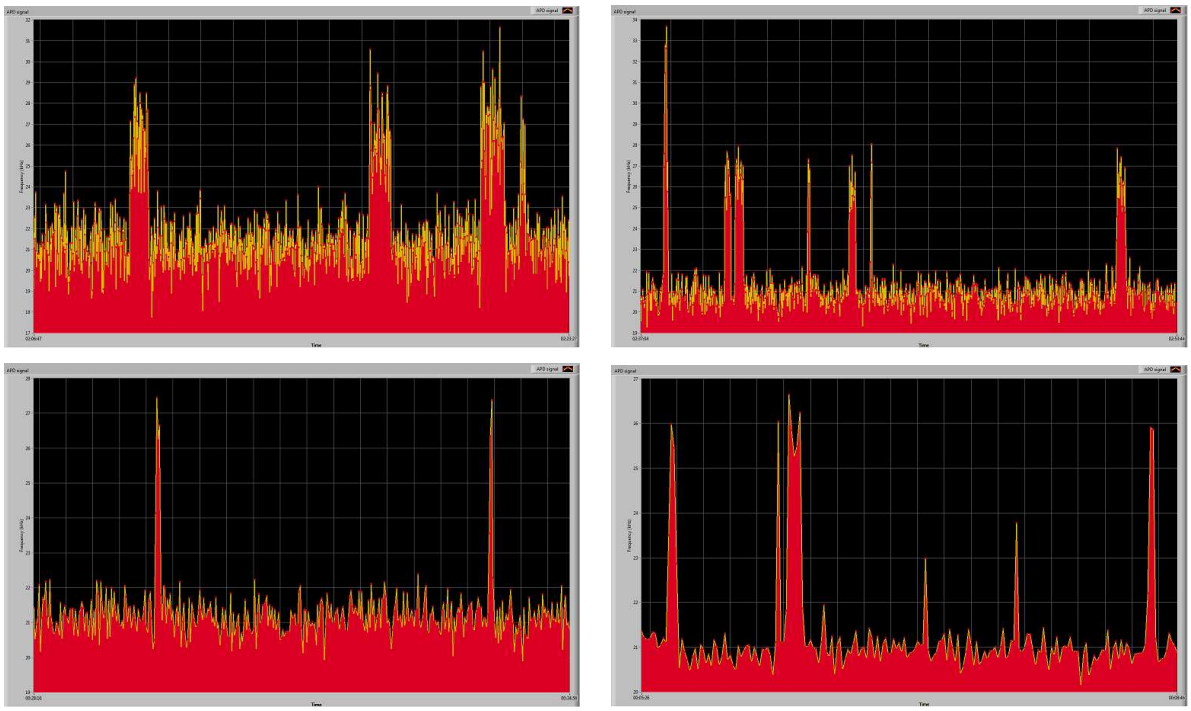

Figure 6.11: Single atom signals measured by the APD with several different integration times: 20 ms (top, left), 70 ms (top, right), 100 ms (bottom, left), and 300 ms (bottom, right). Single atom signals have good resolution in the cases of 70 ms and 100 ms.

is small, which leads to a low signal to noise ratio (SNR) (Fig. 6.11 (top, left)) expressed as

$$\mathrm{SNR} = \frac{N}{\Delta N} \simeq \frac{N}{\sqrt{N}} = \sqrt{N}. \tag{6.5}$$

On the other hand, there is an advantage that the APD can detect atoms that decay shortly after they are trapped. As the integration time increases, more photons are detected during the measurement time, which results in a better SNR. However, there is a higher possibility that an atom escapes the trap within the integration time. This will lead to a smaller signal size, and consequently make single atom discrimination ambiguous (Fig. 6.11 (bottom, right)). The measurements shown in Fig. 6.11 indicate that the APD signal is optimal for integration times of $\sim 70 - 100$ ms.

For the measurement of single argon atoms, we used the detection mode and set the APD integration time to 20 ms. All transverse cooling beams were switched off and only

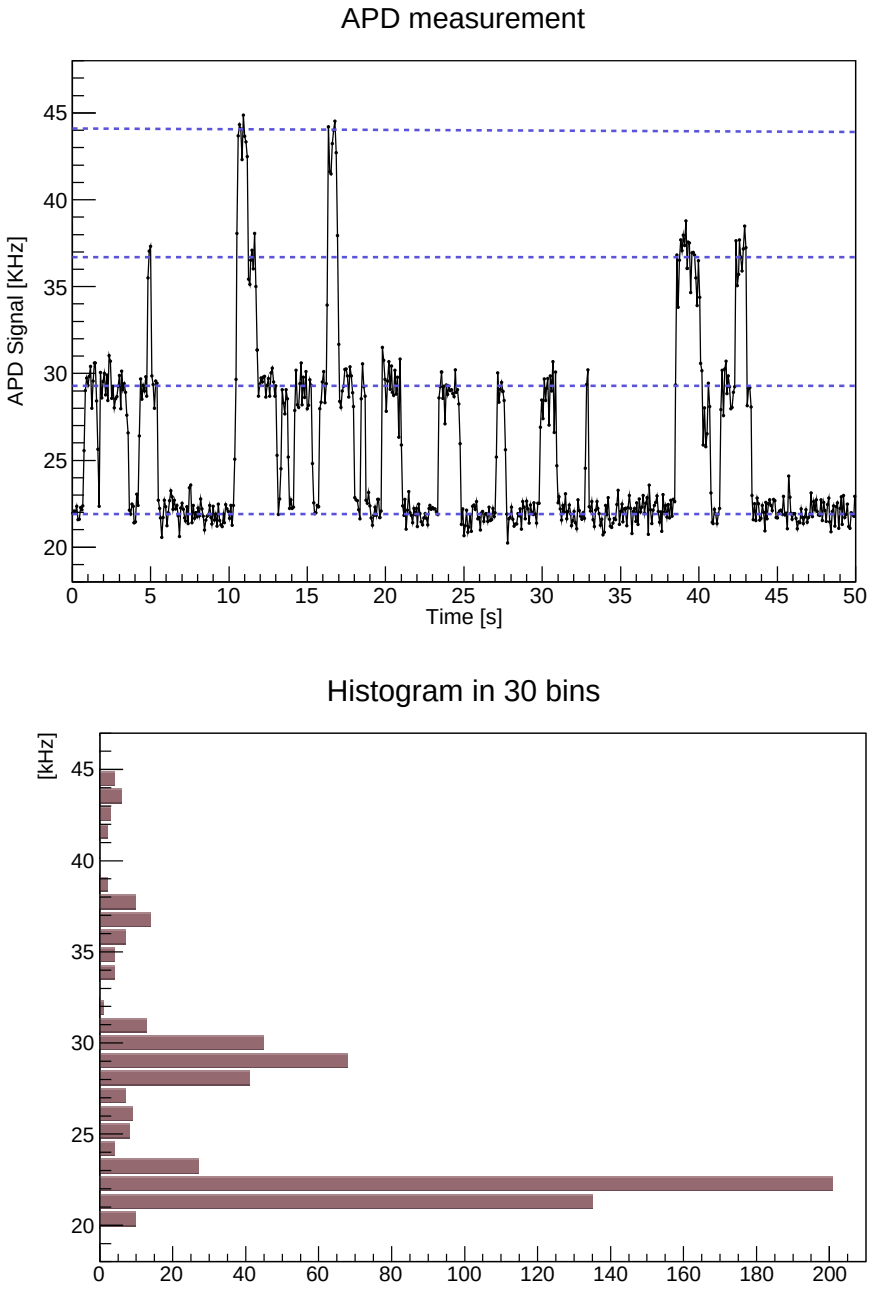

Figure 6.12: Single argon atom signals measured by the APD (top). The dashed lines indicate the values 2.20×10^4 /s , 2.93×10^4 /s, 3.66×10^4 /s, and 4.39×10^4 /s. The histogram of these data shows peaks for the background, one atom, two atoms, and three atoms (bottom).

a small fraction of the Zeeman slower light was used, to reduce the loading rate enough to see single atoms. Figure 6.12 (top) shows the single argon atom signals measured for 50 seconds. In this plot, data for nearby four points are averaged to give the best signal shape, which results in the same conditions as the integration time of 80 ms. One, two, and three atoms are clearly distinguishable. The background level is 2.2×10^4 photons/s, and a single atom signal is 7.3×10^4 photons/s. This is also represented in a histogram (Fig. 6.12 (bottom)), where the measured data are classified into 30 bins. Since it is not likely that two atoms are trapped at the same time or in a quick succession for the krypton measurement in a real xenon sample, single atom discrimination should be more straightforward.

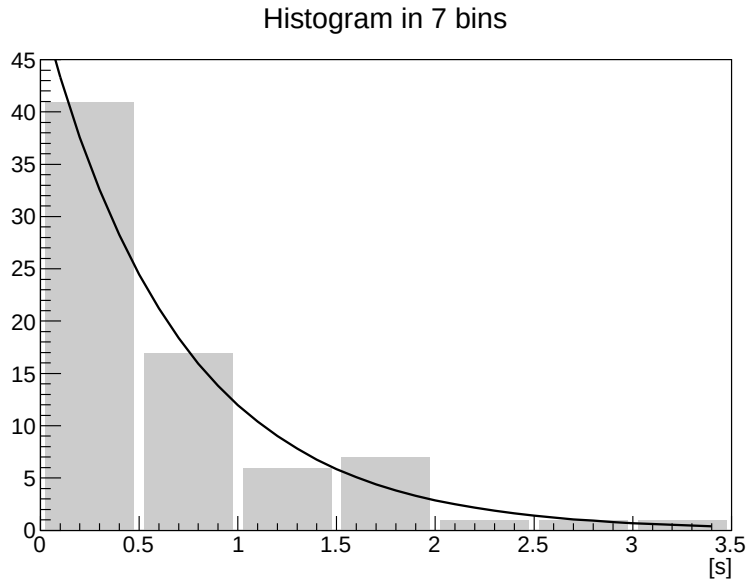

Figure 6.13: Histogram of lifetimes of 74 trapped argon atoms. The black line is the graph of the decay rate, $-\mathrm{d}N/\mathrm{d}t = (35/0.7\ \mathrm{s})\ e^{-t/0.7\mathrm{s}}$. The value of $N_0 = 35$ is determined by fitting the data.

Additionally, the mean lifetime of trapped atoms is derived from the single atom signals. The trapped atoms decay according to the relation

$$N(t) = N_0\ e^{-t/\tau}, \tag{6.6}$$

where τ is the mean trap lifetime. This is valid when only one atom is trapped at a time, i.e., when there are no interatomic collisions. We directly measured the lifetimes of 74 single

atoms and obtained the mean value of $\tau \sim 0.7$ s. The reason for the difference from 0.47 s, which is derived in Sec. 5.5, is that the vacuum level in the MOT chamber was slightly higher than usual at this time. From Eq. 6.6, the decay rate is

$$-\frac{\mathrm{d}N}{\mathrm{d}t} = \frac{N_0}{\tau}\, e^{-t/\tau}. \tag{6.7}$$

The measured data in a histogram roughly agree with the predicted exponential decay rate (Fig. 6.13).

Chapter 7

Krypton abundance measurement

As discussed in Ch. 5, we achieved the required loading rate to detect argon atom trace at a 1-ppt level. We also confirmed the system resolution to discriminate single atoms in Ch. 6. To measure the krypton contamination in xenon samples, we also need to know the precise trapping efficiency of the system for krypton in xenon. We prepare Kr-Xe mixtures with known krypton concentration levels, and calibrate the system efficiency, as described in this chapter.

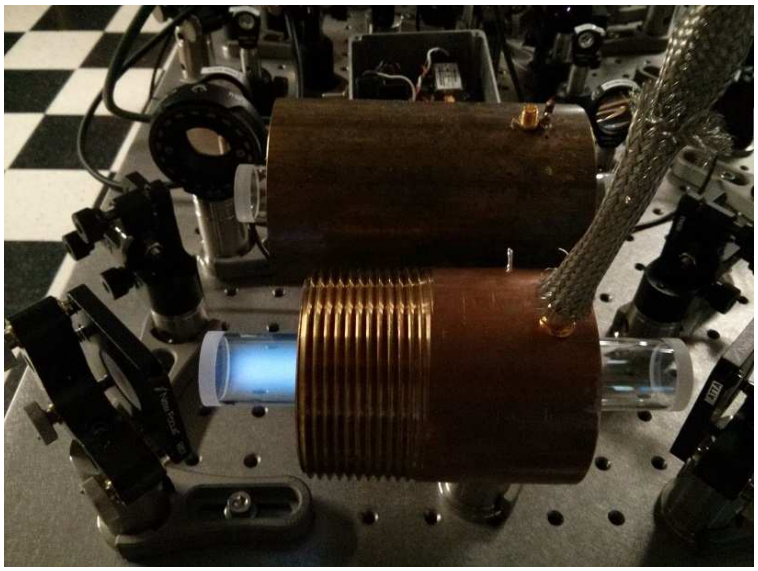

Figure 7.1: Helical coil resonators for the argon vapor cell and the krypton vapor cell. The krypton vapor cell lights on in this picture.

The system can be switched from argon trapping to krypton trapping by simply changing the trapping laser wavelength by locking to a krypton reference cell. In the laser stabilization system, two helical coil resonators, installed in parallel, contain a krypton vapor cell and an argon vapor cell. We can select the paths of the probe and pump beams using flipping mirror mounts. The angle of the grating inside the external cavity diode laser (ECDL) is carefully adjusted with three knobs on its mount to set the wavelength range of the output laser suitable for each transition, and the input current to the diode laser is slightly adjusted so that the laser output is mode-hop free. As the krypton vapor cell discharge is driven at a 70 MHz frequency (60 MHz for the argon cell), the frequency of the driving signal is adjusted before connecting to the krypton resonator. Now the laser locks to the frequency that is 80 MHz red-detuned from the resonant frequency of the krypton transition ($\lambda_0 =$ 811.5132 nm).

7.1 Measurement of krypton in argon gas

As a commissioning run of the krypton trap, we first tested the argon gas that has been used for system adjustment. The single atom detection system was aligned using argon MOT, then the locking frequency was changed to the krypton transition as explained above. The detection mode was used for both trapping and detection in this measurement, which means the loading efficiency is 1/20 of the maximum. During the measurement, the pressure in the source chamber was maintained at 0.8 mtorr, corresponding to the consumption rate of 8×10^{16}/s (Sec. 5.2).

We detected 13 trapped atoms in the APD signal during a 35 minute measurement, obtaining the loading rate of 6.2×10^{-3} atoms/s. The trapping efficiency of the system for krypton in argon gas has not been directly investigated. If we assume that the efficiency for krypton in argon is same as that for argon, the krypton contamination is estimated from the previously measured loading rate of the argon MOT and the above data by

$$\begin{aligned} L_{\mathrm{Kr}} &= 1.79 \times 10^8/\mathrm{s} \times 2.1 \times \frac{1}{20} \times 0.57 \times \frac{\mathrm{Kr}}{\mathrm{Ar}} \\ &= 6.2 \times 10^{-3}/\mathrm{s}, \end{aligned} \tag{7.1}$$

where 1.79×10^8/s is the loading rate of argon MOT, 2.1 is the predicted capture ratio

enhancement of our Zeeman slower for krypton, 1/20 is the efficiency decrease due to using the trapping mode, and 0.57 is the isotopic abundance of ^{84}Kr. Solving Eq. 7.1 gives the krypton concentration in the argon gas of 5.8×10^{-10} (580 ppt).

If the measured trapping efficiency of the system for krypton in xenon (discussed in Sec. 7.5) is assumed in this case, the estimated krypton concentration level, Kr/Ar, is 15 ppt. In order to derive the precise value of Kr/Ar, we need to measure the trapping efficiency of the system for krypton in argon gas using Kr-Ar mixtures with known ratios, as we do for krypton in xenon gas. Since the purpose of this project is to determine krypton level in xenon gas, not in argon, further investigations of the accurate Kr/Ar value have not been carried out. This measurement does confirm that our ATTA system works properly in the sense of its ability to trap trace atoms in a noble gas sample and count single atoms.

7.2 Consumption rate of xenon gas

Prior to trapping krypton atoms in xenon gas, we measured the consumption rate of xenon gas at source pressures of 0.2 mtorr to 0.8 mtorr, where the xenon discharge is active, in the same way as discussed in Sec. 5.3. The measured consumption rates are presented in Tab. 7.1, and plotted in Fig. 7.2. The consumption rate of xenon is about 30 % lower than that of argon gas at the same source pressure, which is explained by the larger mass of xenon atoms. According to the Maxwell-Boltzmann distribution for a three dimensional gas, xenon has the most probable velocity of 193 m/s at the room temperature, while argon has 349 m/s.

Table 7.1: Consumption rates of krypton gas for different pressures in the source chamber.

Source chamber pressure [mtorr]	0.20	0.50	0.61	0.71	0.80
Consumption rate [10^{16} s^{-1}]	1.8	3.6	4.1	4.7	5.5

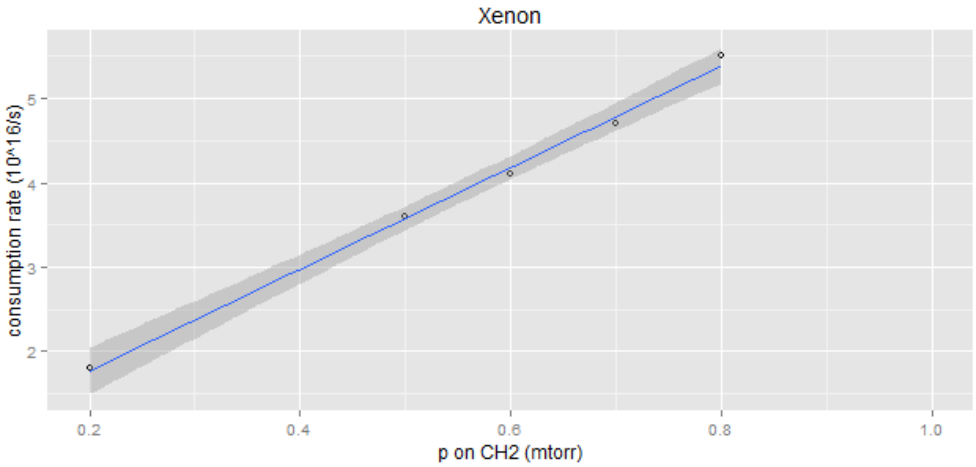

Figure 7.2: Consumption rates of xenon gas for different pressures in the source chamber. The consumption rate increases linearly with the source chamber pressure.

7.3 Source efficiency versus pressure

The fraction of atoms that are excited by the source discharge is sensitive to the source pressure, but it is difficult to predict the behavior theoretically. Table 7.2 presents the relative source efficiency as a function of gas pressure, inferred from the number of atoms detected by the APD. It is also plotted in Fig. 7.3. We find no clear relation between the efficiency and the source pressure, but the measured data are repeatable and reliable.

Table 7.2: Relative source efficiency for krypton in xenon gas as a function of the source pressure at a -20 dBm RF power.

Source pressure [mtorr]	0.10	0.15	0.20	0.25	0.31	0.35
Relative intensity	27	61	55	73	77	100
Source pressure [mtorr]	0.41	0.45	0.51	0.56	0.62	
Relative intensity	70	68	66	64	50	

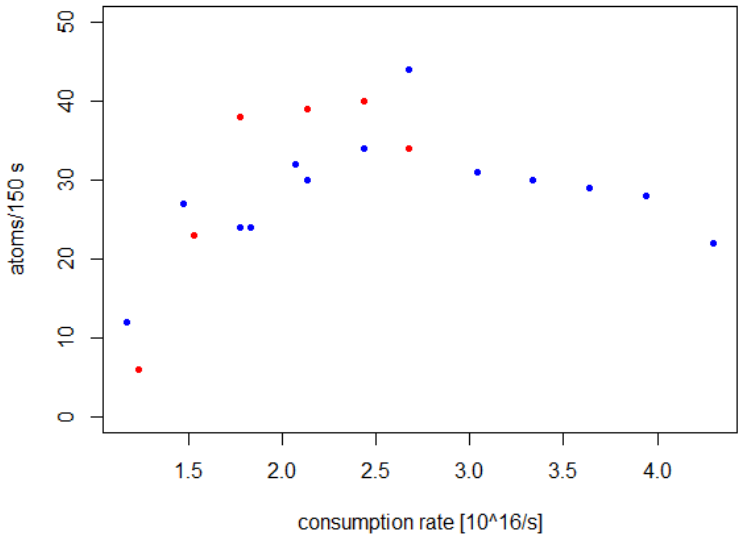

Figure 7.3: Relative source efficiency for krypton in xenon gas in the function of the source pressure. Blue circles are data at a −20 dBm RF power, and red circles are data at a −14 dBm RF power.

7.4 Xenon gas with high krypton contamination

A bottle of xenon gas from the XENON group at Nevis Laboratory of Columbia University was first used for the measurement of the system efficiency for krypton in xenon gas. It turned out to be unusable for calibration due to its high krypton level. Then another xenon bottle was tested and it also showed too high a krypton concentration. Although the measurements with these two bottles of xenon gas do not give us an accurate system efficiency, they are still useful in cross-checking our calibration of the krypton concentration. This section briefly reviews the results from these measurements.

7.4.1 Xenon bottle 1

In this test, we used a bottle of xenon gas that originated from the distillation column at Nevis Laboratory. Since the history of the bottle was not tracked carefully, there was no information about its krypton level. Roughly, a ppm krypton contamination was expected before the trial. The source pressure was maintained at 0.20 mtorr, leading to a gas con-

sumption rate of 1.8×10^{16}/s (Tab. 7.1). Operation with this xenon gas produced a large number of trapped atoms, sufficient to form a MOT visible by a CCD camera, indicating that the xenon bottle contains much more krypton than we expected. Calibration through single atom detection is still possible by controlling the loading rate by a known factor, but it involves a higher uncertainty in case of such a large loading rate.

In the image of the CCD camera, the brightness of the krypton MOT is 1/10 of that of an argon MOT produced at the same setting. This ratio can be interpreted as a ratio of loading rates for a large number of trapped atoms according to Eq. 5.17. $\sim$1 % of difference in scattering rates between krypton and argon is ignored here. Using the system efficiency for krypton in xenon, determined in Sec. 7.5, the krypton concentration level in the xenon gas is estimated by

$$\frac{1}{10} = 2.1 \times 16.2 \times 0.55 \times 0.57 \times \frac{\mathrm{Kr}}{\mathrm{Xe}}, \tag{7.2}$$

where 1/10 is the ratio of the measured krypton loading rate compared to the argon loading rate, 2.1 is the capture ratio enhancement for the Zeeman slower for krypton compared to argon, 16.2 is the enhancement of the source efficiency for krypton at the source pressure of 0.35 mtorr, 0.55 is the ratio of source efficiency between 0.20 mtorr and 0.35 mtorr, and 0.57 is the isotopic abundance of ^{84}Kr. Equation 7.2 yields

$$\frac{\mathrm{Kr}}{\mathrm{Xe}} = 9.3 \times 10^{-3}. \tag{7.3}$$

This krypton level greatly exceeds our expectation.

Table 7.3: Mass components in the first bottle of xenon gas analyzed by the RGA.

Mass	1	2	14	16	17	18	28	44	64-68
Portion [%]	0.72	0.48	2.76	0.48	0.96	5.40	31.89	0.12	11.15
Mass	84	128	129	130	131	132	134	136	Total
Portion [%]	0.96	0.72	11.96	1.68	9.59	12.23	4.68	4.20	100.0

A residual gas analyzer (RGA) monitored the masses of the gas components in the MOT chamber to verify the estimate in Eq. 7.3. The mass distribution was measured with and without the gas flow into the system, and the background was subtracted. The

long distances and the vacuum pumps between the reservoir and the RGA may introduce some errors to the data. Masses between 128 to 135 are xenon isotopes, and the masses of 64-68 indicate the xenon cracks in Tab. 7.4. The RGA data show that the gas inside the bottle consists of 56% xenon, 32% molecular nitrogen, 5% water, 1% ^{84}Kr, and other traces, which means much higher impurities than expected. Although the RGA did not find other krypton isotopes due to their low abundances, the krypton level in the bottle is derived to 1.7% according to the natural abundance of ^{84}Kr. This is close to the estimated value from the MOT brightness, 0.93%. The difference can arise from the uncertainty of the RGA measurement or from different source efficiencies for xenon gas containing impurities such as nitrogen and water.

7.4.2 Xenon bottle 2

Since the xenon bottle in Sec. 7.4.1 was not suitable for single atom detection, we obtained another bottle of xenon from Nevis Laboratory, used for cold trap experiment in the XENON group. The test was done at a 0.45 mtorr source pressure, corresponding to a gas consumption rate of 1.8×10^{16}/s (Tab. 7.1). This time, a visible krypton MOT was formed again, with a lower intensity. The loading rate of the krypton MOT is estimated to be 0.006 times that of argon MOT from our argon gas. The krypton level in the xenon bottle is calculated in the same way as in Sec. 7.4.1,

$$0.006 = 2.1 \times 16.2 \times 0.68 \times 0.57 \times \frac{\mathrm{Kr}}{\mathrm{Xe}}, \tag{7.4}$$

where 0.006 is the ratio of the measured krypton loading rate to the argon loading rate, 2.1 is the capture ratio enhancement for the Zeeman slower for krypton compared to argon, 16.2 is the enhancement of the source efficiency for krypton at the source pressure of 0.35 mtorr, 0.68 is the ratio of source efficiency between 0.45 mtorr and 0.35 mtorr, and 0.57 is the isotopic abundance of ^{84}Kr. From Eq. 7.4, Kr/Xe is calculated to be

$$\frac{\mathrm{Kr}}{\mathrm{Xe}} = 4.6 \times 10^{-4}, \tag{7.5}$$

i.e., 460 ppm.

The RGA was again used to analyze the masses of the gas components in the gas bottle (Tab. 7.4). Xenon makes up 46%, and water 30% of the gas. The RGA data do not show

Table 7.4: Mass components in the second bottle of xenon gas analyzed by the RGA.

Mass	2	17	18	28	32	
Portion [%]	5.52	8.29	29.83	4.42	2.21	
Mass	44	64-68	129	131	132	Sum
Portion [%]	3.87	14.37	12.71	7.73	11.05	100.0

any components at the mass of krypton, which makes sense since the estimated krypton level, 4.6×10^{-4}, is too small for RGA scanning. For system calibration via single atom detection, xenon gas less contaminated by krypton is required.

7.5 Calibration for krypton in xenon studies

After trials in Sec. 7.4, we purchased a bottle of commercial xenon gas (PraxAir) for calibration of the system efficiency for krypton in xenon. The company guarantees the minimum purity of xenon above 99.999 % and the krypton concentration at ∼10 ppb. Table 7.5 shows impurity levels specified in the certificate of analysis. Pure krypton gas used to make Kr-Xe mixtures is from Spectra Gases Inc.

Table 7.5: Specified impurity levels of the xenon bottle from PraxAir.

Components	Oxygen	Nitrogen	THC	Water	CO_2	Krypton	Ar, H_2
Concentration [ppb]	100	440	100	100	100	10	400

The gas mixing system consists of a 201 cm^3 chamber where krypton gas is filled and a 221 cm^3 reservoir where krypton and xenon gases are mixed (Figure. 7.4). Including the volume of connections to each of them, the confinement volumes of the krypton chamber and the mixing region are 260 cm^3 and 766 cm^3, respectively. To prepare Kr-Xe mixtures at arbitrary concentrations, all connections to the krypton chamber, except for one to the krypton gas bottle, are closed, and krypton gas is introduced at a low pressure. The pressure of the krypton gas is monitored by a capacitive manometer (Pfeiffer Vacuum CMR 365) connected to the krypton chamber. Then the connection to the krypton bottle is closed and

the remaining krypton gas outside the krypton chamber is pumped out through a bypassing pipe. Once the pressure is close to the asymptotic limit, the xenon gas bottle and the valve between the reservoir and the krypton chamber are opened, and the krypton and xenon gases are mixed by dispersion. A pressure transducer is used to read the pressure in the gas mixing region.

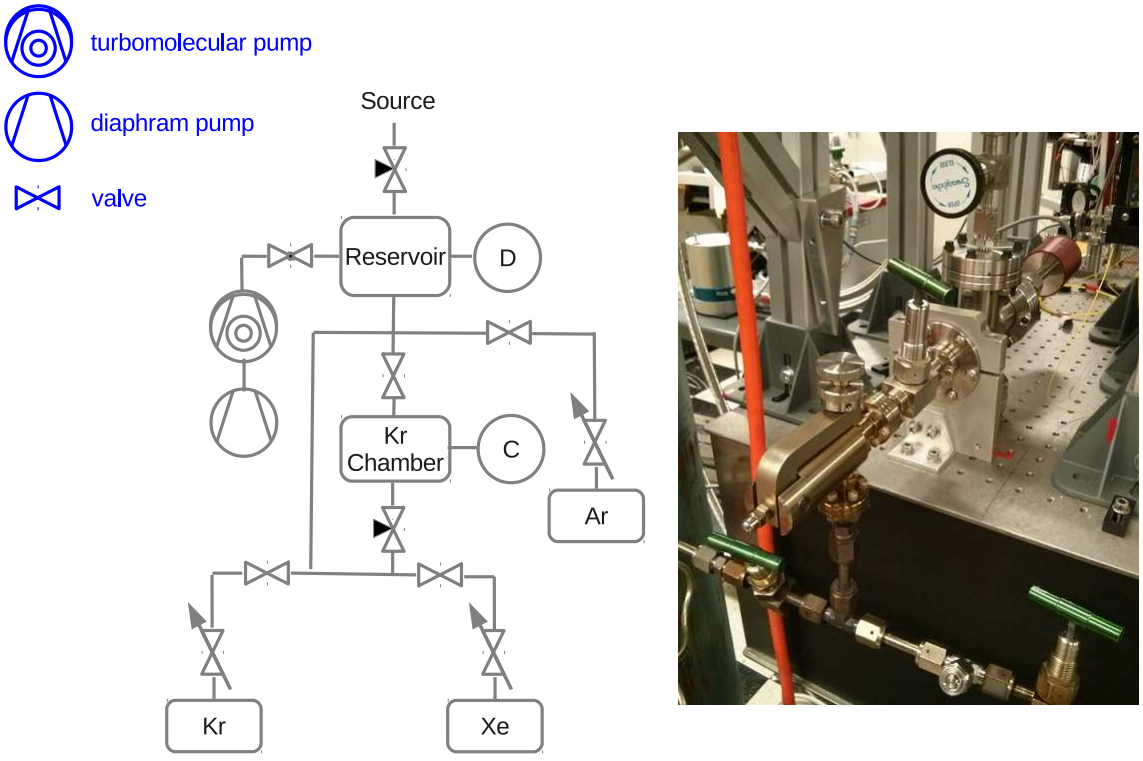

Figure 7.4: Schematic of the gas inlet system and image of the krypton chamber and its connections. Krypton gas in the small krypton chamber is mixed with xenon gas in the reservoir. A pressure transducer (D) and a capacitive manometer (C) monitor the pressure in the reservoir and in the mixing volume, respectively (left). A fine leak valve controls the amount of krypton gas in the krypton chamber (right).

In this section, we determine the trapping efficiency of our system for krypton in xenon gas, based on single atom measurement with two different Kr-Xe mixtures. This is the last test required prior to measuring krypton contamination in xenon samples. Additionally, the krypton level in the xenon gas from PraxAir is estimated from these measurements.

7.5.1 Pure xenon gas from PraxAir

Before measurements with Kr-Xe mixtures, the pure xenon gas from PraxAir was tested. At the time of this measurement, the loading rate measured with argon MOT was half of the maximum. Additionally, all transverse cooling stages were switched off to reduce the loading rate, since a ppb level of krypton is expected to generate too many trapped atoms. The source was maintained at a 0.20 mtorr pressure, corresponding to the consumption rate of 1.8×10^{16}/s.

The APD detected 52 trapped atoms in 20 minutes, leading to the loading rate of 4.3×10^{-2}/s. By adjusting this number to the optimized setting of our system, we have the loading rate

$$L_{\text{PraxAir}} = 4.3 \times 10^{-2}/\text{s} \times 2 \times 12 \times \frac{1}{0.55} = 1.88/\text{s} \ (^{+25\%}_{-22\%}), \tag{7.6}$$

where 4.3×10^{-2}/s is the measured loading rate, 2 is from the non-optimized loading rate at the time of the measurement with an uncertainty of $\pm 3\%$, 12 is the transverse cooling enhancement factor with an uncertainty of $\pm 5\%$, and 1/0.55 is the ratio of source efficiency between 0.20 mtorr and 0.35 mtorr with an uncertainty of $\pm 10\%$.

7.5.2 12 ppm krypton mixture

The krypton chamber was filled with krypton gas at 2.2 mtorr, then mixed with xenon gas at 15.4 torr in the mixing region, leading to a 12 ppm ($\pm 5\%$) Kr/Xe level estimated from the specified volumes of each region. The source was operated at the pressure of 0.2 mtorr, i.e., the consumption rate of 1.8×10^{16}/s. For single atom detection, the loading rate needs to be reduced by a known amount for the reason discussed in Sec. 7.5.1. For this purpose, the Zeeman slower laser was partially blocked with a small aperture, and all transverse cooling stages were blocked. Additionally, one transverse cooling laser was used in a one way configuration to push the atomic beam.

The time taken to find 100 single atoms from the APD signal was measured to be 147 seconds, which is equivalent to 0.68 atoms/s. By compensating for the efficiency decrease

mentioned above, the loading rate for a 12 ppm Kr/Xe gas is estimated as

$$\begin{aligned} L_{12\text{ppm Kr}} &= 0.68 \text{ /s} \times \frac{1}{0.3} \times 12 \times \frac{3}{2} \times \frac{1}{0.03} \times \frac{1}{0.55} \\ &= 2.47 \times 10^3 \text{ /s } (^{+32\%}_{-26\%}), \end{aligned} \tag{7.7}$$

where 0.68/s is the measured loading rate, 1/0.3 is due to the non-optimized loading rate at the time of the measurement with an uncertainty of ±3%, 12 is the transverse cooling enhancement factor with an uncertainty of ±5%, 3/2 is the effect of the one way laser pushing the atomic beam with an uncertainty of ±3%, 1/0.03 is compensation of the small aperture on the Zeeman slower laser with an uncertainty of ±8%, and 1/0.55 is the ratio of source efficiency between 0.20 mtorr and 0.35 mtorr with an uncertainty of ±10%.

From Eq. 7.7, the loading rate of a 1-ppt Kr/Xe gas is

$$L_{1\text{ppt Kr}} = 2.06 \times 10^{-4}\text{/s } (^{+39\%}_{-30\%}). \tag{7.8}$$

This loading rate implies that 81 minutes are required to detect one trapped atom from a 1-ppt Kr/Xe gas. Comparing this to the loading rate of the PraxAir xenon gas, 1.88/s, the krypton level in the xenon gas is estimated to be 9.1 ppb.

7.5.3 0.75 ppm krypton mixture

For the next measurement, a 0.75 ppm (±5%) Kr/Xe mixture was prepared by filling the krypton chamber with krypton gas and the reservoir with xenon gas at 57.0 torr in the mixing region. The source pressure was 0.2 mtorr as before, and the loading rate of the argon MOT was at the maximum value. The overall loading rate was controlled by switching off transverse cooling stages and partially blocking the Zeeman slower laser.

We found 24 trapped atoms in 150 seconds from APD measurement, indicating the loading rate of 0.16 atoms/s. Adjustment for the optimal setting predicts the best loading rate of the 0.75 ppm Kr/Xe mixture as

$$\begin{aligned} L_{0.75\text{ppm Kr}} &= 0.16\text{/s} \times 12 \times \frac{1}{0.03} \times \frac{1}{0.55} \\ &= 1.16 \times 10^2\text{/s } (^{+25\%}_{-21\%}), \end{aligned} \tag{7.9}$$

where 0.16/s is the measured loading rate, 12 is the enhancement by transverse cooling with an uncertainty of ±5%, 1/0.03 is compensation of the small aperture on the Zeeman slower

laser with an uncertainty of ±8%, and 1/0.55 is the ratio of source efficiency between 0.20 mtorr and 0.35 mtorr with an uncertainty of ±10%.

Equation 7.9 implies that the loading rate for a 1 ppt Kr/Xe gas is

$$L_{\text{1ppt Kr}} = 1.55 \times 10^{-4} \text{ /s } (^{+30\%}_{-25\%}), \tag{7.10}$$

corresponding to a measurement time of 108 minutes to detect one trapped atom. This measurement indicates in a 12.1-ppb krypton level of the PraxAir xenon gas.

7.5.4 System efficiency for krypton in xenon

By averaging results from the 12 ppm and 0.75 ppm Kr/Xe mixtures, we have a loading rate for 1 ppt krypton contamination in xenon gas,

$$L_{\text{1ppt Kr}} = 1.80 \times 10^{-4} \text{ /s } (^{+35\%}_{-28\%}). \tag{7.11}$$

With this loading rate, the average time required to find one trapped atom from a 1 ppt Kr/Xe sample is estimated to be 92 minutes, which is a reasonable amount of time since we can expect ∼6 atoms for a one-day measurement.

The krypton level in the PraxAir xenon gas is also calculated from the derived loading rate by

$$\frac{\text{Kr}}{\text{Xe}} = 10^{-12} \times \frac{L_{\text{PraxAir}}}{L_{\text{1ppt Kr}}} = 1.04 \times 10^{-8} \ (^{+21\%}_{-17\%}), \tag{7.12}$$

i.e., 10.4 ppb. This number is very close to the impurity level specified by the company, 10 ppb.

7.6 Xenon extraction from the XENON detector

As the trapping efficiency of our ATTA system for krypton in xenon is determined (Sec. 7.5), we are ready to measure the krypton level in a xenon sample from the XENON100 detector, which is the goal of this project. A gas container, called 'gas pipette', was built to extract and carry the xenon sample from the INFN Laboratori Nazionali del Gran Sasso (LNGS) to the laboratory at Columbia University.

The gas pipette consists of a one liter stainless steal vessel (MDC 43000-2000), an all-metal ultra-fine leak valve (Lesker VZLVM940R), and a shutoff valve as shown in Fig. 7.5.

Figure 7.5: A pipette to extract and carry xenon gas from the XENON100 detector.

Two valves are employed to make sure that the piece is leak-tight. After the pipette was assembled, it was baked at 300 °C for several days to remove water and other impurities, and shipped to the LNGS.

Chapter 8

Conclusion

As described in this thesis, we have built an atom trap trace analysis (ATTA) system to measure krypton contamination levels in the XENON dark matter detectors. The ATTA system traps and counts the contaminant atoms within the target, using standard cooling and trapping techniques, including transverse cooling, Zeeman slowing, and a magneto-optical trap (MOT).

By carefully optimizing the system, we achieved the loading efficiency required to detect krypton contamination in xenon samples within a reasonable amount of measurement time. Fluorescence photons emitted from trapped atoms are detected by an avalanche photodiode (APD). With a specially designed optical system, we obtained a signal-to-noise ratio (SNR) sufficient to discriminate single atoms signals from background noise.

The precise system efficiency for krypton in xenon gas was determined by testing the system with Kr-Xe mixtures at 0.75 ppm and 12 ppm. With the measured system efficiency, we expect to find one trapped ^{84}Kr atom at a 1-ppt Kr/Xe level in a $\sim$90 minute measurement. A test with commercial xenon gas, whose krypton level is specified as $\sim$10 ppb, estimates a 10.6-ppb krypton concentration, validating that our ATTA apparatus.

The system is ready for measurements when a xenon sample is available upon termination of the current dark matter detection run. The achieved loading efficiency is acceptable for a measurement of a 1-ppt krypton contamination, but the higher efficiency will allow us more precise result from a short-time measurement. Additionally, as XENON1T aims for a sub-ppt krypton level in its xenon target, increase of the system efficiency is desired for

future. There are several approaches for the efficiency improvement.

As discussed in Sec. 6.3.2, using the detection mode laser beam decreases the loading efficiency by 1/20 compared to the trapping mode beam. By switching two modes quickly, we can compensate for the decrease while maintaining the low background for the APD detection. Due to the loss of the detection period from mode switching, the actual enhancement will be less than by a factor of 20, but we still expect $\sim$10. The two modes can be switched by splitting one MOT laser beam into the trapping and detection beams, and blocking/unblocking each beam using mechanical shutters. It can also be done by a commercial laser power controller.

Increasing the gas cooling power will lead to more atoms below the capture velocity of the Zeeman slower, improving the Zeeman slower efficiency. Building a new Zeeman slower with a longer length can increase the capture fraction. However, these methods are not able to increase the system efficiency significantly since the capture fraction of the Zeeman slower already reached 66%.

For a long-term plan, an optical excitation methods discussed in Sec. 4.3.1 will allow us to reach a higher excitation efficiency as well as stabilize the source behavior. The non-resonant UV+UV excitation method (Fig. 4.6 (middle)) is under discussion, where the 215 nm wavelength is obtained from a diode or Ti:Sapphire laser by nonlinear frequency conversion. We expect the enhancement by a factor of up to 100 from the modification.

Bibliography

[Abbasi *et al.*, 2011] R. Abbasi, Y. Abdou, T. Abu-Zayyad, J. Adams, et al. Measurement of the atmospheric neutrino energy spectrum from 100 gev to 400 tev with icecube. *Phys. Rev. D*, 83:012001, 2011.

[Ade *et al.*, 2013] P. A. R. Ade, N. Aghanim, C. Armitage-Caplan, M. Arnaud, et al. Planck 2013 results. XVI. Cosmological parameters. *ArXiv*, 1303.5076, 2013.

[Ageron *et al.*, 2011] M. Ageron, J.A. Aguilar, I. Al Samarai, A. Albert, et al. ANTARES: The first undersea neutrino telescope. *Nuclear Instruments and Methods in Physics Research Section A*, 656(1):11 – 38, 2011.

[Ahlswede *et al.*, 2013] Jochen Ahlswede, Simon Hebel, J. Ole Ross, Robert Schoetter, et al. Update and improvement of the global krypton-85 emission inventory. *Journal of Environmental Radioactivity*, 115:34–42, 2013.

[Ahmed *et al.*, 2010] Z. Ahmed, D. S. Akerib, S. Arrenberg, C. N. Bailey, et al. Dark Matter Search Results from the CDMS II Experiment. *Science*, 327(5973):1619–1621, 2010.

[Alt, 2002] Wolfgang Alt. An objective lens for efficient fluorescence detection of single atoms. *Optik - International Journal for Light and Electron Optics*, 113(3):142 – 144, 2002.

[Alton *et al.*, 2009] D. Alton, D. Durben, M. Keeter, K. Zehfus, et al. DarkSide-50: A direct search for dark matter with new techniques for reducing background. Technical report, 2009.

[Angloher *et al.*, 2012] G. Angloher, M. Bauer, I. Bavykina, A. Bento, et al. Results from 730 kgdays of the CRESST-II Dark Matter search. *The European Physical Journal C*, 72(4):1–22, 2012.

[Aprile and Doke, 2010] E. Aprile and T. Doke. Liquid xenon detectors for particle physics and astrophysics. *Reviews of Modern Physics*, 82(3):2053–2097, 2010.

[Aprile and Zelevinsky, 2009] E. Aprile and T. Zelevinsky. Instrument development for liquid xenon dark matter searches: an atom trap trace analysis system to measure ultra-low krypton contamination in xenon. *NSF award*, #0923274, 2009.

[Aprile *et al.*, 2006] E. Aprile, C. E. Dahl, L. de Viveiros, R. J. Gaitskell, et al. Simultaneous measurement of ionization and scintillation from nuclear recoils in liquid xenon for a dark matter experiment. *Phys. Rev. Lett.*, 97:081302, 2006.

[Aprile *et al.*, 2010] E. Aprile, K. Arisaka, F. Arneodo, A. Askin, et al. First dark matter results from the XENON100 experiment. *Phys. Rev. Lett.*, 105:131302, 2010.

[Aprile *et al.*, 2011] E. Aprile, K. Arisaka, F. Arneodo, A. Askin, et al. Study of the electromagnetic background in the XENON100 experiment. *Physical Review D*, 83(8):082001, 2011.

[Aprile *et al.*, 2012a] E. Aprile, M. Alfonsi, K. Arisaka, Arneodo, et al. Dark matter results from 225 live days of XENON100 data. *Phys. Rev. Lett.*, 109:181301, 2012.

[Aprile *et al.*, 2012b] E. Aprile, K. Arisaka, F. Arneodo, A. Askin, et al. The XENON100 dark matter experiment. *Astroparticle Physics*, 35(9):573 – 590, 2012.

[Armengaud *et al.*, 2012] E. Armengaud, C. Augier, A. Benoˆ, L. Bergé, et al. Search for low-mass WIMPs with EDELWEISS-II heat-and-ionization detectors. *Phys. Rev. D*, 86:051701, 2012.

[Bartlett, 1962] N Bartlett. Xenon hexafluoroplatinate(V) $Xe^{+}[PtF6]^{-}$. *Proc. Chem. Soc.*, page 218, 1962.

[Begeman *et al.*, 1991] K. G. Begeman, A. H. Broeils, and R. H. Sanders. Extended rotation curves of spiral galaxies: dark haloes and modified dynamics. *Mon. Not. R. Astr. Soc.*, 249:523–537, 1991.

[Bertone *et al.*, 2005] Gianfranco Bertone, Dan Hooper, and Joseph Silk. Particle dark matter: evidence, candidates and constraints. *Physics Reports*, 405(5-6):279–390, 2005.

[Bertone, 2010] Gianfranco Bertone. The moment of truth for WIMP dark matter. *Nature*, 468(7322):389–93, 2010.

[Bjorklund and Levenson, 1981] G. C. Bjorklund and M. D. Levenson. Sub-Doppler frequency-modulation spectroscopy of I_2. *Phys. Rev. A*, 24:166–169, 1981.

[Bradač *et al.*, 2008] Maruša Bradač, Steven W. Allen, Tommaso Treu, Harald Ebeling, et al. Revealing the properties of dark matter in the merging cluster macs j0025.41222. *The Astrophysical Journal*, 687(2):959, 2008.

[Carr *et al.*, 2006] J. Carr, G. Lamanna, and J. Lavalle. Indirect detection of dark matter. *Reports on Progress in Physics*, 69(8):2475, 2006.

[Cartledge *et al.*, 2008] Stefan I. B. Cartledge, J. T. Lauroesch, David M. Meyer, Ulysses J. Sofia, et al. Interstellar krypton abundances: The detection of kiloparsec-scale differences in galactic nucleosynthetic history. *The Astrophysical Journal*, 687(2):1043, 2008.

[Chen *et al.*, 1999] C. Y. Chen, Y. M. Li, K. Bailey, T. P. O'Connor, et al. Ultrasensitive isotope trace analyses with a magneto-optical trap. *Science*, 286(5442):1139–41, 1999.

[Chen *et al.*, 2001] C. Y. Chen, K. Bailey, Y. M. Li, T. P. O'Connor, et al. Beam of metastable krypton atoms extracted from a rf-driven discharge. *Rev. Sci. Inst.*, 72(1):271–272, 2001.

[Clowe *et al.*, 2004] Douglas Clowe, Anthony Gonzalez, and Maxim Markevitch. Weak-lensing mass reconstruction of the interacting cluster 1e 0657558: Direct evidence for the existence of dark matter. *The Astrophysical Journal*, 604(2):596, 2004.

[Clowe *et al.*, 2006] Douglas Clowe, Marusa Bradac, Anthony H. Gonzalez, Maxim Markevitch, et al. A direct empirical proof of the existence of dark matter. *The Astrophysical Journal Letters*, 648(2):L109, 2006.

[Du, 2003] Xu Du. Realization of radio-krypton dating with an atom trap. PhD thesis, Northwestern University, 2003.

[Ekwurzel *et al.*, 1994] Brenda Ekwurzel, Peter Schlosser, William M. Smethie, L. Niel Plummer, et al. Dating of shallow groundwater: Comparison of the transient tracers 3H/3He, chlorofluorocarbons, and ^{85}Kr. *Water Resources Research*, 30(6):1693–1708, 1994.

[Elmer, 2007] Perkin Elmer. Single Photon Counting Module SPCM-AQRH series data sheet. Fremont, CA, 2007.

[Feng, 2010] Jonathan L. Feng. Dark matter candidates from particle physics and methods of detection. *Annual Review of Astronomy and Astrophysics*, 48(1):495–545, 2010.

[Fixsen, 2009] D. J. Fixsen. The temperature of the cosmic microwave background. *The Astrophysical Journal*, 707(2):916, 2009.

[Foot, 2005] C.J. Foot. *Atomic physics*. Oxford master series in physics. Oxford University Press, 2005.

[Friedman *et al.*, 1967] H. Friedman, E. T. Byram, and T. A. Chubb. Distribution and variability of cosmic X-ray. *Science*, 156:374–378, 1967.

[Gaitskell, 2004] Richard J. Gaitskell. Direct detection of dark matter. *Annual Review of Nuclear and Particle Science*, 54(1):315–359, 2004.

[Glatz, 1996] Joseph Glatz. Krypton gas penetrant imaging – a valuable tool for ensuring structural integrity in aircraft engine components. *Materials Evaluation*, 54:1352–1362, 1996.

[Gordon and Selvin, 2003] Matthew P. Gordon and Paul R. Selvin. A microcontroller-based failsafe for single photon counting modules. *Review of Scientific Instruments*, 74(2):1150, 2003.

[Hall, 1981] J. L. Hall. Optical heterodyne saturation spectroscopy. *Applied Physics Letters*, 39(9):680, 1981.

[Haynes, 2013] William M. Haynes, editor. *CRC handbook of chemistry & physics*. CRC Press, 94th edition, 2013.

[Hippel *et al.*, 1985] Frank Von Hippel, David H Albright, and Barbara G Levi. Stopping the production of fissile materials for weapons. *Scientific American*, 253:40–47, 1985.

[Hitachi, 2005] Akira Hitachi. Properties of liquid xenon scintillation for dark matter searches. *Astroparticle Physics*, 24(3):247–256, 2005.

[Jortner *et al.*, 1965] Joshua Jortner, Lothar Meyer, Stuart A. Rice, and E. G. Wilson. Localized excitations in condensed Ne, Ar, Kr, and Xe. *The Journal of Chemical Physics*, 42(12):4250, 1965.

[Jungman *et al.*, 1996] Gerard Jungman, Marc Kamionkowski, and Kim Griest. Supersymmetric dark matter. *Physics Reports*, 267(56):195–373, 1996.

[Kane and Watson, 2008] Gordon Kane and Scott Watson. Dark matter and LHC: What is the connection? *Modern Physics Letters A*, 23(26):2103–2123, 2008.

[Levin and Hesshaimer, 1996] Ingeborg Levin and Vago Hesshaimer. Refining of atmospheric transport model entries by the globally observed passive tracer distributions of 85 krypton and sulfur hexafluoride (SF6). *Journal of Geophysical Research*, 101(16):745–755, 1996.

[Lewis *et al.*, 2003] Aaron D. Lewis, David A. Buote, and John T. Stocke. Chandra observations of a2029: The dark matter profile down to below $0.01r_{vir}$ in an unusually relaxed cluster. *The Astrophysical Journal*, 586(1):135, 2003.

[Lim, 2013] Kyungen Lim. *XENON100 Dark Matter Search : Scintillation Response of Liquid Xenon to Electronic Recoils*. PhD thesis, Columbia University, 2013.

[Linde Electronics and Specialty Gases, 2010] Linde Electronics and Specialty Gases. Multipurpose analog PID controller. Technical report, The Linde Group, 2010.

[Lindemann and Simgen, 2013] S. Lindemann and H. Simgen. Krypton assay in xenon at the ppq level using a gas chromatographic system combined with a mass spectrometer. *ArXiv*, 1308.4806, 2013.

[Liu and Littman, 1981] Karen Liu and Michael G. Littman. Novel geometry for single-mode scanning of tunable lasers. *Opt. Lett.*, 6(3):117–118, 1981.

[Macalpine and Schildknecht, 1959] W. W. Macalpine and R. O. Schildknecht. Coaxial resonators with helical inner conductor. *Proc. IRE*, 47:2099, 1959.

[Marcassa *et al.*, 1993] L. Marcassa, V. Bagnato, Y. Wang, C. Tsao, et al. Collisional loss rate in a magneto-optical trap for sodium atoms: Light-intensity dependence. *Phys. Rev. A*, 47:R4563–R4566, 1993.

[Marchionni *et al.*, 2011] A Marchionni, C Amsler, A Badertscher, V Boccone, et al. ArDM: a ton-scale LAr detector for direct Dark Matter searches. *Journal of Physics: Conference Series*, 308(1):012006, 2011.

[McDougall, 1999] Ian McDougall, editor. Geochronology and thermochronology by the $^{40}Ar/^{39}Ar$ method. New York : Oxford University Press, 2nd edition, 1999.

[McKinsey and Orzel, 2005] D.N. McKinsey and C. Orzel. Radioactive krypton background evaluation using atom counting. *Nuclear Instruments and Methods in Physics Research Section A: Accelerators, Spectrometers, Detectors and Associated Equipment*, 545(12):524 – 531, 2005.

[McKinsey *et al.*, 2010] D N McKinsey, D Akerib, S Bedikian, A Bernstein, et al. The LUX dark matter search. *Journal of Physics: Conference Series*, 203(1):012026, 2010.

[Metcalf and van der Straten, 1999] H.J. Metcalf and P. van der Straten. Laser cooling and trapping. Graduate Texts in Contemporary Physics. Springer-Verlag GmbH, 1999.

[Meyrath, 2005] Todd P. Meyrath. Multipurpose analog PID controller. Technical report, University of Texas at Austin, 2005.

[Ovchinnikov, 2008] Y. B. Ovchinnikov. A permanent Zeeman slower for Sr atomic clock. *The European Physical Journal Special Topics*, 163(1):95–100, 2008.

[Penzias and Wilson, 1965] A. A. Penzias and R. W. Wilson. A measurement of excess antenna temperature at 4080 Mc/s. *The Astrophysical Journal*, 142:419–421, 1965.

[Phillips and Metcalf, 1982] William D. Phillips and Harold Metcalf. Laser deceleration of an atomic beam. *Phys. Rev. Lett.*, 48:596–599, 1982.

[Plante, 2012] Guillaume Plante. *The XENON100 dark matter experiment: design, construction, calibration and 2010 search results with improved measurement of the scintillation response of liquid xenon to low-energy nuclear recoils.* PhD thesis, Columbia University, 2012.

[Prodan and Phillips, 1984] John V. Prodan and William D. Phillips. Chirping the light-fantastic? Recent NBS atom cooling experiments. *Progress in Quantum Electronics*, 8(34):231 – 235, 1984.

[Reinaudi *et al.*, 2012] G. Reinaudi, C. B. Osborn, K. Bega, and T. Zelevinsky. Dynamically configurable and optimizable Zeeman slower using permanent magnets and servomotors. *J. Opt. Soc. Am. B*, 29(4):729–733, 2012.

[Rentzepis and Douglass, 1981] P. M. Rentzepis and D. C. Douglass. Xenon as a solvent. *Nature*, 293:165, 1981.

[Schroder *et al.*, 1971] J. Schroder, K. O. Munnich, and D. H. Ehhalt. Krypton-85 in the troposphere. *Nature*, 233(29):614, 1971.

[Steane *et al.*, 1992] A. M. Steane, M. Chowdhury, and C. J. Foot. Radiation force in the magneto-optical trap. *J. Opt. Soc. Am. B*, 9(12):2142–2158, 1992.

[Sukenik and Busch, 2002] C. I. Sukenik and H. C. Busch. A rf discharge cell for saturated absorption spectroscopy of metastable argon. *Rev. Sci. Inst.*, 73(2):493–494, 2002.

[Taylor and Thompson, 2008] Barry Taylor and Ambler Thompson. The international system of units (si). Technical report, NIST, 2008.

[Yamashita *et al.*, 2004] M. Yamashita, T. Doke, K. Kawasaki, J. Kikuchi, and S. Suzuki. Scintillation response of liquid Xe surrounded by PTFE reflector for gamma rays. *Nuclear*

Instruments and Methods in Physics Research Section A: Accelerators, Spectrometers, Detectors and Associated Equipment, 535(3):692 – 698, 2004.

[YanQiang *et al.*, 2012] Guo YanQiang, Li Gang, Zhang YanFeng, Zhang PengFei, et al. Efficient fluorescence detection of a single neutral atom with low background in a microscopic optical dipole trap. *Science China Physics, Mechanics & Astronomy*, 55(9):1523, 2012.

[Young *et al.*, 2002] L. Young, D. Yang, and R. W. Dunford. Optical production of metastable krypton. *Journal of Physics B: Atomic, Molecular and Optical Physics*, 35(13):2985, 2002.

[Ziegler and Nichols, 1942] J. G. Ziegler and N. B. Nichols. Optimum settings for automatic controllers. *Trans. ASME*, 64:759–768, 1942.

[Zwicky, 1933] F. Zwicky. Spectral displacement of extra galactic nebulae. *Helv. Phys. Acta*, 6:110–127, 1933.